ELECTROCATALYTIC APPLICATION OF 3D TRANSITION METAL COMPLEXES FOR EFFICIENT HYDROGEN GENERATION

JAKE THIBODEAU

Thesis submitted to the University of Ottawa
in partial Fulfillment of the requirements for the
degree of Master of Science in Chemistry

Department of Chemistry and Biomolecular Sciences
Faculty of Science
University of Ottawa

Abstract

The production of hydrogen gas through green processes such as electrolysis is crucial in shifting away from fossil fuel derivatives, in order to enhance the viability of hydrogen as a sustainable energy alternative. This work investigates several complexes based primarily on 3d transition metals, in particular Mn, Fe, Ni, Cu, and additionally Mo for their electrocatalytic capabilities towards hydrogen evolution reactions (HER) with the electrolysis of water as the ideal proton source. A secondary proton source, acetic acid, was also investigated. In particular, the complexes explored were pyridine-based bidentate and tridentate Mn(I), Mo(0) and Mo(VI) species, macrocyclic quinquedentate complexes of Mn(II), Fe(III), Ni(II), Cu(II), and open-ended tetradentate complexes for Ni(II) and Cu(II). Four unreported crystal structures, using single crystal X-ray diffraction analysis, for Mn(II), Fe(III) and Ni(II) complexes were found. This research cumulated in the creation of a $NiO/Ni(OH)_2$ film electrodeposited onto a FTO glass electrode, with the source material being an open-ended tetradentate Ni(II) complex in 0.1 M KCl aqueous solution. This Ni-derived film provided good HER performance for the electrolysis of water in 0.1 M KCl solution, with results providing an average of 46.7 µmol of hydrogen as detected by GC-TCD with the electrode held at -1.2 V (*vs*. Ag/AgCl) over 1 hr, with a Faradaic efficiency of ~96%.

Acknowledgements

To my professor, Darrin Richeson, for always being someone who would encourage you forward and being a positive influence. I'm grateful that you allowed me the opportunity to join the group, and I'll always appreciate you welcoming me in. I think this time has been a great learning experience. It has certainly pushed my boundaries and knowledge, and even though I can recognize there is still much more to learn, I am feeling more capable on this journey to becoming a scientist. This is in no small part thanks to everything you have done, and you will always have my gratitude.

To my mother, who has supported me throughout my pursuit of higher education. You have been there for me through this entire journey and have been someone I can always rely on. I'll always appreciate everything you have done for me.

To my group members, JB, SN, JF, RJ, EM, you've made being in the lab enjoyable and a welcome place to be. Even though our paths will eventually go on their own ways, I'll remember this time fondly, and I hope all goes well with your own journeys.

To my close friends, KL, HM, MR, and LY, it's been great to have you as such. And to professor BB, for providing that extra bit of encouragement that made all the difference.

Table of Contents

List of Figures

List of Schemes

List of Tables

List of Abbreviations

1,2-bis	1,2-bis(3-aminopropylamino)ethane
1,8-dia	1,8-diamino-3,6-dioxaoctane
AcOH	Acetic acid
Ag/AgCl	Silver/silver chloride, as reference electrode
Ag5N-3,2,3	(2,15-dimethyl-3,7,10,14,20-pentaazabicyclo[14.3.1]eicosa-1(20),2,14,16,18-pentaene-N^3,N^7,N^{10},N^{14},N^{20})-silver(I) perchlorate
AFM	Atomic force microscopy
BG	Background
BPY	2,2'-bipyridine
CE	Counter electrode
CNT	Carbon nanotubes
CPE	Controlled potential electrolysis
Cu3N2O	Dibromo-(2,13-dimethyl-6,9-dioxa-3,12,18-triazabicyclo[12.3.1]octadeca-1(18),2,12,14,16-pentaene-κN^3,κN^{12},κN^{18},κO^6,κO^9)-copper(II)
Cu4N	Dibromo-(N1',N3-ethane-1,2-diyldipropane-1,3-diamine)-copper(II)
CV	Cyclic voltammetry
DAD	1,4-di-*tert*-butyl-1,3-diazabutadienyl
$E_{1/2}$	Half-wave potential
E_{cat}	Potential required for catalysis
E_{red}	Potential for reduction peak
E_{ox}	Potential for oxidation peak
ESI	Electrospray ionization
EDX	Energy dispersive X-ray spectroscopy
Fc/Fc^+	Ferrocene/Ferrocenium ion, as electrochemical reference
FE	Faradaic Efficiency
Fe5N-2,2,2	Dichloro-(2,13-dimethyl-3,6,9,12,18-pentaazabicyclo[12.3.1]octadeca-1(18),2,12,14,16-pentaene-N^3,N^6,N^9,N^{12},N^{18})-iron(III) perchlorate
FTIR	Fourier transform infrared
FTO	Fluoride-doped tin oxide
GC	Gas chromatography
i_p/i_{cat}	Current required for catalysis
ITO	Indium-doped tin oxide
KCl	Potassium chloride
kWh	Kilowatt-hour
LSV	Linear sweep voltammetry

MJ	Megajoule
MOFs	Metal-organic frameworks
Mn3N2O	Diaqua-(2,13-dimethyl-6,9-dioxa-3,12,18-triazabicyclo[12.3.1]octadeca-1(18),2,12,14,16-pentaene-κN^3,κN^{12},κN^{18},κO^6,κO^9)-manganese(II) perchlorate chloride
Mn5N-2,2,2	Diaqua-(2,13-dimethyl-3,6,9,12,18-pentaazabicyclo[12.3.1]octadeca-1(18),2,12,14,16-pentaene-N^3,N^6,N^9,N^{12},N^{18})-manganese(II) perchlorate chloride
Mn5N-3,2,3	Chloro-(2,15-dimethyl-3,7,10,14,20-pentaazabicyclo[14.3.1]eicosa-1(20),2,14,16,18-pentaene-N^3,N^7,N^{10},N^{14},N^{20})-aquamaganese(II) perchlorate
Mn-DPA	$[Mn(\kappa^3\text{-DPA})(CO)_3]^+Br^-$
Mn-TPA	$[Mn(\kappa^3\text{-TPA})(CO)_3]^+Br^-$
Mo-BPY	$(^t BuN)_2MoCl_2\cdot$bpy
Mo-DAD	$(^t BuN)_2MoCl_2\cdot(^t BuDAD^H)$
Mo-TPA	$Mo(\kappa^3\text{-TPA})(CO)_3$
MS	Mass spectrometry
$NaNO_2$	Sodium nitrite
Ni4N	Dichloro-(N1',N3-ethane-1,2-diyldipropane-1,3-diamine)-nickel(II)
Ni5N-3,2,3	Methanol-(2,15-dimethyl-3,7,10,14,20-pentaazabicyclo[14.3.1]eicosa-1(20),2,14,16,18-pentaene-N^3,N^7,N^{10},N^{14},N^{20})-nickel(II) diperchlorate
NHE	Normalized hydrogen electrode
RE	Reference electrode
RHE	Reversible hydrogen electrode
SEM-EDS	Scanning electron microscopy with energy dispersive X-ray spectroscopy
SHE	Standard hydrogen electrode
TBAHFP	Tetrabutylammonium hexafluorophosphate
TETA	Triethylenetetramine
TCD	Thermal conductivity detector
TPA	Tris(2-pyridylmethyl)amine
XRD	X-ray diffraction
XPS	X-ray photoelectron spectroscopy
WE	Working electrode

Chapter 1: Introduction

1.1 – Energy Sources and Hydrogen

Energy and the effective application of available resources is a perpetual demand in our society. When evaluating energy sources, a critical factor comes from not only the total energy output the source can deliver, but in terms of energy density. Energy density reflects both in terms of weight and volume per energy unit. Fossil fuels represent an attractive source of energy due to their stability, high energy density, and extensive industrial infrastructure built around their use throughout history. They generally have high volumetric energy density (~35-40 MJ/L), and a good gravimetric energy density, (~45-60 MJ/kg).[1] However, with the well-documented adverse impact that fossil fuel consumption has on climate change and global warming, there is a considerable effort to provide sustainable alternative energy sources.

Hydrogen (H_2) is a contender to fulfill these energy demands. It has an extremely high gravimetric energy density at ~140 MJ/kg in its liquid state, but has deficiencies relating to how much volume it requires, being just below ~10 MJ/L.[1] With appropriate hydrogen storage technologies under research such as metallic hydrogen, hydrogen storage alloys, and inorganic/liquid hydrides, this remains an important part of improving viability for widespread use.[2,3] Pairing with this is the production component of hydrogen gas, which currently the vast majority (96%) of such comes from fossil fuel derivatives – 48% from natural gas, 30% from petroleum fractioning and 18% from coal gasification.[4,5]

The remaining 4% is attributed to electrolysis and other water-splitting methods, such as solar thermochemical, photo-electrocatalysis and photocatalysis.[4,6,7] The steam-methane reforming process, paired with a water-gas shift reaction, is the most common for creating hydrogen gas (95% in the United States).[8] The process generally heats water mixed with methane to a high temperature (700-1000 °C) and pressure (3-25 bar) which itself demands consumption of fossil fuels for heating.[8,9] These two processes utilize the following redox reactions in Equation 1 for steam-methane reformation, and Equation 2 in a water-gas shift reaction:

$$CH_4 + H_2O\ (+heat) \rightarrow CO + 3\ H_2 \quad (1)$$

$$CO + H_2O\ \rightarrow CO_2 + H_2 \quad (2)$$

However, this overall process also yields considerable amounts of CO_2, reporting around 9-14 kg CO_2 / kg H_2.[8] With the stated total worldwide production of hydrogen being at approximately 120 million tons per year and the relevant conversion to CO_2 past 1 billion tons, this represents a significant portion of the total CO_2 emissions at ~35.8 billion tons per year.[10] It is reported that approximately 90% of this produced hydrogen is used in industries such as fertilizer production by ammonia synthesis, methanol production, oil and fat hydrogenation, petrochemical processing, and metallurgical applications.[11,12] Improvements are being made to the overall efficiency of hydrogen production, such as using electrified steam reforming, improving efficiency to ~5.3-5.5 kg CO_2 / kg H_2.[13] Others seek to be carbon neutral by replacing methane with ethanol sourced from biofuels.[14] Cost remains an important consideration throughout all this. The

conventional process above for hydrogen production comes to a cost of \$2.76 / kg H_2, with the expected electrified process averaging \$3.49 / kg H_2.[13]

With the above considerations, electrolysis emerges as an opportunity for hydrogen production without carbon emissions or other adverse climate impacts. The process itself is straightforward in that it generally involves applying a significant electrical potential into water or a water-containing solution, the resulting by-products of hydrogen, hydroxide, and oxygen pose minimal environmental concerns. The general reaction for electrolysis is by two half-reactions of a Hydrogen Evolution Reaction (HER) and an Oxygen Evolution Reaction (OER) with HER in pH=7 solution is displayed in Equation 3, and OER in Equation 4.[15–17] The primary expense of production comes from the electrical demand of the process, currently stated at 50 kWh / kg H_2.[18] This can significantly impact the baseline cost, with the reference's conversative estimate of \$0.06 / kWh and likewise \$3.00 / kg H_2. With respect to optimization, it should be highlighted that amperage (or Ampere-hour) is the key relevant factor in Faradaic efficiency and thus electrolysis, and not kWh directly. With the conversion noted in Equation 5, a lower voltage can lead to an overall higher efficiency in the system.

$$2\,H_2O + 2\,e^- \rightarrow H_2 + 2\,OH^- \quad (3)$$

$$4\,OH^- \rightarrow O_2 + 2\,H_2O + 4\,e^- \quad (4)$$

$$Ampere = \frac{(Watt \cdot hour)}{(Volt \cdot hour)} \quad (5)$$

In addition to electrical costs, using a working electrode that is cost-efficient and reliable is of importance. Rare metals such as platinum, palladium, ruthenium, and iridium are considered to be the best performers for their high suitability and efficient hydrogen

generation.[19–22] This would include derivatives such as their oxide counterparts.[19] The availability of such metals and associated costs however generally limits their widespread use, spurring research into alloys or using similar metals that might show performance close to these ideal groups.[21,23] An important component in this search are the relative abundance and cost of a particular metal. Directly above platinum and palladium located in the 3d transition metals lies nickel, a notable example to be explored here. Similar metals right next to nickel are cobalt and copper – copper being of interest here as a prompt for further research.

This thesis will address both homogeneous and heterogeneous electrochemical reactions. These refer to the physical state of the catalyst and of the intended reaction substrate. In this case, the term homogeneous refers to both being in the solution state while heterogeneous refers to a solid-state catalyst and a solution reactant.

1.2 – Electrochemical Features for Non-Electrochemists

1.2.1 – Cyclic Voltammetry and Controlled Potential Electrolysis

In this thesis, the main device for characterization and assessing the ability of a species for hydrogen production is a potentiostat – an electronic device that controls the application of potential (V) or current (A) and can measure the potential/current/resistance passed through a system. Two main techniques will be applied – cyclic voltammetry (CV) and controlled potential electrolysis (CPE). Cyclic

voltammetry applies a variable potential at a chosen rate of change and measures the detected current during this process. An example would be starting from 0 V and passing to -1.5 V, changing at a rate of 0.1 V s^{-1}. One pass from 0 to -1.5 V, back to 0 V can be referred to as one cycle. This technique is useful for the characterization of a possible catalyst, along with assessing the electrochemical cell response. The latter can include details such as the potential window – reduction of the solvent at the electrode (negative potential) and oxidation (positive potential) without catalyst present.[24] A negative applied potential can result in reduction and is referred to as a cathodic potential, with positive applied voltages associated with oxidation and termed anodic potentials. Cyclic voltammetry will be presented according to the IUPAC standards, with the plotting of increasing reduction potentials to the left-hand side of the plot and reduction currents plotted on the negative y-axis.[24] Anodic or oxidation currents will be reversed with increasing anodic potential to the right and oxidation currents plotted on the positive y-axis. For interest, the US standard differs from this and essentially rotates the display of this information by 180 degrees.[24]

With cyclic voltammetry measurements, there are several normal ideal characteristics. An ideal solution without substrate or catalyst will largely be flat in current with a minimal difference between the outgoing scan and the return scan (~10 mA or less), essentially showing the non-reactivity of the solution. With an added catalyst, it is desirable to see a strong increase in current at a potential (V), with a decline in current after, forming a curve or 'peak' (Figure 1). This peak represents a maximum of the current curve in that region and is designated as i_p or i_{cat}, with E_{cat} termed as the potential required

for catalysis.[24–26] These observations are linked with a redox event and are typically associated with the reduction peak (E_{red}) or oxidation peak (E_{ox}) of the species, depending on the applied potential. The voltage associated with the increasing current is termed the onset potential.[27] As this onset potential is sometimes less than clear, a reference point can be assigned based on a defined current density (e.g. 0.1 mA cm^{-2}) with an associated voltage.[17,20,28] Overpotential (η) directly relates to this defined current density, defined as the difference between the thermodynamic potential and the given potential at which the catalyst operates at the given current.[26] The thermodynamic potential relates to the Nernst equation in the reduction of protons.[26] The addition of a substrate to this system can lead to an increase in the current associated with the redox event, this current enhancement is a signature of catalysis. This increased current must be compared against the background to establish if this is attributable to catalyst functionality.

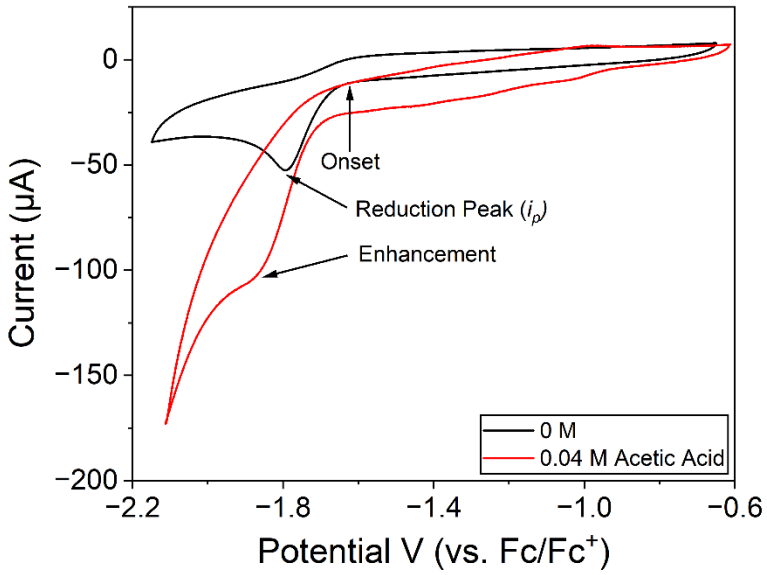

Figure 1: Example of a cathodic scan cyclic voltammogram of a potential catalyst complex, highlighting onset, reduction peak (i_p), and enhancement with 0.04 M acetic acid as a substrate.

The second main technique that will be employed is controlled potential electrolysis (CPE). In a CPE experiment, a defined voltage is applied for a given timeframe (e.g. -1.3 V for 3600 s). Using the current flow and the time, the number of electrons transferred during this time is calculated. This technique will be primarily used for the identification and quantitative measurement of a product (e.g. hydrogen) of catalysis. Ideally, the applied potential will be below that of any background product formation, and a measurement of CPE should be done to compare product formation with and without the presence of a catalyst. Using the current delivered by the potentiostat to the system multiplied by the given time period, the total coulombs delivered can be determined, which can further be compared against the amount of product to determine Faradaic efficiency.

1.2.2 – Faradaic Efficiency

Faradaic efficiency (FE) is determined by the ratio of the moles of product to the moles of electrons delivered by the potentiostat.[29] In this equation 6 for hydrogen generation, n_{H_2} represents the mols of H_2, n_e represents the mols of electrons nominally needed to form one molecule of diatomic hydrogen from water ($n_e = 2$); F represents Faraday's Constant (96485.3321 s A mol^{-1} or C mol^{-1}); Q is the total charge passed in Coulombs, from the integrated area of current (A) · time (s) over the duration of CPE.

$$\frac{n_{H_2} \cdot n_e \cdot F}{Q} \cdot 100\% \quad (6)$$

1.2.3 – Electrochemical Cell

An electrochemical cell has a few general key components. These general parts are the electrodes, a solution with the immersed electrodes, and an enclosed container to hold these components. Typically, three electrodes are used - a working electrode, a counter electrode, and a reference electrode. For this thesis, the working and counter electrodes are located at opposing ends of the cell, with the reference electrode placed in between, closer to the working electrode (Scheme 1). The reference electrode is placed closer to the working electrode to reduce the influence of ohmic drop between the two, or otherwise resistance of the solution influencing the detection by the reference electrode.

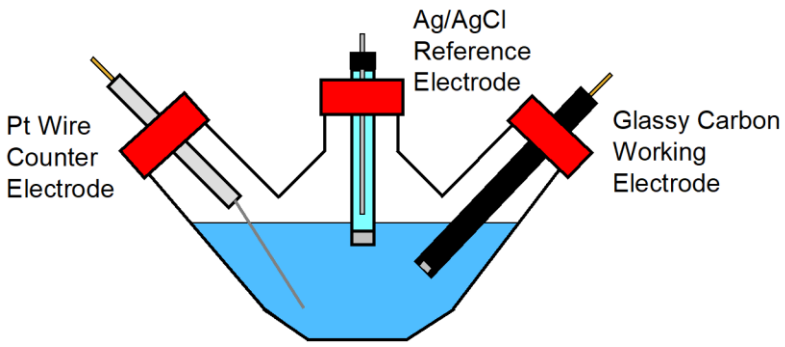

Scheme 1: General Schematic of an Electrochemical Cell Setup.

The working electrode serves as the output device in which the potential is set and the current flowing through the system is measured. In this thesis, the working electrode for cyclic voltammetry is typically a glassy carbon electrode, often used for its wide potential solvent window and sensitivity due to the polished and small surface

area.[30] This smaller surface area also greatly reduces the total reaction rate, a benefit in that a more finite change in the material can be observed if desired. During CPE, the electrode was changed to one that provides a larger surface area, allowing a greater total rate of reaction but losing some degree of finer sensitivity to peak shape and resolution. Graphite rods are normally suitable for this purpose, although many alternatives exist such as fluoride-doped tin oxide glass.[30,31] The reference electrode is used to sense the actual potential applied across the working and counter electrodes, controlled by the potentiostat. The counter electrode is present to complete the circuit and ideally will be largely inert to the solution components, although it has been found that the counter electrode material can potentially alter reactions significantly. As literature reports in one case where the counter electrode was cathodic, a 90% yield was given for platinum, 60% for nickel, and no reaction with graphite.[30] Yields were consistently high when the anodic working electrode was exchanged, with platinum held as the counter electrode.

1.2.4 – Potential Windows and References

The term 'potential window' generally refers to the upper and lower limits of voltage that can be applied within an electrochemical cell. Related to this is a 'solvent window' or 'potential solvent window', both referring to the solvent of the electrochemical cell.[30] This defines the voltage limits of solvent non-reactivity before it becomes reduced or oxidized at the electrode, depending on the applied voltage. These solvent windows are well documented in literature, and not only depend on the solvent

itself but the type of working electrode and electrolyte present in the solution.[30] Acetonitrile is a common organic solvent of choice with a window spanning from ~-3 V to ~2 V (*vs.* Ferrocene/Ferrocenium or Fc/Fc^+). Paired with acetonitrile is the electrolyte Tetrabutylammonium hexafluorophosphate (TBAHFP), used for its generally non-reactive properties and electrochemical stability.[32] Water is an ideal choice as a hydrogen source due to sustainability issues but has a relatively small potential solvent window before a reaction occurs. Water's base potential window in a pH=7 system is defined with a reversible reduction potential of -0.41 V (*vs.* RHE) and a reversible oxidation potential of 0.81 V (*vs.* RHE).[16,33,34] These potentials are modified by pH values according to the Nernst Equation, discussed in more detail in the next section. Referring back to the working electrode choice, platinum nominally has an overpotential requirement of -0.01 V from this theoretical value, with glassy carbon at -1.13 V.[30] The potential window can be experimentally observed by cyclic voltammetry to confirm electrode and electrolyte impact.

The use of references is critical as electrochemical systems have unique variances that often shift the detected potentials. Two reference types are used to address this. The first is an Ag/AgCl wire reference electrode with 3 M KCl aqueous solution contained in a small glass vessel, with conductive sensing through a small frit. This reference type is preferred due to its stability and established potential shift, optimized for use in aqueous solutions. The other method uses a bare silver wire present in the electrochemical cell as a pseudo-reference and is commonly employed in organic solution, with ferrocene added in the solution as a known redox reference. Ferrocene is useful in two notable

characteristics – it is typically non-reactive and innocent for electrocatalytic activity outside of its respective known redox peaks, and these peaks have a known ideal shape that allows ease of measurement (Figure 2). These are detected as a reversible ferrocene/ferrocenium redox couple during an anodic CV scan, typically passing from 0 to 1.0 V. The mean potential of the observed redox peaks ($E_{1/2}$) is used for referencing (e.g. 0.5 V).[24] However, the detected potentials can vary significantly (e.g., +/- 0.4 V) primarily due to the cell setup and solution present. These reference peaks will provide a constant point of reference in the event the added substrate does affect the entire cell potential. In theory, the peak-to-peak separation between reduction and oxidation peaks will be 57 mV, and 'the width at half max on the forward scan of the peak' as 59 mV.[24] These values are often observed as larger values, attributed to ohmic drop by increased resistance in solution.[24] This can be compensated by higher electrolyte concentrations, but overall, this is highlighted as a nuance of the electrochemical system.

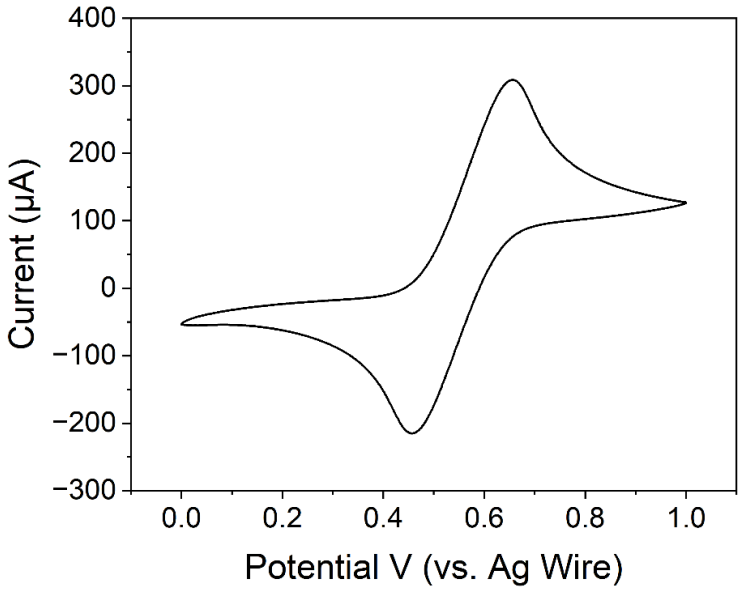

Figure 2: An example of an observed ferrocene redox event in acetonitrile, from this work.

There are disadvantages to the pseudo-reference electrode approach. There are times when comparing uncorrected data with substrate addition (such as water or glacial acetic acid) may provide a consistent reduction peak. Correcting with ferrocene (by subtraction of the $E_{1/2}$ potential) couple may give small variations in the measured applied voltage. This is usually not a major concern, only a factor to consider during analysis, and ferrocene remains fairly reliable as a reference with this note. Another scenario is where ferrocene and the relative cell potential correction does not adequately explain a peak shift. For example, if a reduction peak shifts by 100 mV, yet the ferrocene reference has only moved 50 mV, it may be reasoned that the cell potential shifting is not entirely responsible for the reduction peak change. Further cyclic voltammetry characteristics such as shape and current may help define and explain any changes. When examining anodic or positive potentials by cyclic voltammetry, the added ferrocene will dominate any electrocatalytic events in the vicinity of the reference peaks, and so it is unsuitable for it to be present if performing any oxidative characterization. Notably as well, ferrocene will significantly colour the solution and obscure visual observations of product produced at the electrodes.

With either the Ag wire or an Ag/AgCl electrode setup, the potentiostat will adjust the potential provided at the working electrode as sensed by the reference electrode. The reference electrode is sensitive according to distance from the working electrode, but this effect is minimal in the self-contained Ag/AgCl reference, as the conductivity is largely controlled and standardized by the frit permittivity. In contrast, the bare Ag wire has no protective qualities and is susceptible to large variances (such as 0.2 V) with moderate

repositioning, as observed by the ferrocene/ferrocenium redox peaks shifting. However, if the reference electrode position is held constant, ferrocene correction is fairly reliable as it is held to that detected redox event.

1.2.5 – Nernst Equation and Potential Referencing

In the literature, it can be seen that Ag/AgCl is a common reference electrode in aqueous solutions. However, reported voltages are often converted to compare against a reversible hydrogen electrode (RHE) or a normal hydrogen electrode (NHE) in order to provide a reliable comparison in literature, with a 3 M KCl Ag/AgCl reference held to be 0.197 V (*vs.* RHE/NHE). RHE and NHE are generally equivalent, however, RHE accounts for pH change in the solution while NHE is defined as the potential of platinum within an ideal solution of pH=0 and H_2 at 1 atm.[35–37] A standard hydrogen electrode (SHE) can also be referred to for scaling and is equivalent to NHE.[35] RHE is one of the most often reported voltage references in literature and it derives its relationship directly with the simplified Nernst equation.[15] The general idea for this equation is that it accounts for the minimum possible voltage for electrolysis in an aqueous system, accounting for the pH in a defined manner. In this way, a calculation converting the detected potential using an Ag/AgCl reference to RHE can be done (Equation 7). $\mathrm{E}^0_{\mathrm{AgCl}}$ is equivalent to 0.197 V *vs.* RHE.

$$\mathrm{E_{RHE}} = \mathrm{E_{AgCl}} + 2.303\frac{\mathrm{RT}}{\mathrm{F}} \cdot \mathrm{pH} + \mathrm{E}^0_{\mathrm{AgCl}}$$

$$= \mathrm{E_{AgCl}} + 0.059 \cdot \mathrm{pH} + \mathrm{E}^0_{\mathrm{AgCl}} \quad (7)$$

This method has come under much debate regarding the accuracy and reliability of conversion to RHE.[15] For example, some researchers experimentally determined the RHE potential for electrolysis via two platinum foil electrodes, purging the cell and solution with pure hydrogen and conducting their calibration against the Ag/AgCl reference. Their experimental value of 0.706 V significantly exceeds that of the calculated value of 0.611 V at the base pH of 7. Furthermore, they tested the solution pH to be 5.46, placing their calculated value at 0.520 V - a difference of 0.186 V from their experimental value. This leads to some notion that comparison and conversion via the Nernst equation may be less than ideal. With these stated values deviating notably from standard calculation with the Nernst equation, it exacerbates simple comparison and highlights the need for additional confirmation data. An example is testing in H_2SO_4 as a highly common electrolysis characterization solvent, with platinum serving as a known reported data point.[31,38]

While the Nernst equation and references to NHE/RHE are interesting and relevant, especially in terms of thermodynamic potential and determining the minimum onset potential possible for electrolysis, it does not necessarily fully relate to real-life conditions. For example, one group conducted their hydrogen production test at -0.26 V *vs.* RHE, with a small test at -0.055 V *vs.* RHE to confirm their overpotential value.[39] Another group conducted their hydrogen production testing at a stated -1.2 V *vs.* Ag/AgCl and appropriately provided a molar value of H_2 production, allowing for some finer comparisons in terms of performable achievement.[28] With these considerations, the

Nernst equation in this thesis primarily serves as the baseline for conversion between reference voltages as needed.

1.3 – Sabatier Principle and Hydrogen Evolution Reactions (HER)

The Sabatier Principle is an important concept in catalysis, particularly heterogeneous catalysis, as the reaction substrate (such as water) must bind or interact in some fashion with the catalyst to create a product.[40,41] Ideally, this interaction should be a balance between overly weak and overly strong. Overly weak means that there will be no interaction of the substate, and overly strong means that the substrate will bind too tightly and fail to dissociate.[30] The latter may result in unfavourable decomposition or modification of the molecular structure of the catalyst or deposition on the electrode.[30]

A graph of the ideal balance of reactions and their general representation with transition metals can be termed a 'volcano plot', marking the metals general location in terms of binding strength and rate of production.[40] An optimal metal such, as platinum, will appear near center of this plot of binding strength and rate of production, placing it at the top of this 'volcano'.[22] This has been demonstrated to directly relate to electrocatalytic activity and Hydrogen Evolution Reactions (HER), in one example by experimentally comparing different metal foils placed in 0.1 M H_2SO_4 solutions connected by a KNO_3 salt bridge.[40] They compare the current density (current divided by surface area of the working electrode) at a selected potential of -1.7 V and compare this against the hydrogen binding Gibbs energies using Density Functional Theory calculations. The

general findings here correlate well with the use of other substrates and without needing electrochemical application, such as with decomposition of formic acid.[42]

However, this applies to the tested metal performing as a smooth and homogeneous surface exposed to the substrate. There are several approaches to modifying the reactivity and selectivity of materials, such as surface area exposure to the substrate (particularly on the atomic level), discrete catalytic sites, or electrode surface modification with conductive materials such as graphene or carbon nanotubes.[31,43,44] These changes can affect the local atomic reactivity/selectivity, modify the electrochemical reduction potentials to be higher or lower, or act as a reduction site in conjugation with the metal.[43] Stability and decomposition can also be supplanted by supporting elements or through surface protection.

Heterogeneous HER is proposed to proceed through step-based mechanisms, namely the Volmer-Tafel mechanism or Volmer-Heyrovsky mechanism.[45] Generally, this refers to the electrochemical adsorption of hydrogen (Volmer – Equation 8), followed by desorption by electrochemical means (Heyrovsky – Equation 9) or chemical (Tafel – Equation 10).[46]

$$H^+ + M + e^- \rightarrow MH_{ads} \quad (8)$$

$$MH_{ads} + H^+ + e^- \rightarrow M + H_2 \quad (9)$$

$$2\,MH_{ads} \rightarrow 2\,M + H_2 \quad (10)$$

The exact mechanism for these steps can be further broken down depending on whether it occurs in neutral/alkaline media or acidic media, primarily identifying water as part of the decomposition process and providing the adsorbed hydrogen in the case of

neutral/alkaline environments.[20] These steps can be rate-determining, with one step proceeding at a significantly faster or lower rate than the other. This relates to the binding strength of the adsorbed species and thus the rate of adsorption and desorption. This impacts onset and overpotential (η) requirements for rates of hydrogen production, although this is modified by the conditions of the electrochemical environment, particularly pH.[15] This can be directly related to voltage changes via the Nernst equation.

1.4 – Outline and Objectives of this Thesis

This thesis covers the exploration of several metal-centered complexes for their ability to function as electrocatalysis for hydrogen production. The primary focus is on using water as the substrate with some exploration of using acetic acid as a substrate. The complexes that were explored centered on 3d transition metals. Specifically, manganese, iron, nickel, and copper complexes were prepared and their ability to perform electrocatalyst was explored. Efforts to employ a set of complexes designed around the 4d-metal molybdenum are also presented. Chapter 2 will focus on the initial exploration of five complexes using manganese and molybdenum, particularly focusing on observed stability and reactions occurring at the electrode. Chapter 3 is a more generalized electrochemical examination of 3d metal complexes supported by macrocyclic ligands. There is a shift to heterogeneous catalysts in Chapter 4 where some copper and nickel complexes were discovered to lead to deposition of heterogeneous materials on the working electrodes. This chapter focuses on characterizing the performance of these materials for hydrogen production.

Chapter 2: Initial Electrocatalytic Exploration using Pyridine-Based Complexes

2.1 – Preamble

In the process of creating a successful homogeneous electrocatalytic complex for hydrogen evolution reaction (HER), several steps must be taken:

- Synthesis of the complex and subsequent characterization, identifying that the desired product was made.
- Examine suitable solvents that the complex may dissolve in and that have an appropriate potential window for the catalytic reaction.
- Employ an innocent electrolyte providing necessary conductivity for the system.
- Perform electrochemical characterization (typically cyclic voltammetry) to identify reduction and oxidation events for the complex.
- Review possible substrates (e.g. water, glacial acetic acid) that could serve as the source of protons for hydrogen generation.
- Examine electrochemical and visual changes with these substrates added, identifying current enhancement if present and matching optimal substrate concentration.
- Subject system to CPE, typically hold a steady chosen potential for a given time period such as 1 h.

- Analyse for products such as hydrogen, by relevant method such as gas chromatography (gaseous product), NMR (liquid/soluble product).

In this chapter, five different complexes will be evaluated for electrocatalytic hydrogen production. Importantly, this will include identifying the impacts of the unintended decomposition of the complexes as part of this process. Full synthesis and experimental details for the complexes will be at the end of the chapter. The focus in this chapter will be on the impacts of electrochemical characterization on the overall stability of the tested complexes from applied voltages. It must be expected that not all electrochemical experiments will result in the desired reaction occurring and unintentional products may result.[30] Within an electrochemical cell, the complex under investigation will be subjected to cathodic and anodic potentials and this may result in the formation of a more reactive species from reduction or oxidation. The catalyst needs to act as a conduit for the transfer of electrons from the electrode to the reaction substrate, ideally lowering the energy required (and likewise potential) for the complete reaction. However, the reaction that occurs may not follow the one that is desired. Some outcomes that may result are irreversible decomposition or conversion of the catalyst, fouling either working or counter electrode, or a new product that remains in solution. These effects might be clearly seen in electrochemical characterization such as cyclic voltammetry (CV) with distortion or elimination of reduction/oxidation peaks, as well as distinct visual changes to the electrodes and electrochemical cell solution. Visual observations are simple, immediately accessible, and can provide valuable information to correlate with acquired CV data.

2.2 – Mn-TPA and Mn-DPA

The initial target was to examine the electrochemical oxidation characteristics of the $[Mn(\kappa^3\text{-TPA})(CO)_3]^+Br^-$ (Mn-TPA) complex. The complex consists of one tris(2-pyridylmethyl)amine (TPA) molecule as a ligand to a central manganese (I) atom bonded through three of the nitrogen groups, leaving one pyridine group uncoordinated (Scheme 2). Three carbonyl groups additionally attach to the manganese atom, and the entire structure is complemented with a bromide counter anion which aids solubility in polar solvents. A similar complex, $[Mn(\kappa^3\text{-DPA})(CO)_3]^+Br^-$ (Mn-DPA), with bis(2-pyridylmethyl)amine (DPA) as the ligand was also selected for investigation. The TPA ligand was synthesized with the identity confirmed by ^1H NMR, with DPA used as received from a supplier. Mn-TPA complex was confirmed by ^1H NMR and high-resolution ESI-MS. Similarly, Mn-DPA complex was confirmed by ^1H NMR and ^{13}C NMR. These complexes had been previously prepared and characterized by our group under reduction potentials for reduction events.[47] Furthermore, the effects of water addition acting as the proton source for hydrogen production via electrolysis had been examined.[47] We now carried out a more thorough examination for the complex's redox behavior, specifically exploring possible oxidation events.

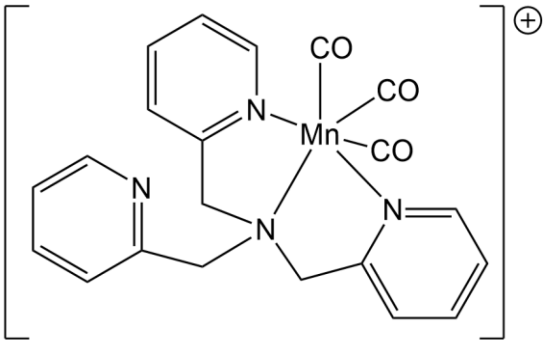

$[Mn(\kappa^3\text{-TPA})(CO)_3]^+Br^-$

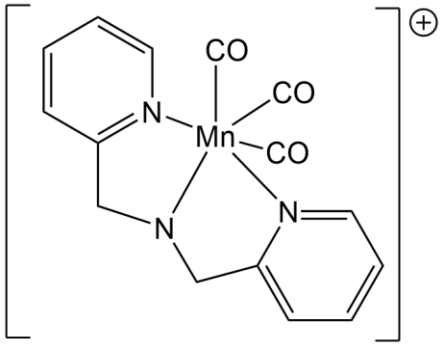

$[Mn(\kappa^3\text{-DPA})(CO)_3]^+Br^-$

Scheme 2: Structures for $[Mn(\kappa^3\text{-TPA})(CO)_3]^+Br^-$ (Mn-TPA) and $[Mn(\kappa^3\text{-DPA})(CO)_3]^+Br^-$ (Mn-DPA) complexes.

To establish a correlation with literature values, CV characterization was first performed in the cathodic region.[47] For Mn-TPA, voltammetry showed three clear, irreversible reduction peaks are observed at -1.95 V, -2.3 V and -2.7 V *vs.* Fc/Fc^+, with associated current strengths of 18 µA, 21 µA, and 18 µA respectively as seen in Figure 3. With water additions, a significant increase was observed for the first peak, growing to 29 µA with 1.4 M water. This peak maximizes at approx. 7.4 M water addition and 57 µA, holding until ~11.1 M before reducing with further additions, 14.8 M indicating 49 µA but retaining a clear, defined peak. The maximum current represents an approx. three-fold increase in current from the baseline, and with this peak being clear and well-defined, it presents good characteristics of enhancement and catalysis with water addition. The second peak at -2.3 V is enhanced and retained until 7.4 M at ~40 µA, at which point the potential window of the system dominates in reduction. The third peak initially observed rapidly becomes no longer observable with addition of water, due to the potential solvent

window of water (reduction of water by the electrode itself) dominating past the -2.3 V region.

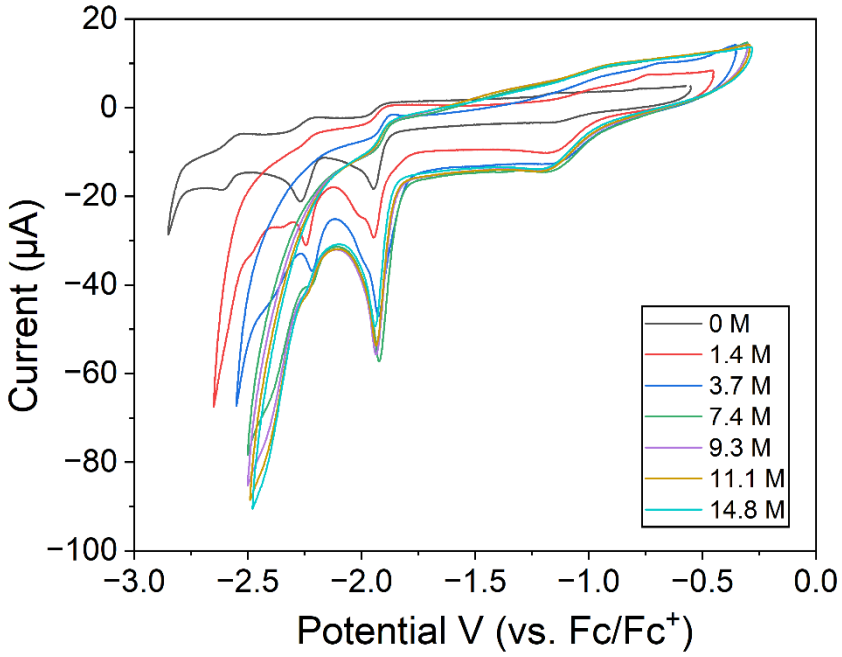

Figure 3: Cyclic voltammetry under cathodic potentials (*vs.* Fc/Fc^{+}) of 1.0 mM Mn-TPA, 0.1 M TBAHFP as electrolyte in 15 mL acetonitrile under N_2 with increasing amounts of water added, noted in legend in molarity. Performed at a scan rate of 100 mV s^{-1}.

The oxidation region for Mn-TPA was examined from 0 to 3.0 V (*vs.* Ag wire) and displayed notable irreversible oxidation events, at 1.03 V with a current of 14 μA and 1.62 V at a current of 24 μA (Figure 4). Note that this experiment is not corrected against ferrocene, as it would overlap the examined potential window. Water was additionally added to examine if oxygen evolution reactions were viable. Water additions shift the oxidation peaks slightly to higher potentials, now appearing at 1.26 V, 1.66 V, and 1.94 V with 0.37 M water present with current strengths of 13 μA, 20 μA, and 27 μA respectively.

Adding additional water to a concentration of 0.74 M further shifts these peaks to 1.40 V, 1.82 V, and 2.12 V and displaying the same current strengths as previously observed. Further additions past 1.0 M quickly flattened these minor peaks, with a possible minor event at 1.27 V at 1.9 M, and 1.44 V at 3.0 M. Generally, these peaks were assessed to be minor, with little opportunity to be explored for catalytic activity.

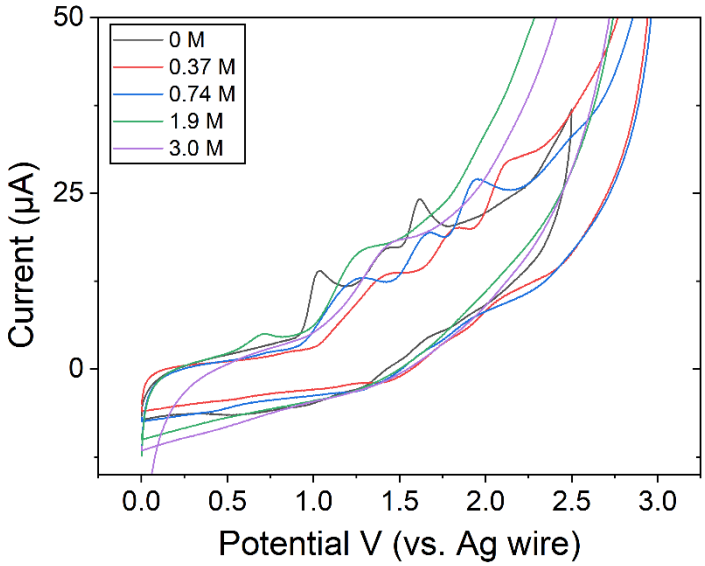

Figure 4: Cyclic voltammetry under anodic potentials (*vs.* Ag wire) of 1.0 mM Mn-TPA, 0.1 M TBAHFP in 15 mL acetonitrile under N_2 at a scan rate of 100 mV s^{-1}.

Following this general electrochemical characterization, hydrogen production was tested using a graphite working electrode at constant cathodic potential of -1.8 V (~-2.1 V *vs.* Fc/Fc^+) for 3600 s with 7.4 M water in 15 mL acetonitrile, with an otherwise identical electrochemical cell setup under CV testing. 7.4 M was chosen due to the maximum enhancement observed here with the first reduction peak. Hydrogen was not detected

with gas chromatography under these set conditions. A subsequent test with 3.7 M water at -1.8 V (~-2.15 V *vs.* Fc/Fc^+) for 3600 s was conducted, with results of 13.0 µmol of H_2 produced. This does provide some level of comparability with reference material, which states an outcome of 16 µmol with 7.4 M water at -2.0 V *vs.* Fc/Fc^+. However, it should be noted that this was a difficult result to acquire, with some lower potentials set at -1.65 V, -1.70 V (uncorrected) for 3.7 M water not yielding a detectable amount of hydrogen. This is likely partially attributable to the use of Ag wire as the pseudo-reference electrode which is unfortunately is not always stable and can demonstrably result in voltage shifts up to ±0.2 V with positioning. This hinders precise calibration of potential if not relying on ferrocene correction, something that may not be present in hydrogen production tests. This would later be addressed with the introduction of an Ag/AgCl reference, a self-contained reference which greatly mitigates this possible level of potential shift and increases accuracy of the electrochemical cell readings.

The visual observations made during these measurements were noteworthy. At this potential of -2.15 V *vs.* Fc/Fc^+, clear visible bubbles were observed coming from the working electrode, a positive outcome in hydrogen generation. However, decomposition and conversion of the Mn complex was clearly present, with the counter electrode tarnished brown and brown specks floating in the solution. Generally, this would suggest the catalyst is structurally changed, with physical deposition on the counter electrode. The exact reason for this occurring is not known, but since oxidation occurs at the counter electrode this was likely related to the changes noted during the anodic scans described above. For some complexes with the TPA ligand, it is noted that 'In water… free and

complexed tpa are in equilibrium' and can create dimeric hydroxo-bridged complexes in water presence.[48,49]

During these tests, it was found that Mn-TPA was soluble in water. This would be the ideal solvent to use for HER, acting as the proton source in hydrogen production by electrolysis, and removing the need for organic solvent as part of the reaction. Therefore, electrochemical testing was performed with 1.0 mM Mn-TPA and 0.5 M NaCl in 15 mL of water. It was found via cyclic voltammetry that the test with Mn-TPA was not significantly different from that of background without catalyst (Figure 5). However, there was an interesting irreversible peak at -1.63 V (*vs.* Ag/AgCl), with a current strength of 69 µA, as compared to 48 µA of background, indicating a reduction of the complex here before reaching the potential window. For CPE analysis of hydrogen production, a potential of -1.8 V (*vs.* Ag wire) was chosen and held for 3600 s. Results from these measurements were unfavourable, with 34.4 µmol of H_2 generated with catalyst but a larger amount of H_2 (95.6 µmol) was obtained in the absence of catalyst. The relatively high amount of hydrogen here is attributed overall to the high overpotential applied here, noting that a minimum potential (onset) must be reached before catalysis/electrolysis of water occurs. With these results, fouling of the counter electrode with brown tarnishing was again observed. This could be removed with a light manual polishing afterward. This electrode fouling may be the reason for the reduced performance as compared to the background without a catalyst. Due to the high total potential of the observed reduction peak, appearance after the onset potential of the background, and negative results under CPE, it was decided to examine a similar catalyst, Mn-DPA.

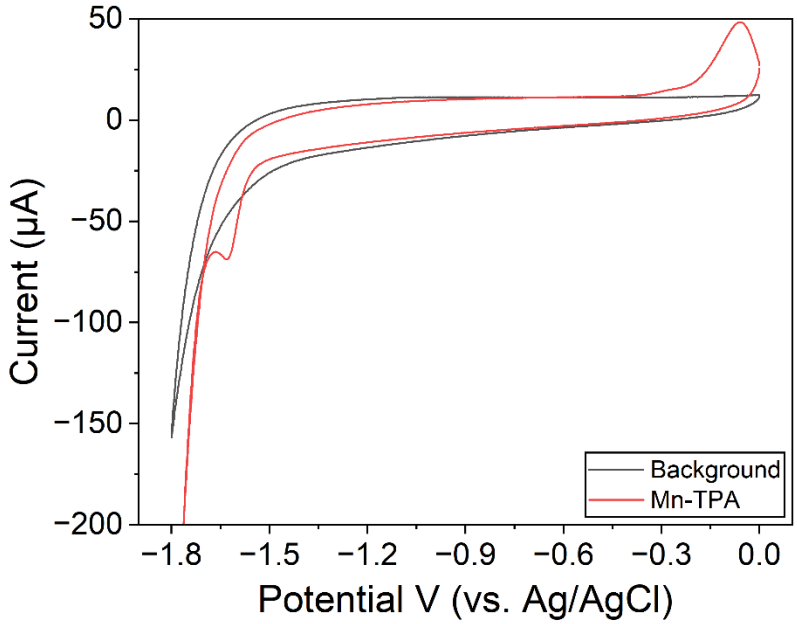

Figure 5: Cyclic voltammetry under cathodic potentials (*vs.* Ag/AgCl) with 1.0 mM Mn-TPA (red) and without (black), 0.5 M NaCl as electrolyte in 15 mL water under N_2 at a scan rate of 100 mV s^{-1}.

Similar to Mn-TPA, a complex of Mn-DPA was prepared to investigate electrochemical activity and to compare it with the Mn-TPA complex. Focusing on the cathodic scans, the first reduction peak is sharp and clear at (~-1.9 V *vs.* Fc/Fc^+), with a slightly lower reduction potential than the first peak of Mn-TPA at -1.95 V (Figure 6). There is a minimal second reduction event at -2.28V which blends into a stronger reduction peak at -2.43 V. The current enhancement response at this first reduction peak with the addition of water appears significantly stronger than that of Mn-TPA. Current enhancement maximized at 6.7 M water at 158 μA *vs.* Mn-TPA of 57 μA at 7.4 M, or

otherwise a five-fold increase in current compared to the three-fold seen with Mn-TPA. Peak enhancement is maintained up to 8.1 M but declines to 106 µA with 10.4 M water present (Figure 7). The second peak at -2.42 V greatly enhances to 95 µA with 1.4 M water. With further additions, this significantly shifts to -2.17 V with 3.7 M present, maximizing with a current strength of 107 µA. Subsequent water addition diminishes this peak, virtually disappearing past 6.7 M.

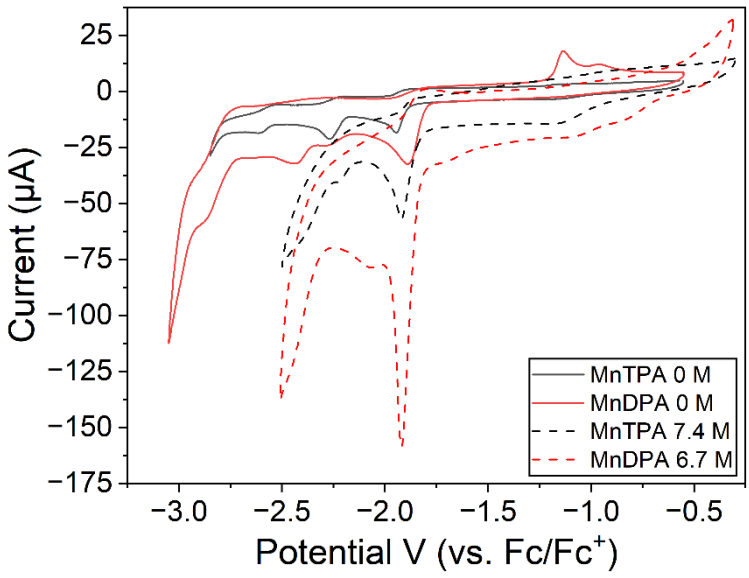

Figure 6: Cyclic voltammetry under cathodic potentials comparing 1.0 mM Mn-TPA (black) and 1.0 mM Mn-DPA (red). Solid lines with no water substrate added are represented with dashed lines with respective listed amounts. Performed in 15 mL acetonitrile solution, 0.1 M TBAHFP under N_2 at a scan rate of 100 mV s^{-1}.

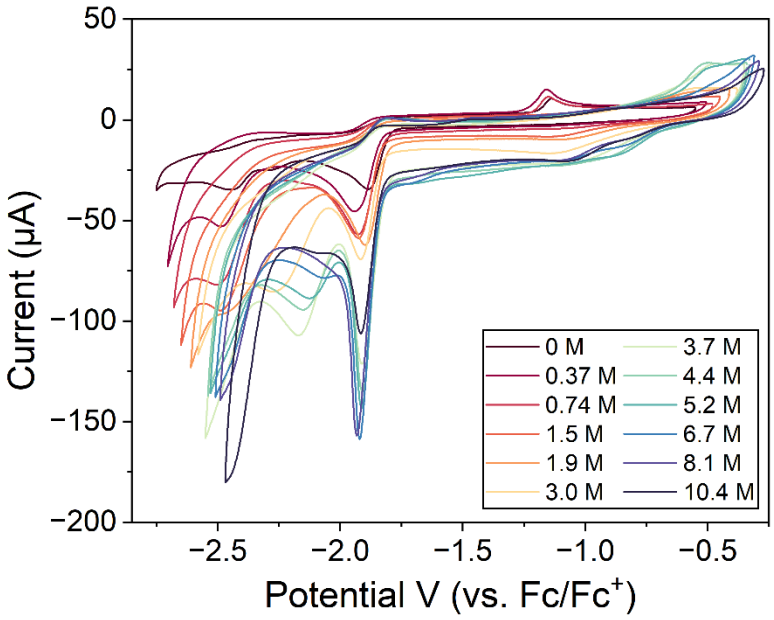

Figure 7: Cyclic voltammetry under cathodic potentials (*vs.* Fc/Fc^+) of 1.0 mM Mn-DPA, 0.1 M TBAHFP in 15 mL acetonitrile under N_2 with increasing amounts of water added as indicated in legend. Performed at a scan rate of 100 mV s^{-1}.

While enhancement is signficant, unfortunately it arises to a similar issue as encountered with Mn-TPA. During electrochemical characterization, decomposition was observed again but in a different manner. Instead of depositing on the counter electrode as a brown coating and turning the solution brown, the working electrode visibly produced what appeared to be a soluble red material (Figure 8). CPE was not necessary to induce this, rather brief CV scans were able to cause this effect. Hydrogen production testing also proved negative, with one experiment of 5.9 M water at -1.75 V (~2.05 V *vs.* Fc/Fc^+) for 3600 s yielded no detectable hydrogen, and 3.7 M water yielded 0.37 µmol, close to negligible. This result however pairs well with the observable decomposition of

product at the working electrode, as well as the brown effluent produced at the counter electrode with applied CPE (Figure 8). Mn-DPA is likely higher in reactivity compared to Mn-TPA with the lack of one pyridine arm and greater degree of access to the metal center with this. This is reflected with the higher enhancement of the first reduction peak with addition water relative to Mn-TPA.

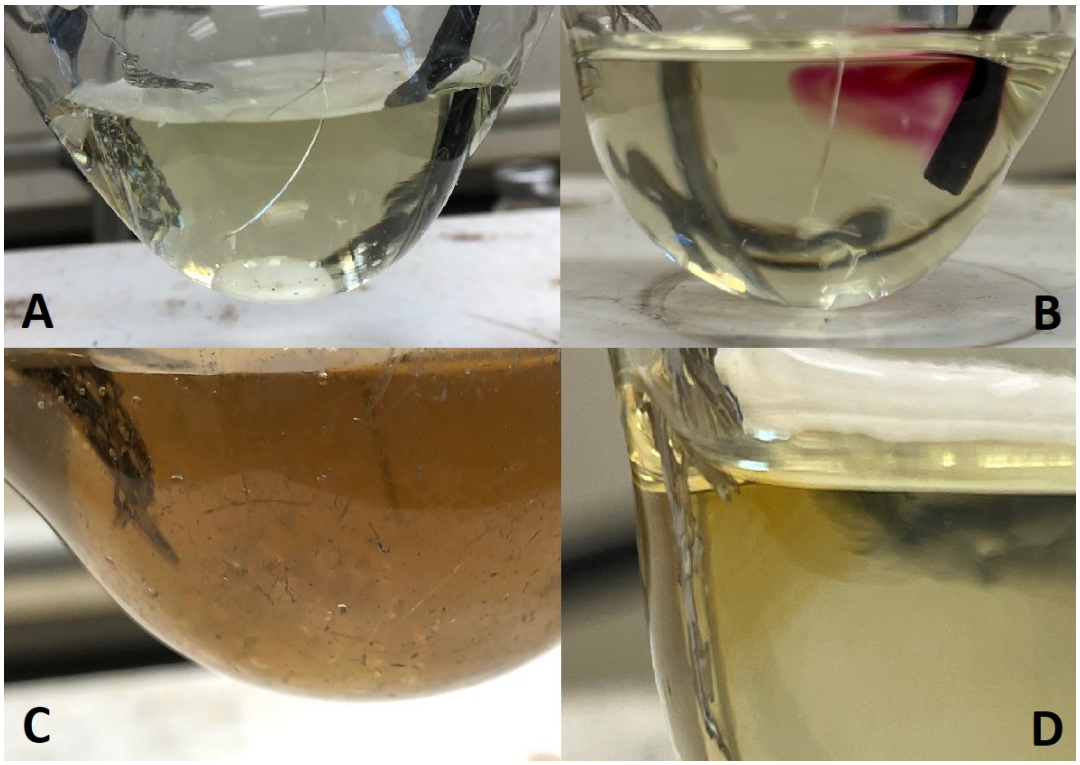

Figure 8: Comparison of visual observations attributable to possible decomposition - (A) Initial visual state in acetonitrile before testing (Mn-TPA/Mn-DPA), (B) 1.0 mM Mn-DPA in acetonitrile solution with 0 M water present during 0 to -2.5 V CV (*vs.* Ag wire), (C) 1.0 mM Mn-TPA in acetonitrile solution with 7.4 M water after applied -1.7 V (*vs.* Ag wire) CPE over 3600 s (D), 1.0 mM Mn-DPA in acetonitrile solution with 3.7 M water present during 0 to -2.5 V CV (*vs.* Ag wire).

2.3 – Mo-TPA

Following these attempts, a similar complex in Mo(κ^3-TPA)$(CO)_3$ (Mo-TPA) was made (Scheme 3). Molybdenum was chosen for a few reasons, with $Mo(CO)_6$ reacting with TPA it would be able to create a similar base structure to Mn-TPA, but would offer differences in being at zero oxidation state versus +1 for Manganese. The Mo-TPA complex was confirmed via ^{1}H NMR, ^{13}C NMR and FTIR.[50,51] Synthesis and experimental details are listed at the end of the chapter.

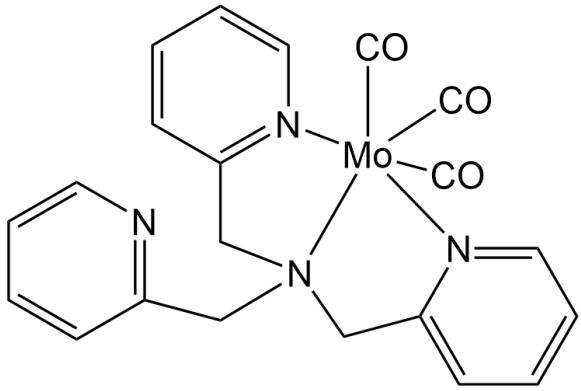

$[Mo(\kappa^3\text{-TPA})(CO)_3]$

Scheme 3: Structure for the [Mo(κ^3-TPA)$(CO)_3$] (Mo-TPA) complex.

An electrochemical cell was set up to assess the electrocatalytic properties of the Mo-TPA sample, and if any reduction of substrate for hydrogen production was possible. The cell was set up to the initial standard 15 mL of acetonitrile or dichloromethane to compare effects of solvents, 0.1 M of TBAHFP, and 1.0 mM of Mo-TPA, while purged under a nitrogen atmosphere. In this initial reading, the variations between the two

solvents are significant (Figure 9). In acetonitrile, an irreversible reduction is seen at -1.34 V (*vs.* Fc/Fc^+), with a large oxidation peak observed at -0.38 V. In contrast, solutions in dichloromethane displayed a reduction peak at -1.54 V with a return oxidation close to the same voltage (-0.45 V) as with acetonitrile, although significantly differing in shape. Furthermore, the dichloromethane solution displayed a larger reduction current and a smaller oxidation than the acetonitrile solution.

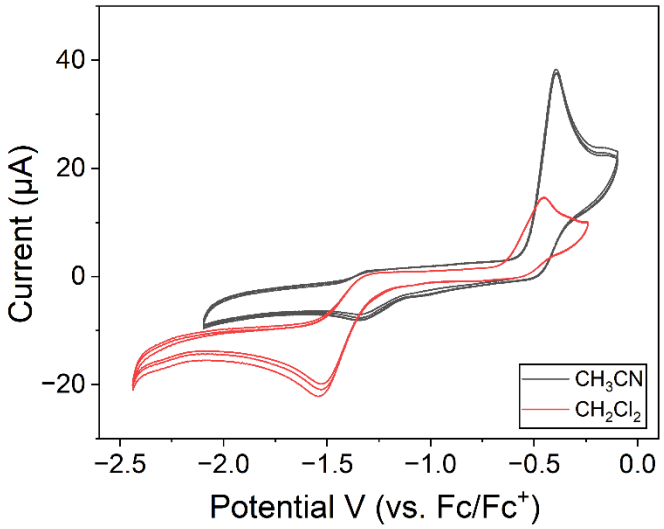

Figure 9: Cyclic voltammetry (*vs.* Fc/Fc^+) of 1.0 mM Mo-TPA in acetonitrile (black), in dichloromethane (red) and 0.1 M TBAHFP as electrolyte.

Literature offers a reference CV in dichloromethane for a similar complex, where the free arm of pyridine is replaced with a benzyl arm.[51] The reference provides an oxidation peak at -0.3 V (*vs.* Fc/Fc^+) and their reduction peak at -0.95 V. Notably, it is stated that the reduction peak only occurs on the second pass, while this is not apparent

during these trials. While it is suspected that the ~-0.4 V oxidation and ~-1.4 V reduction are linked, these peaks were not isolatable by restricting CV scans to each event alone (e.g., 0 to 1.5 V, or 0 to -3.0 V). These trials also exhibit a larger split in relative oxidation and reduction potentials to that of literature – oxidation roughly occurring at the same point (~0.1 to ~0.15 V), but reduction potentials expand past the reference literature. Besides molecular differences of benzyl versus pyridine, there are other differences such as electrolyte (Bu_4NPF_6 vs Bu_4NBr), scan rate used (100 mV s^{-1} vs 200 mV s^{-1}), and ferrocene correction that may provide some ambiguity to reliably compare here.

The ability of the complex Mo-TPA to produce hydrogen from water was then explored. A cathodic scan from 0 V to -3.0 V (uncorrected) in acetonitrile and 0 M water displayed the single irreversible event, with the reduction peak at ~-1.5 V (*vs.* Fc/Fc^+) (Figure 10). Under these conditions the reduction peak was broad and not well-defined. With 0.37 M water to the acetonitrile solution, there was an increase in current from the first reduction peak to 23 μA, and the development of a second peak was observed at -2.15 V. With 1.5 M water, two reduction events shifted to -1.36 V and -1.87 V. These peaks are not particularly strong or well-defined. At 1.9 M water the second reduction event is gone. Increasing the water concentration to 11 M yielded a smaller reduction current at the first reduction at -1.36 V.

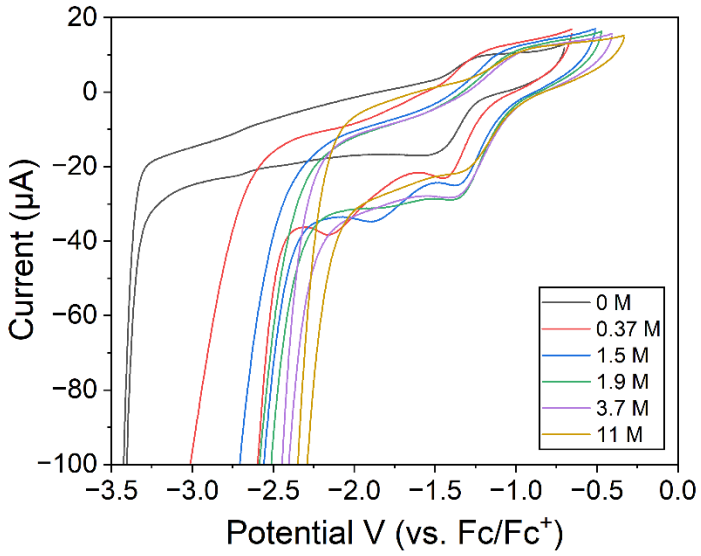

Figure 10: Cyclic voltammetry under cathodic potentials (*vs.* Fc/Fc^{+}) of 1.0 mM Mo-TPA in 15 mL acetonitrile and 0.1 M TBAHFP electrolyte, with the additions of 0.37 M, 1.5 M, 1.9 M, 3.7 M and 11 M water.

It has been reported that acetonitrile solutions of Mo-TPA are oxidized quantitatively in the air to produce a Mo(VI) complex $Mo(O)_3(tpa)H_2O$.[50] While this aspect was not explored in experimentation here in detail, it may account for the CV changes including the appearance of reduction peaks with the presence of water.

With the relatively minor increases in current with water addition and the lack of further notable enhancement with increasing amounts of water, it is suggested that there is no notable catalysis occurring. The development of a second peak which was not observed during initial scans, and with all peaks continuing to shift and even decline could suggest a structural change of the complex taking place. The combination of these factors led to the decision to not pursue hydrogen production attempts with water.

Acetic acid (AcOH) provides an alternative proton source to water and was used for some further investigations of Mo-TPA as shown in Figure 11. In acetonitrile, the first reduction peak at -1.5V appeared to display current enhancement with acetic acid addition. With further additions of acetic acid, this reduction peak shifted anodically to -1.2 V (23 μA) with 0.22 M AcOH and further to -1.1 V (37 μA) with 0.55 M AcOH. The current intensity of this reduction showed a decrease with further addition of acetic acid. Parallel background measurements without Mo-TPA being present are also shown in Figure 11. Interestingly, these experiments gave a larger current response at the same voltages. This suggests that Mo-TPA is not contributing to the current enhancement and that the peak in the -1.12 V region in the presence of acetic acid is wholly attributed to acetic acid alone. While it is noted that the initial current response of the 0 M test is diminished in contrast to the previous comparison in water, possibly indicating the reduced properties of the material (e.g. due to oxidation), this factor alone would not explain the relatively lower current with acetic acid. As a result, no further experiments with Mo-TPA were carried out.

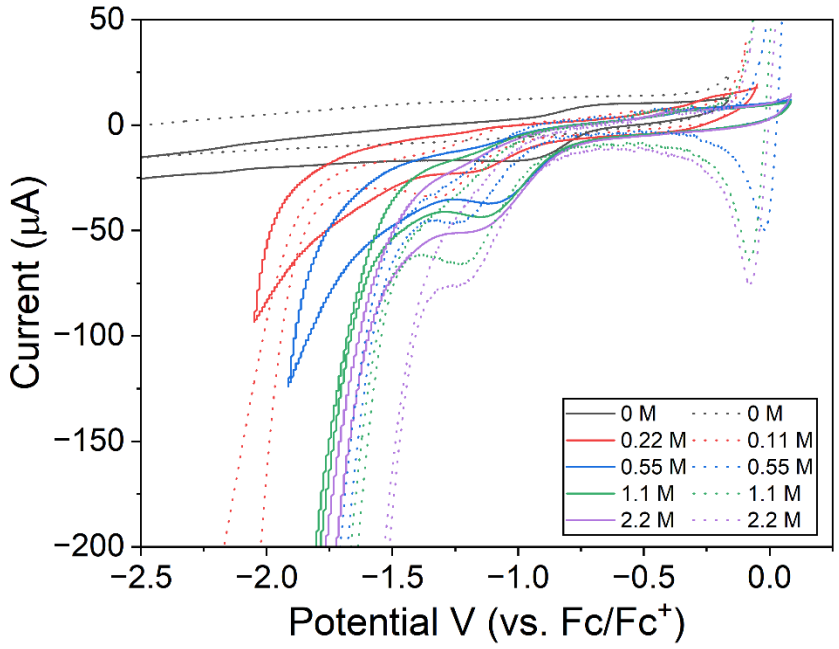

Figure 11: Cyclic voltammetry (*vs.* Fc/Fc^{+}) with 1.0 mM Mo-TPA (solid lines) and without (dotted lines) in 15 mL acetonitrile and 0.1 M TBAHFP electrolyte, with listed amounts of acetic acid present.

2.4 – Mo-DAD and Mo-BPY Complexes

In a search for new complexes that may be suitable for HER, two molybdenum complexes were tested and displayed in Scheme 4. The compounds are termed Mo-DAD ((^{t}BuN)$_2$MoCl$_2$·(^{t}BuDAD^{H})) and Mo-BPY ((^{t}BuN)$_2$MoCl$_2$·bpy)). These compounds were prepared by Michael Land, a PhD candidate from Carleton University, with key characterization performed by him with ^{1}H NMR, ^{13}C NMR, FTIR, melting point and elemental analysis.[52] Both compounds consist of two *tert*-butylimido (^{t}BuN) groups, with Mo-DAD having a 1,4-di-*tert*-butyl-1,3-diazabutadienyl (DAD) group and Mo-BPY having a

2,2'-bipyridine (BPY) group coordinated to the central molybdenum atom. Both of these complexes have Mo in the +6-oxidation state. The main objectives here were to determine electrochemical characteristics with select solvents (acetonitrile, water, dichloromethane), for the primary purpose of hydrogen generation, examined with additions of water and glacial acetic acid as the proton source.

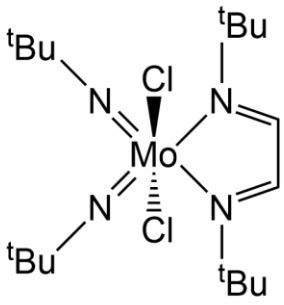

$(^tBuN)_2MoCl_2\cdot(^tBuDAD^H)$

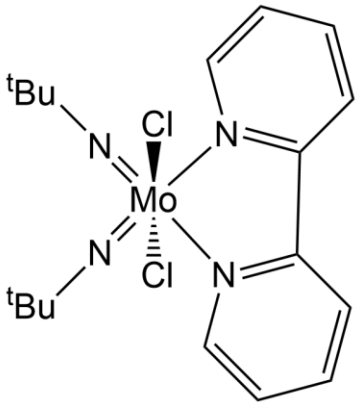

$(^tBuN)_2MoCl_2\cdot BPY$ (Mo-BPY)

Scheme 4: Structure for Mo-DAD ($(^tBuN)_2MoCl_2\cdot(^tBuDAD^H)$) and Mo-BPY($(^tBuN)_2MoCl_2\cdot$bpy) complexes.

For initial examination, 1 mM (7.2 mg) of Mo-DAD was placed into 15 mL acetonitrile and 0.1 M TBAHFP electrolyte with a GC working electrode and a platinum counter electrode. Water additions were incremented to a total of 0.37 M, 1.1 M, 1.9 M, 2.6 M, 3.7 M, 7.4 M, 11.1 M, and 18.5 M. The cyclic voltammetry measurements for solutions with 0 M, 0.37 M, 1.1 M, 1.9 M, and 3.7 M of water are shown in Figure 12. At 0 mL water, an irreversible reduction peak is observed at ~-1.9 V (*vs.* Fc/Fc^+) with the total

current at 37 µA, with no associated oxidation peak visible. No other reduction events are seen before the potential window is reached around -2.6 V. With 0.37 M water addition, the reduction peak significantly increased to 56 µA, and the reduction peak shifted to less negative voltage of -1.71 V. A small oxidation peak also became visible at ~-1.0 V. This relatively large potential shift with the reduction peak is noted even without ferrocene correction (~-1.77 V uncorrected), and so should be noted as likely a structural change in the catalyst. This is correlated with further additions of water. 1.1 M led to a small increase the maximum peak to ~-1.78 V with a current of 63 µA. 1.9 M shows a strong change in this trend, essentially collapsing this peak with further additions.

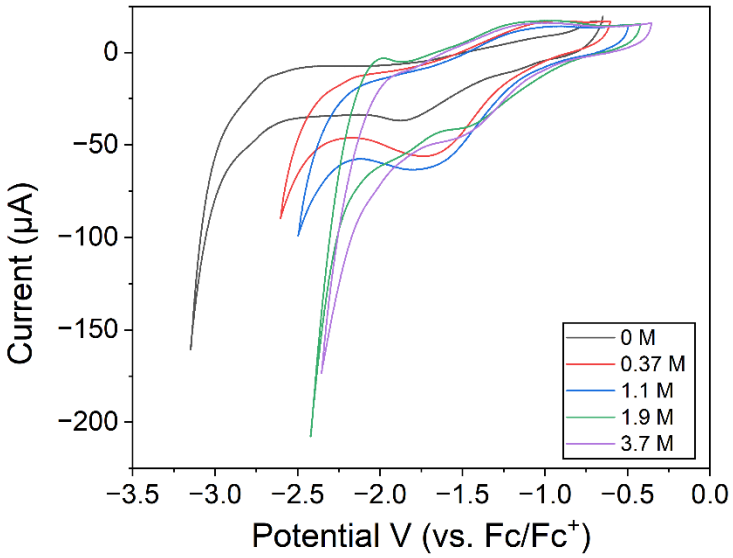

Figure 12: Cyclic voltammetry under cathodic potentials (*vs.* Fc/Fc^+) of Mo-DAD in 15 mL acetonitrile and 0.1 M TBAHFP electrolyte, with the additions of 0.37 M, 1.1 M, 1.9 M, and 3.7 M water.

An examination was subsequently done with dichloromethane as the solvent, in order to verify if solvent served as a key factor, similar to that seen with Mo-TPA. The initial response of the complex gave a more distinct signature, with a reduction peak in the -1.3 to -1.47 V (*vs.* Fc/Fc^{+}) region with a current of 17 µA (Figure 13). Another reduction can be observed at ~-2.2 V. With additions of water from 0.37 M to 1.9 M, the first peak interestingly shifts to a more negative potential (anodically) to -1.77 V with 0.37 M water. 0.74 M brings this peak to -1.66 V, and 1.1 M the reduction event returned to its original potential, at -1.44 V and 25 µA. However further additions diminish this peak. This suggests that 1.1 M is a turning point for water potentially binding with the base complex, as the enhancement maximizes here both in acetonitrile and dichloromethane.

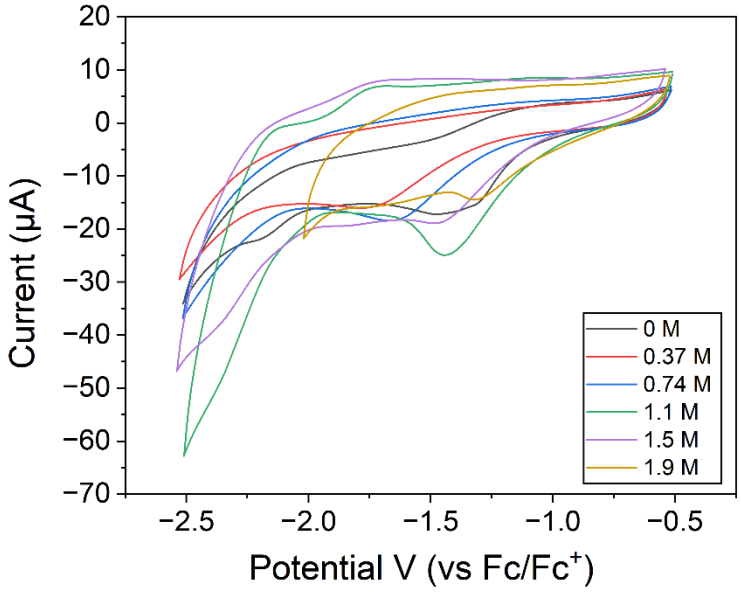

Figure 13: Cyclic voltammetry under cathodic potentials (*vs.* Fc/Fc^{+}) of Mo-DAD in 15 mL dichloromethane and 0.1 M TBAHFP electrolyte, with the additions of 0.37 M, 0.74 M, 1.1 M, 1.5 M, 1.9 M water.

Testing with Mo-BPY followed the same procedure, starting with 15 mL acetonitrile and 0.1 M TBAHFP electrolyte. The first CV from -0.65 V to -2.15 V (*vs.* Fc/Fc^{+}), where an overlapping trend develops at the first reduction peak at -1.79 V with a current of 54 µA, as seen in Figure 14. The next scan from -0.65 to -3.15 V overlays the first reduction peak as well as a second reduction peak at -2.7 V. However, there are some changes to the first reduction peak at -1.79 V with continuous scans, as it appears to shift to more negative voltage and decrease in current. This could be seen in this instance of a CV scan, where continuous scans out to -3.15 V fairly rapidly degrades and flattens the first peak at -1.79 V. This same behaviour does not occur with the first scan limited from -0.65 V to -2.15 V, with the peak remaining constant at the same current strength. One possibility is that by reaching this second reduction point of the complex (past ~-2.7 V (*vs.* Fc/Fc^{+})) an irreversible transformation by reduction occurs and influences the first reduction peak. If the structure of the complex is irreversible change (by such that a ligand component is removed), then reversibility is diminished, and the observed peaks gradually decline. This concern would be correlated during later testing with acetic acid additions.

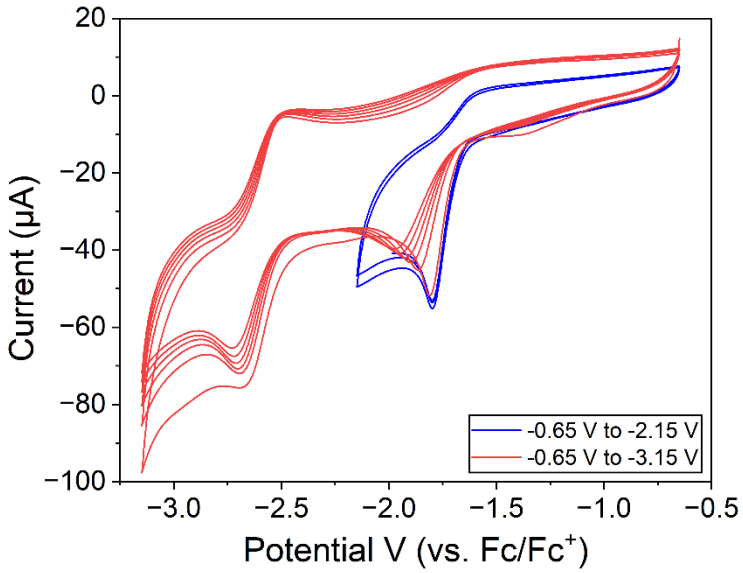

Figure 14: Cyclic voltammetry under cathodic potentials (*vs.* Fc/Fc^{+}) of Mo-BPY in 15 mL acetonitrile, 0.1 M TBAHFP with no added substrate, starting from -0.65 V to -2.15 V (blue) performed first, and -0.65 V to -3.15 V (red) performed second at a scan rate of 100 mV s^{-1}.

From here, testing with water additions to the complex in acetonitrile was carried out. Additions were made from 0.37 M to 11 M, with choice additions highlighted in Figure 15 for clarity. Immediately with 0.37 M addition, a significant change is seen in the appearance of two reduction peaks at ~-1.9 V and ~-1.55 V (*vs.* Fc/Fc^{+}). These reduction events continue to change with increasing water concentration. This could be explained by the coordination of water molecules to the complex, particularly directly to the molybdenum atom where chloride is present. This type of coordination is fairly common where accessibility to these halides allows substitution, especially in high polar solvents such as water.[53] Further additions of water nominally enhance this peak to a maximum current of 57 µA at -1.29 V at 3.7 M water.

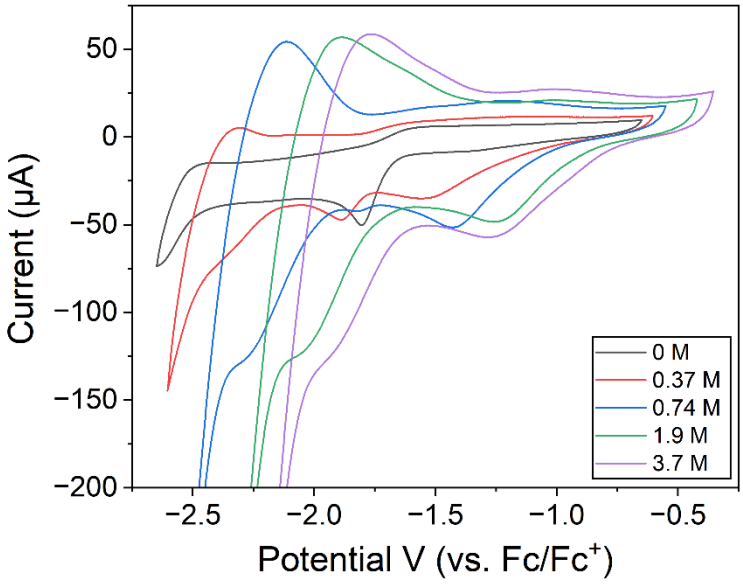

Figure 15: Cyclic voltammetry under cathodic potentials (*vs.* Fc/Fc^{+}) of Mo-BPY in 15 mL acetonitrile with water additions of 0 M, 0.37 M, 0.74 M, 1.9 M, and 3.7 M, scanning from 0 to -2.0 V at a scan rate of 100 mV s^{-1}.

Overall, the performance observed with the addition of water does not particularly suggest HER catalytic activity, with a minimal increase of current from 50 µA to 57 µA. The indication that the original peak was eliminated with the creation of a new peak is not typically associated with favourable results, due to materials trending to more stable configurations where possible in the local environment. Pairing with these results are visual observations indicating strong changes with small additions of water. The initial colour of the solution with no water present was transparent yellow. At 0.74 M of water present, the solution turned clear, and at 1.9 M the solution became cloudy white. Colour change is a distinct indicator that one of the substrates is being modified, most commonly

this being the complex present in the solution, and this correlates strongly with the significant shift in peaks detected in CV.

With the observation that minor amounts of water caused a rearrangement of the detected CV peaks with no notable enhancement of current, it was decided to investigate the electrochemical effects of adding acetic acid to this complex, serving as a proton source. In the presence of acetic acid and correlating with the previous tests regarding potential window limits (Figure 14), it was determined that scans out to -3.15 V (*vs.* Fc/Fc^+) would induce a dramatic shift in the overall electrochemical chemistry as compared to restricting scans to -2.15 V (Figure 16). With 0.02 M addition of acid, the CV displayed a reduction at -1.90 V (*vs.* Fc/Fc^+). However, the sample that was scanned to -3.15 V shows a smaller current comparatively. Background in the absence of complex shows some effect from the acetic acid addition, but no significant reduction at -1.90 V. This large difference in potential is theorized to be attributed to decomposition and fouling of the electrodes, as reduction of acetic acid should parallel that of background as a maximum reduction point. Likewise, this is beyond the possible variance of Ag wire placement and ferrocene correction, with the relative maximum impact of those potential variables being approx. ± 0.2 V at extremes. Visual observations of the working electrode indicated mild tarnishing and blackening, but further testing such as polishing and re-insertion of the working electrode was not performed. Rather, test conditions were adjusted to restrict the potential to -2.2 V (*vs.* Fc/Fc^+), with positive results thereafter in regard to total enhancement with acetic acid.

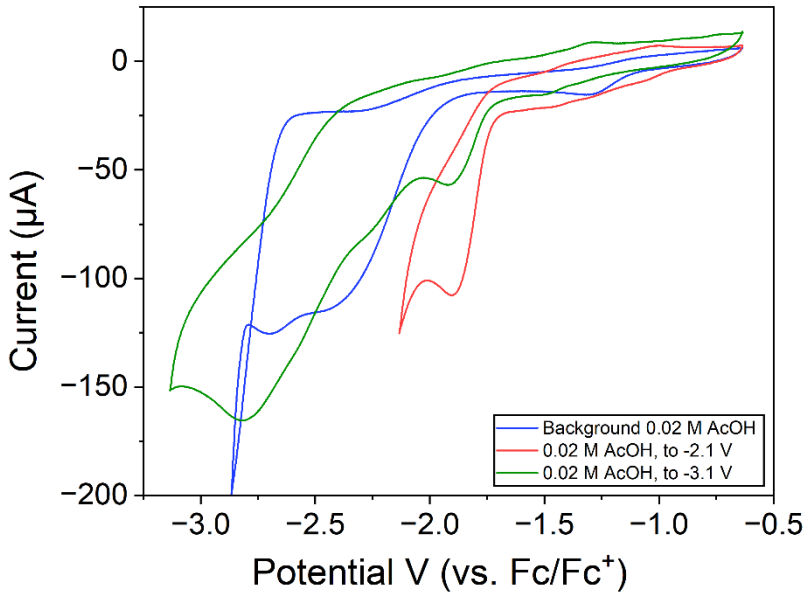

Figure 16: Cyclic voltammetry under cathodic potentials (*vs.* Fc/Fc^+) of 1.0 mM Mo-BPY and background in acetonitrile with 0.02 M AcOH additions. Background without catalyst present (blue), Mo-BPY scans from 0 to -3.1 V (red), Mo-BPY scans from 0 to -2.1 V (green).

With the restrictions for cyclic voltammetry set to a maximum of -2.2 V (*vs.* Fc/Fc^+), sequential additions of acetic acid were performed with and without catalyst present. The most significant enhancements and deviation from background occurred at low amounts of acetic acid present, with 0.01 M enhancing the peak at -1.79 V (*vs.* Fc/Fc^+) from a relative 53 µA to 112 µA peaking at -1.91 V, as seen in Figure 17. The relative background current here at -1.91 V increases from 8 µA to 15 µA in comparison. With 0.04 M AcOH the current enhancement remains favourable with 108 µA *vs.* 45 µA, with and without catalyst respectively, although the peak has lost some definition and background is beginning to increase (Figure 17). As an alternative method to highlight overpotential

requirements, using 100 µA as a comparison point, the 0.04 M AcOH solution with catalyst present requires -1.86 V to that of -2.03 V for background.

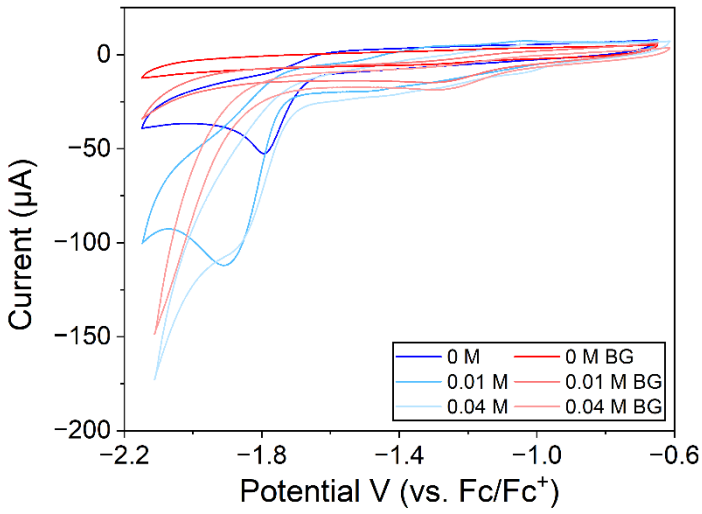

Figure 17: Cyclic voltammetry comparison under cathodic potentials (*vs.* Fc/Fc^{+}) of 1.0 mM Mo-BPY in 15 mL acetonitrile, 0.1 M TBAHFP with complex present (blue) and background (red). Increments of 0.01 M and 0.04 M AcOH are shown with complex present (light blue) and background (light red).

The background continued to increase parallel to that with catalyst present, up to the maximum with 0.62 M AcOH. Here a reduction peak associated with acetic acid dominates at around -1.25 V at 30 µA, with full onset reduction continuing soon after around -1.4 V (Figure 18). The presence of catalyst nominally improves this initial peak to 37 µA, but soon after trends close to that of background. Full graphing of the additions of AcOH, with and without catalyst, can be seen in Figures 19 and 20.

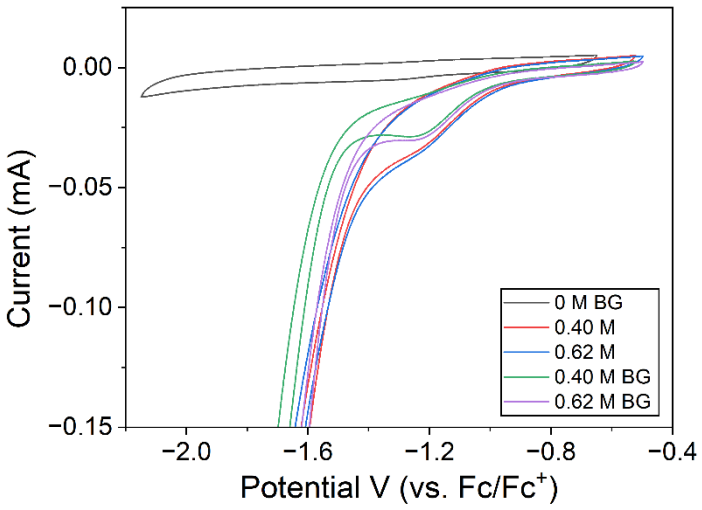

Figure 18: Cyclic voltammetry comparison under cathodic potentials (*vs.* Fc/Fc^{+}) of 1.0 mM Mo-BPY in 15 mL acetonitrile, 0.1 M TBAHFP with complex presence in 0.40 M AcOH (red) and with 0.62 M AcOH (blue). Without complex or substrate present (black) and with 0.40 M, 0.62 M AcOH (green/purple).

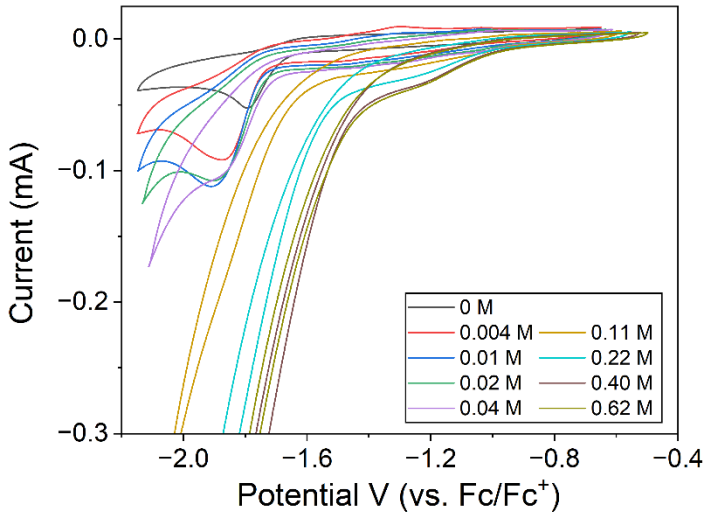

Figure 19: Cyclic voltammetry under cathodic potentials (*vs.* Fc/Fc^{+}) of 1.0 mM Mo-BPY in 15 mL acetonitrile, 0.1 M TBAHFP with catalyst present, scaling from 0 M to 0.62 M AcOH additions.

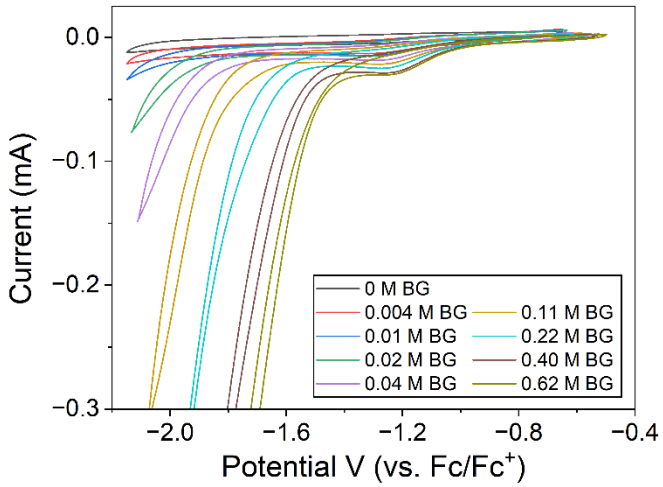

Figure 20: Cyclic voltammetry under cathodic potentials (*vs.* Fc/Fc^+) of 1.0 mM Mo-BPY in 15 mL acetonitrile, 0.1 M TBAHFP without catalyst present, scaling from 0 M to 0.62 M AcOH additions.

With the possibility of usable catalytic activity observed with Mo-BPY, CPE was performed with an applied potential of -1.17 V (*vs.* Ag wire, -1.75 V *vs.* Fc/Fc^+) over 3600 s with a concentration of 0.11 M AcOH. This potential was chosen to target the initial E_{cat} of the reduction peak at 0 M seen at -1.79 V (*vs.* Fc/Fc^+), with the amount of acetic acid chosen to modestly surpass the minimum amounts required, expecting some possible consumption of the substrate over time. However, this potential was determined to be likely too low to be effective, as the average hydrogen detected over three runs was calculated to be 0.6 ± 0.36 µmol H_2, generally determined to be too close to negligible. Therefore, the potential was increased to -1.35 V (*vs.* Ag wire, -1.93 V *vs.* Fc/Fc^+), with trials covering 0.04 M, 0.33 M, and 0.55 M AcOH. With these new parameters, 0.04 M AcOH yielded positive results, with 2.2 µmol H_2 detected compared to the background of 0.02 µmol. These results indicate a slight capability for hydrogen production above that

of background, although the total amounts of H_2 remain negligible. The trials at 0.33 M were less clear, with 15.0 µmol and 13.2 µmol H_2 obtained with and without catalyst respectively. This is further correlated with trials at 0.55 M AcOH, providing results of 28.4 µmol and 30.6 µmol H_2 obtained with and without catalyst respectively. At these higher acetic acid concentrations, it is less clear if the complex is positively contributing to H_2 production. These trials were not extensively repeated since there was little if any difference between background and catalyst trials.

Visual observations during these CPE experiments highlight significant changes during experiments carried out with -1.17/-1.35 V (*vs.* Ag wire), as seen in Figure 21. The original state of solution changes from transparent yellow to a bright reddish hue, only occurring in the presence of Mo-BPY. This process gradually occurs over the timeframe of applied potential becoming more deeply coloured. With the sample transferred to a non-N_2 purged vial, the colour does fade gradually over the course of hours in open air. The colour is likely lost due to oxidation of the product with atmospheric exposure.

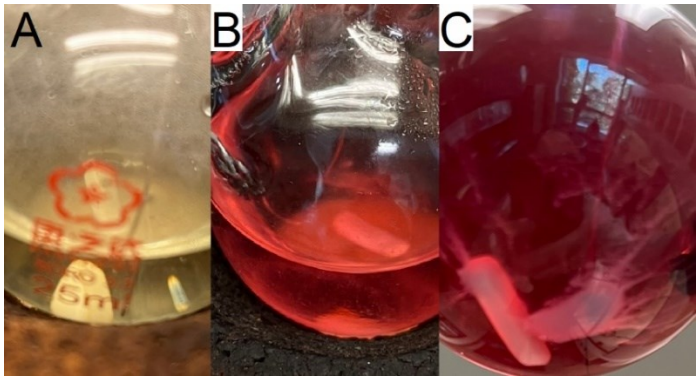

Figure 21: Comparison of 1.0 mM Mo-BPY to initial state in acetonitrile with catalyst present, no substrate added (A), with 0.11 M AcOH present and after 3600 s CPE at -1.17 V (*vs.* Ag wire) (B), with 0.55 M AcOH present and after 3600 s CPE at -1.35 V (*vs.* Ag wire) (C).

In this chapter, we have covered several differing complexes, both in metal centers and ligand structures. We have observed the variations in cyclic voltammetry results that they may produce, with and without added substrate. Furthermore, we can observe the effects of substrate addition and applied reduction potentials on visual observations of the experiment and potential outcomes for the end objective of effective hydrogen production versus background. An important consideration is that enhancement of a known reduction peak is a good indicator of a type of catalytic process occurring, but this does not necessarily lead to the desired reaction (e.g. hydrogen production). Conversion of the catalyst into another form, seen as decomposition and fouling of the electrodes, both counter and working electrodes is key to recognize as part of the analysis process. Occasionally, however, conversion of the catalyst and even fouling of the electrode may result in remarkably positive attributes, as will be further explored in Chapter Four.

2.5 – Experimental Details

2.5.1 – General Methods

Commercial reagents were purchased from Sigma-Aldrich, Alfa-Aesar and TCI America and were used without further purification. Synthesis reactions that were performed in an inert atmosphere were conducted under nitrogen. NMR spectra measurements were carried out on a Bruker Avance II 400 instrument at room

temperature. ESI-MS was performed on a Waters SYNAPT G2 High-Definition Mass Spectrometer. Electrochemical measurements were performed on a Princeton Applied Research VersaSTAT 3 Potentiostat (Mn-TPA, Mn-DPA) and PGZ 301 VoltaLab Potentiostat (Mo-TPA, Mo-DAD, Mo-BPY). Gas chromatography measurements were performed using an Agilent 7820 A equipped with a thermal conductivity detector (TCD) and Agilent select permanent gases column. For detection of hydrogen gas, gas samples of 200 µL were taken using a 250 µL gas tight syringe, extracted from the headspace of the electrochemical cell. Hydrogen molar quantities were calculated from the detected area (µV·s) by GC-TCD from a prepared hydrogen calibration curve.

2.5.2 – Electrochemical Cell Setup

Electrochemical characterization of the complex was performed in a 40 mL three-neck flask with a glassy carbon working electrode for CV characterization, a silver wire as the reference electrode, and a platinum wire for the counter electrode. A graphite rod for the working electrode and a platinum mesh as the counter electrode were used when CPE hydrogen production experiments were performed. The regular cell standard is 15 mL of acetonitrile, 0.1 M of TBAHFP, and 1 mM of examined sample, while purged under a nitrogen atmosphere. When water was the solvent, an Ag/AgCl reference electrode (3 M KCl) was used in place of the silver wire.

2.5.3 – Synthesis of Tris(2-pyridylmethyl)amine (TPA) Ligand

Synthesis of the Tris(2-pyridylmethyl)amine (TPA) ligand – 0.25 mL of 2-picolylamine (1.049 g/mL, 108.14 g/mol, 2.4 mmol), 0.475 mL of 2-pyridinecarboxaldehyde (1.126 g/mL, 107.11 g/mol, 4.99 mmol), 1.56 g of sodium triacetoxyborohydride (211.94 g/mol, 7.36 mmol) acting as the catalyst were added in an approximate 1:2:3 molar equivalence to 37.5 mL of dichloromethane. The mixture was stirred in a closed 100 mL round bottom flask for two days at room temperature. Solution was orange before and after this time period. At that point, 37.5 mL of saturated $NaHCO_3$ was poured into the flask, continuing the previous stirring for 30 min at room temperature. Immediate foaming occurred with a visible separation of two layers over a few minutes, a clear-orange top layer for water and an opaque-orange bottom layer for dichloromethane, with some foaming continuing at the interface between the two layers. The foaming is indicative of the sodium bicarbonate neutralizing excess acid from the reaction process. This mixture was poured into an extraction funnel with 25 mL of ethyl acetate added to separate components further. After extraction, the bottom layer of dichloromethane was retained as the organic layer and this extraction was passed through a large filter with a large amount of sodium sulfate as a drying agent. The remaining solvent was removed by rotary evaporation, yielding an orange-brown oil. This oil was washed thoroughly and repeatedly in the same flask using pentane to capture the desired product, with the pentane kept and placed in a 100 mL beaker. The pentane was left to evaporate overnight, and a yellow-orange solid remained, weighing 0.615 g (87% yield). ^1H NMR spectra with $CDCl_3$ of this material compared well with reported TPA.

2.5.4 – Synthesis of Mn-TPA, Mn-DPA, and Mo-TPA

Synthesis of the Mn-TPA: In a nitrogen filled glovebox, 0.351 g of the TPA ligand (290.36 g/mol, 1.21 mmol) and 0.323 g of $Mn(CO)_5Br$ (274.892 g/mol, 1.18 mmol) and 18 mL of THF was placed in a 50 mL round bottom flask. This flask was covered in aluminum foil to protect the reaction mixture from ambient light and sealed before being taken out of the glovebox and brought to a purged vertical condenser and carefully attached with steps taken to minimize oxygen contamination. The flask was stirred and heated to reflux for 2 h, with a large amount of yellow precipitate formed after this time period. The solution and precipitate were passed through a Fisher Scientific P8 coarse filter paper, washed with additional THF and the remaining product was left to dry overnight in an open vial. The final product was a 0.420 g yellow powder (product 429.0759 g/mol, 83% yield). Reported yield for Mn-TPA synthesis is 82% from literature.[47] The identity of Mn-TPA was confirmed by comparison of the ^1H NMR in dimethyl sulfoxide-d_6 and by high resolution ESI-MS to reported values.[47] General reaction scheme is provided in Scheme 5.

Synthesis for the Mn-DPA complex followed the same procedure as for Mn-TPA, using 0.167 g (0.838 mmol) of bis(2-pyridylmethyl)amine (DPA) in place of the TPA ligand. 0.225 g (0.818 mmol) of $Mn(CO)_5Br$ with DPA was dissolved in 25 mL of THF, refluxing for a period of 2 h. The resulting precipitate was filtered with coarse filter paper and dried in air, resulting in a beige powder. The final mass was 0.231 g with a yield of 68%. The identity of Mn-DPA was confirmed by comparison of the ^1H NMR in dimethyl sulfoxide-d_6 with reported values.[54] General reaction scheme is provided in Scheme 5.

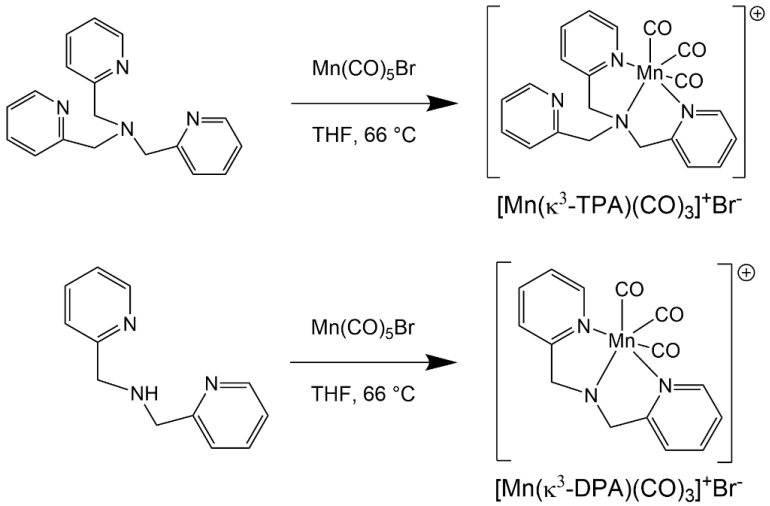

Scheme 5: Reaction schemes for the synthesis of $[Mn(\kappa^3\text{-TPA})(CO)_3]^+Br^-$ (Mn-TPA) and $[Mn(\kappa^3\text{-DPA})(CO)_3]^+Br^-$ (Mn-DPA) complexes.

Synthesis of the Mo-TPA Complex: 0.249 g of the TPA ligand (290.36 g/mol, 0.858 mmol), and 0.206 g of $Mo(CO)_6$ (264.026 g/mol, 0.780 mmol) and 15 mL of ethanol was placed in a 50 mL round bottom flask. This flask was purged with nitrogen, and after reagents added, covered in aluminum foil to protect from ambient light. This flask was brought to a nitrogen-purged vertical condenser with attention to maintain a purged state. The initial solution was a deep red brown colour. The flask was stirred and placed under reflux for 2 h, with an observable large amount of reddish-orange precipitate formed after this time period. The solution and precipitate were passed through a paper filter, washed with additional ethanol and left to dry overnight. The final product was a 0.221 g orange powder, 59% yield of Mo-TPA with visual appearance matching description of literature. The identity of Mo-TPA was confirmed by comparison of FTIR and ^1H, ^{13}C NMR in dimethyl sulfoxide-d_6 with reported values.[50,51]

Chapter 3: Macrocyclic Complexes

3.1 – Preamble

With the findings of instability and decomposition from the previous complexes, the search for electrocatalytic complexes shifted to a different family of macrocyclic complexes. Rather than relying on a ligand that partially encloses the metal ion with tri-dentate/bi-dentate arms, macrocyclic complexes with a closed-ring ligand are reported to be stable and resistant to acids and alkalis.[55] In this chapter, we will cover the synthesis and electrochemical characterization for a number of macrocyclic complexes. These complexes will be based around the complexes of Mn(II), Fe(III), Ag(I), and Ni(II) using quinquedentate N_5 and N_3O_2 macrocyclic ligands.[56] A brief description of the synthesis procedure will be provided, with in-depth synthesis and characterization details provided at the end of the chapter. In establishing a naming convention for these complexes, these are synthesized with two ligand components. Since 2,6-diacetylpyridine (2,6-dap) is common to all of these compounds it was not used in the abbreviated naming (Scheme 6, left). The second main ligand component was a diamine and was the variable component of the ligands, consisting on one of 1,8-diamino-3,6-dioxaoctane (1,8-dia), triethylenetetramine (TETA), or 1,2-bis(3-aminopropylamino)ethane (1,2-bis) (Scheme 6, right).

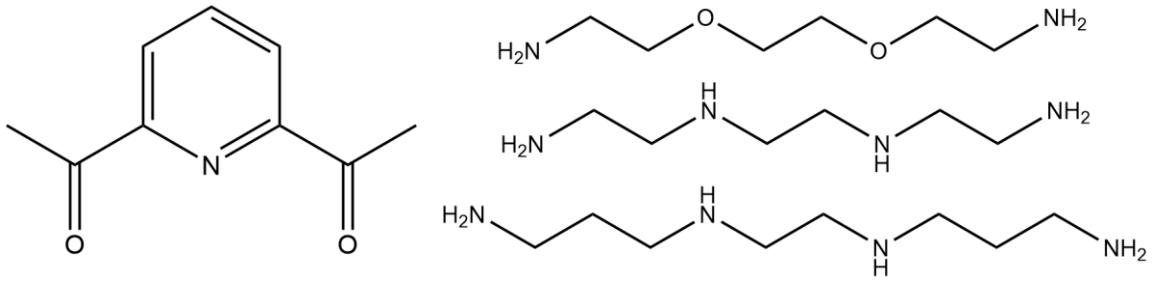

Scheme 6: Molecular structures for 2,6-diacetylpyridine (left), 1,8-diamino-3,6-dioxaoctane (top right), triethylenetetramine (center right), and 1,2-bis(3-aminopropylamino)ethane (bottom right).

Simplifying a naming convention for the complexes, the complex names will be the metal, followed by the number and nature of the coordinated elements attached to the metal center with the complete complex (e.g., Mn3N2O). In the case of identical metals, the oxidation state will be noted (Fe^{3+}3N2O, Fe^{2+}3N2O). To differentiate between triethylenetetramine and 1,2-bis(3-aminopropylamino)ethane complexes, a suffix denoting the number of carbons present between the nitrogen atoms will be placed, as they differ primarily in that manner (e.g., Mn5N-2,2,2 for triethylenetetramine complexes, Mn5N-3,2,3 for 1,2-bis(3-aminopropylamino) complexes.

The macrocyclic complexes covered in this chapter will be for initial attempts to create Mn3N2O, Fe^{3+}3N2O, Fe^{2+}3N2O, followed by an alternative synthesis to create Mn3N2O, Mn5N-2,2,2, Mn5N-3,2,3, Fe5N-2,2,2 and Ni5N-3,2,3. Ag5N-3,2,3 is synthesized as an precursor to Ni5N-3,2,3 synthesis via transmetalation. The full names for the complexes explored are as follows in Table 1 and shown in Scheme 7. Mn3N2O was not characterized by single crystal XRD, with the basic proposed structure in Scheme

7. The preliminary investigation section complexes in Section 3.2 are not included due to them being determined as early unsuccessful syntheses.

Table 1: Full nomenclature for main complexes explored in Chapter 3 and associated short name version.

Full Nomenclature	Short Name
Diaqua-(2,13-dimethyl-6,9-dioxa-3,12,18-triazabicyclo[12.3.1]octadeca-1(18),2,12,14,16-pentaene-κN^3,κN^{12},κN^{18},κO^6,κO^9)-manganese(II) perchlorate chloride	Mn3N2O
Diaqua-(2,13-dimethyl-3,6,9,12,18-pentaazabicyclo[12.3.1]octadeca-1(18),2,12,14,16-pentaene-N^3,N^6,N^9,N^{12},N^{18})-manganese(II) perchlorate chloride	Mn5N-2,2,2
Chloro-(2,15-dimethyl-3,7,10,14,20-pentaazabicyclo[14.3.1]eicosa-1(20),2,14,16,18-pentaene-N^3,N^7,N^{10},N^{14},N^{20})-aquamaganese(II) perchlorate	Mn5N-3,2,3
Dichloro-(2,13-dimethyl-3,6,9,12,18-pentaazabicyclo[12.3.1]octadeca-1(18),2,12,14,16-pentaene-N^3,N^6,N^9,N^{12},N^{18})-iron(III) perchlorate	Fe5N-2,2,2
(2,15-dimethyl-3,7,10,14,20-pentaazabicyclo[14.3.1]eicosa-1(20),2,14,16,18-pentaene-N^3,N^7,N^{10},N^{14},N^{20})-silver(I) perchlorate	Ag5N-3,2,3
Methanol-(2,15-dimethyl-3,7,10,14,20-pentaazabicyclo[14.3.1]eicosa-1(20),2,14,16,18-pentaene-N^3,N^7,N^{10},N^{14},N^{20})-nickel(II) diperchlorate	Ni5N-3,2,3

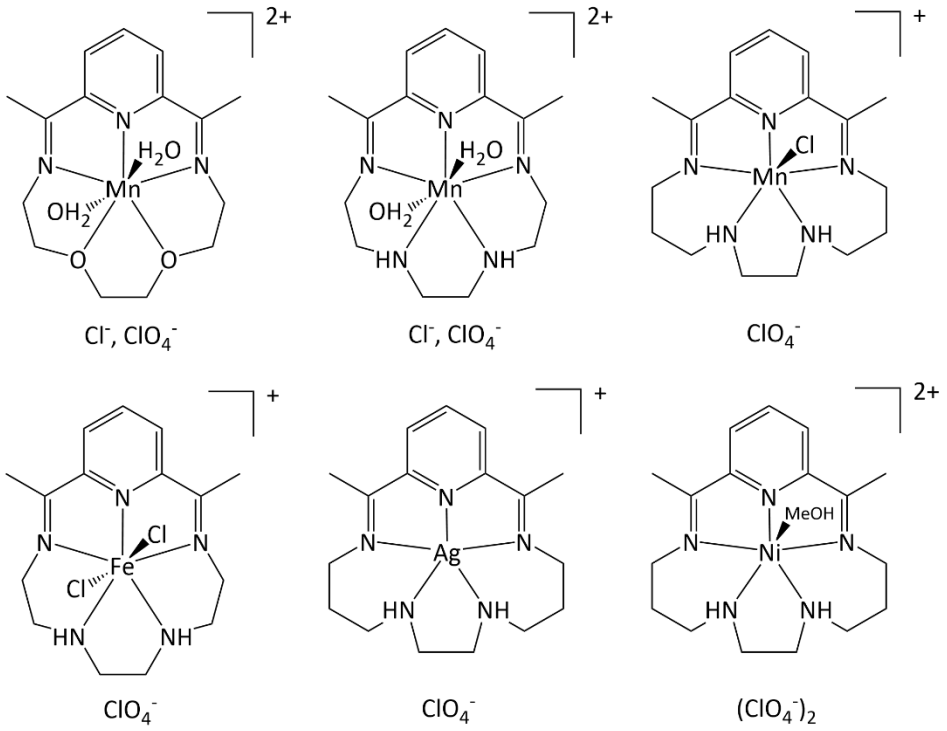

Scheme 7: Schematic structures for main complexes in Chapter 3.

Some inspiration for exploring these macrocycle complexes came from the work of Wang et al. (2019).[57] This reference covers the use of four macrocyclic complexes with variation of the metal centers between $Co^{2+}/Mn^{2+}/Fe^{3+}/Zn^{2+}$ and compared their reduction events and HER catalytic behavior in the presence of aqueous pH 7.0 sodium phosphate buffer solution. Cobalt in particular showed a strong catalytic response at a peak of -1.1 V (*vs.* NHE), with a significant increase in current density 0.5 mA cm^{-2} to ~3.5 mA cm^{-2}. CPE experiments at this potential were found to produce hydrogen, with an output of 390 mol H_2 (mol catalyst)$^{-1}$ h^{-1} cm^{-2} and a Faradaic efficiency of 99 ± 4% under 20 µM concentration, 1 hr timeframe and 1.0 cm^{-2} working electrode. This result may be tempered with the fairly high overpotential requirements of 680 mV (*vs.* NHE) for this

work, but otherwise highlights a foundation for macrocycle molecular synthesis and electrochemical analysis with substrate addition.

3.2 – Initial Investigation with 3N2O Complexes

Three macrocycles were planned with Mn^{2+}, Fe^{3+} and Fe^{2+}, with 2,6-diacetylpyridine and 1,8-diamino-3,6-dioxaoctane as the ligand components (Scheme 8). Critically, this synthesis calls for the use of 1:1 water/ethanol with a small amount of AcOH added as a catalyst. Each product from these attempts was distinct in visual appearance – Mn3N2O appeared as a light brown solid, Fe^{3+}3N2O displayed a fluffy light yellow material, and Fe^{2+}3N2O was a black and clumped solid.

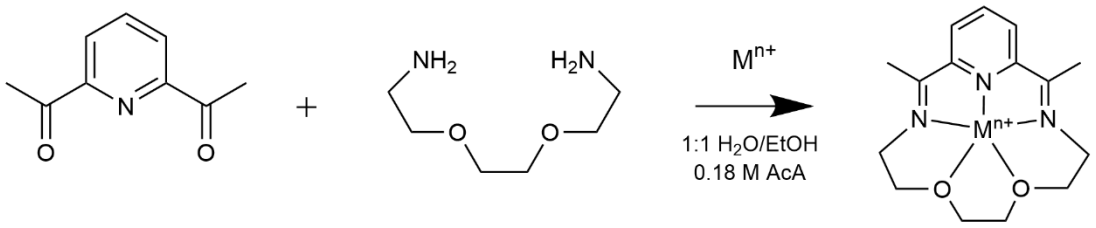

Scheme 8: General reaction scheme for initial series of M3N2O type macrocycle complexes.

Cyclic voltammetry was performed on these three species using the same cell conditions - 15 mL of acetonitrile with 0.1 M TBAHFP, a silver wire as the reference electrode (externally referenced to ferrocene/ferrocenium couple), a glassy carbon working electrode, and a platinum wire as the counter electrode. These were assessed

individually – however, an interesting pattern became quickly apparent. With all three samples, the CV was nearly identical, displaying only slight potential shifts from one another, likely attributable to the variability of using ferrocene as the reference along with the silver wire (Figure 22). The first reduction peak is aligned approximately to that of -2.15 V (*vs.* Fc/Fc^{+}). A second weaker reduction was seen at approximately -2.45 V. The next reduction peak is approx. at -2.85 V, forming on its return oxidation an unusual narrow gap at -2.75 V, not previously observed in any testing. A CV was then carried out with only 2,6-diacetylpyridine present with the normal electrochemical cell setup. This voltammogram was essentially the same as those of the purported 3N2O complexes (Figure 22). With the near exact similarity between the three samples and that of 2,6-diacetylpyridine, it is proposed that the macrocyclic formation was incomplete perhaps due to the use of water in this synthesis procedure. This is supported by subsequent research that suggested that water may inhibit the formation of the macrocycle. In literature from an extensive collaboration of scientists that tested a great number of these macrocycles, they note specifically 'If the reaction is carried out in the presence of water, hydrolysis occurs to give an octahedral complex of the ring-opened ligand'.[58,59]

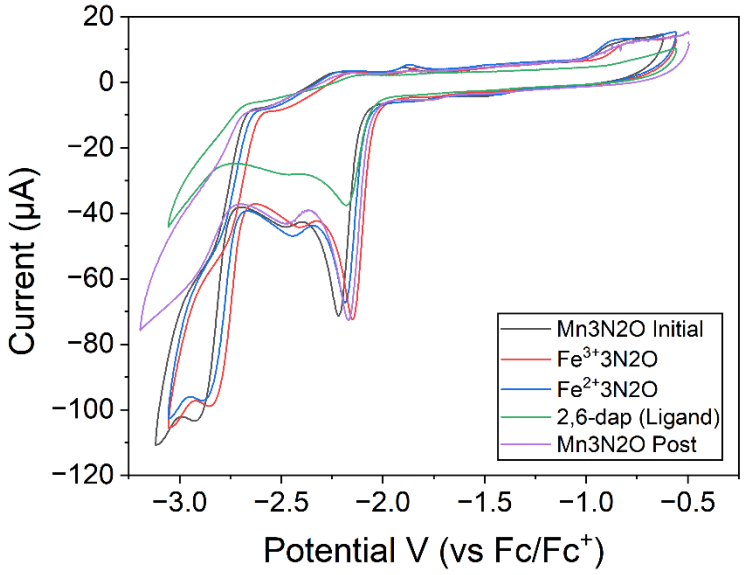

Figure 22: Cyclic voltammetry under cathodic potentials (*vs.* Fc/Fc^{+}) for attempts at Mn3N2O, Fe^{3+}3N2O, Fe^{2+}3N2O, 2,6-diacetylpyridine (2,6-dap) and Mn3N2O after stirring, N_2 purging.

3.3 – Alternative Preparation of Macrocyclic Complexes

After these results, further review of literature was conducted for an alternative synthesis procedure. One was found with a rather simple change – removal of water and using only ethanol, and removal of acetic acid addition.[60] A generalized reaction scheme is presented in Scheme 9. The presence of water may not be wholly responsible for the previous findings. However, the high level of difference in end product, most readily visually and electrochemically by cyclic voltammetry, appears to substantiate the change in procedure. Electrochemical characterization was conducted by cyclic voltammetry with the cell setup identical to the previous samples. Ferrocene correction was not performed

for Mn3N2O, Mn5N-2,2,2 and Mn5N-3,2,3 samples due to this being a cursory exploration as well as ferrocene presence obscuring oxidation responses above 0 V.

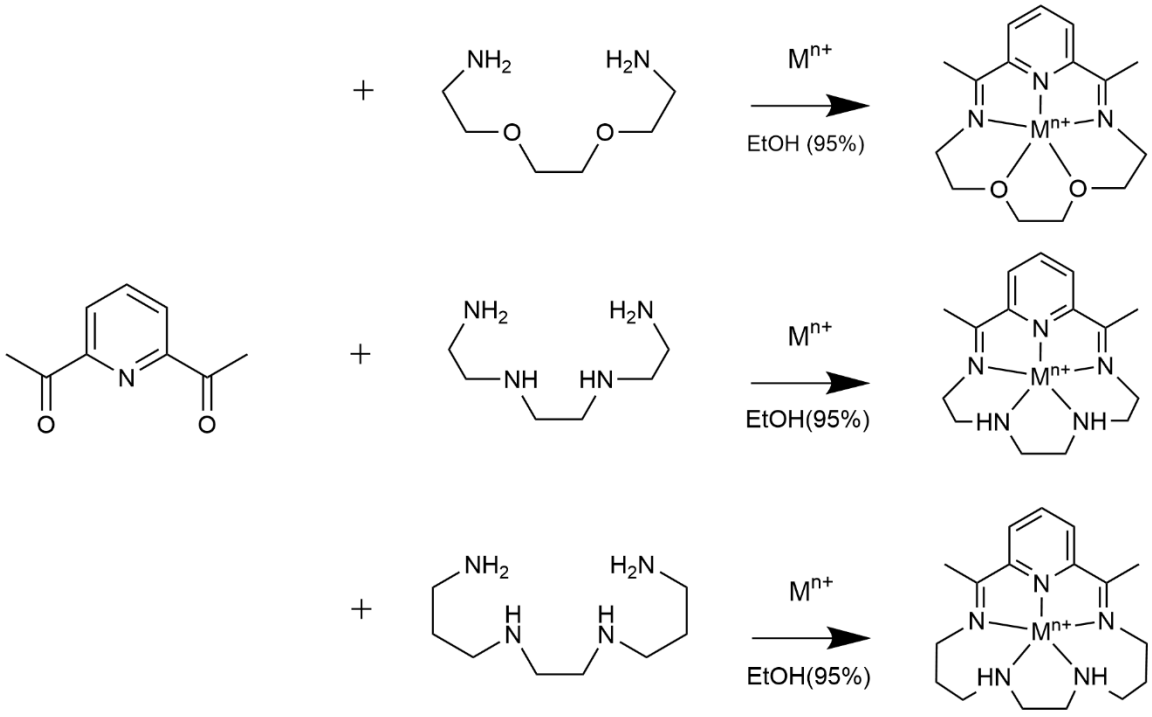

Scheme 9: Generalized reaction scheme for second series of M3N2O, M5N-3,2,3, and M5N-2,2,2 type macrocycle complexes.

3.3.1 – Mn3N2O Macrocycle Complex

The final product of Mn3N2O using the new procedure appeared as a bright orange powder contrasting to the previous Mn3N2O sample. Mn3N2O complex was characterized by FTIR and cyclic voltammogram measurements compared with previous section tests. While there are certain key FTIR characteristics noted in literature that may indicate a successful synthesis of the macrocyclic complex, such as an identical response

of the pyridine ring at 1590 cm^{-1}, and absence of a peak in the 3200-3300 cm^{-1} region, the complex formation is not confirmed by alternative characterization such as single crystal XRD, or ^{1}H NMR due to paramagnetism.[56]

Starting with Mn3N2O in 15 mL acetonitrile, 0.1 M TBAHFP as electrolyte – the oxidation side electrochemistry presents a clear reversible oxidation event at $E_{1/2}$ = 0.94 V (*vs.* Ag wire), with a current strength of 12 µA and 10 µA for the oxidation and reduction peaks here (Figure 23). A possible oxidation event is also observed in the 2.2 V region, appearing as an oxidation peak at ~2.25 V and a return reduction peak at ~2.15 V. These peaks are not well defined and overlap with the solvent window limits. In the cathodic region, the first reduction appeared as an irreversible reduction event, with the peak at -1.10 V (*vs.* Ag wire) and 19 µA (Figure 23). A smaller less-defined reduction peak is also observed at -1.25 V and 18 µA. A third broad reduction peak is observed at -1.78 V with 21 µA current. No return oxidation peaks are observed. With water addition, the first reduction peak gradually increases in current with each step of addition, maximizing with 5.6 M at 77 µA. The second reduction peak from 0.37 M onward is observable but significantly varies in potential with each addition. The first and second reduction peak maximizes from ~5.6 M to 9.3 M. The third reduction peak enhances significantly with low amounts of water (0.74 M, 39 µA), although this reduction event appears to diminish for water additions past this point, with 5.6 M and above eliminating observability entirely.

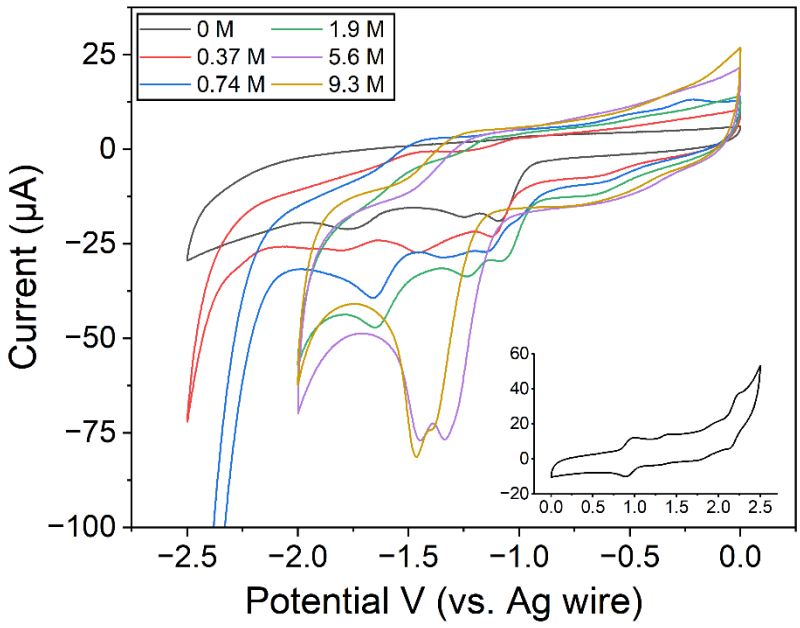

Figure 23: Cyclic Voltammetry under cathodic potentials (*vs.* Ag wire) of 1.0 mM complex Mn3N2O in 15 mL acetonitrile, 0.1 M TBAHFP with listed amounts of water addition. The inset graph is cyclic voltammetry under anodic potentials in acetonitrile without water present from 0 to 2.5 V (*vs.* Ag wire).

3.3.2 – Mn5N-2,2,2 Macrocycle Complex

Mn5N-2,2,2 synthesis was confirmed by single crystal XRD matched in the Cambridge database and FTIR. Examining Mn5N-2,2,2 under anodic potentials, the inset in Figure 24 shows a quasi-reversible couple was seen at an $E_{1/2}$ = 1.62 V (*vs.* Ag wire), and an irreversible reduction peak at 0.68 V. Under cathodic potentials, the only electrochemical response in acetonitrile was a broad irreversible reduction peak in the -1.5 to -1.7 V region (*vs.* Ag wire) (Figure 24). This reduction event appeared to change with the addition of water. With 1.1 M water present, two irreversible reduction peaks appear at approximately -1.32 V and -1.47 V. Expanding the potential window from 0 V

to 0.5 V for a sample with 2.6 M water (Figure 24, green and purple), it appeared the first reduction is linked to an oxidation event at -0.04 V. With this oxidation event overlayed, the first reduction peak is seen at -1.4 V as part of the entire reduction event. Interesting is the significant increase of current for this reduction, growing from 63 µA to 109 µA at -1.5 V with no other changes. Further additions of water enhance this peak to a maximum of 158 µA at 4.6 M, diminishing in current strength gradually with higher amounts. Additionally, a quasi-reversible couple develops at $E_{1/2}$ = -0.49 V that holds steady after 4.6 M is present. The potential window for reduction of water at the electrode is observed past -1.8 V with amounts of water higher than ~1.1 M.

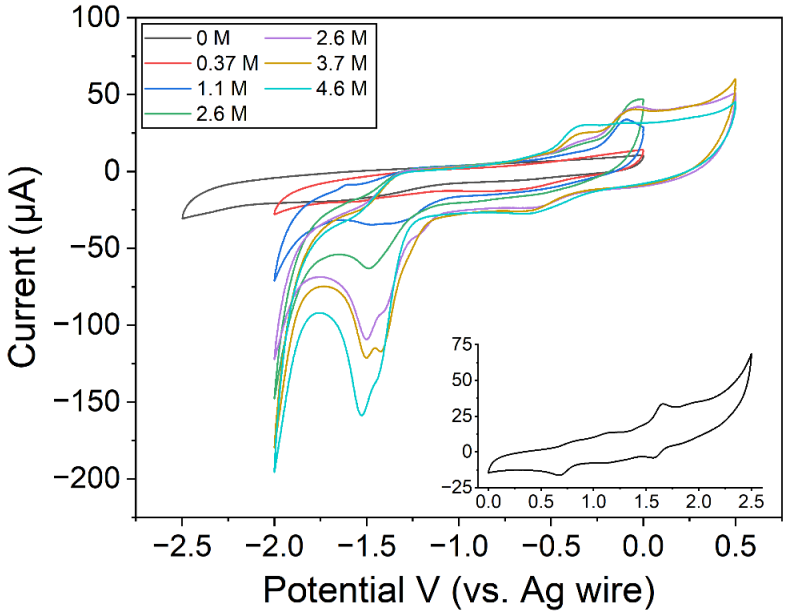

Figure 24: Cyclic voltammetry under cathodic potentials (*vs.* Ag wire) of 1.0 mM complex Mn5N-2,2,2 in 15 mL acetonitrile, 0.1 M TBAHFP with listed amounts of water addition. The inset graph is cyclic voltammetry under anodic potentials in acetonitrile from 0 to 2.5 V (*vs.* Ag wire).

The enhancement that is observed is likely to be attributable to the first reduction peak in the -1.5 V region, developing roughly in-line with the peak at 1.1 M and -1.47 V. This peak develops at the same approximate potential with further additions of water, with no major shifts observed. The current growth from ~20 µA to 158 µA does indicate a reasonable possibility for catalytic hydrogen production from water as a substrate, although clear visible indicators such as bubble formation on the working electrode were not present. Fouling or other homogeneous products were not observed on the working or counter electrode after testing.

3.3.3 – Mn5N-3,2,3 Macrocycle Complex

Mn5N-3,2,3 synthesis was confirmed by single crystal XRD. Exploring with cyclic voltammetry under anodic potentials, the inset in Figure 25 shows a single irreversible oxidation event at 1.44 V, with no other notable features. Under cathodic potentials, similar to Mn5N-2,2,2, a single broad irreversible reduction peak is observed, although appearing at a much lower potential of -1.28 V (*vs.* Ag wire) (Figure 25). With water addition, the peak at -1.28 V gradually enhances to a maximum of 51 µA at -1.35 V, with a clear oxidation peak at 0.18 V. However, additions of water past this point significantly changes the reduction curve, developing two new reduction peaks at -0.85 V and -1.86 V. Additionally, the oxidation peak that developed at 0.18 V was eliminated entirely. The maximum current of the two reduction peaks is 58 µA and 144 µA respectively.

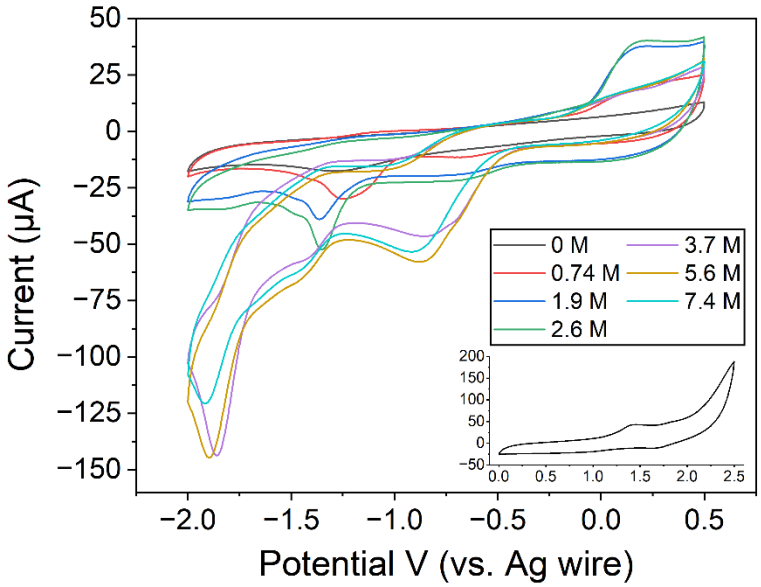

Figure 25: Cyclic voltammetry under cathodic potentials (*vs.* Ag wire) of 1.0 mM complex Mn5N-3,2,3 in acetonitrile with listed amounts of water addition. The inset graph is cyclic voltammetry under anodic potentials in acetonitrile from 0 to 2.5 V (*vs.* Ag wire).

While the maximum current strength of 144 μA at -1.86 V (*vs.* Ag wire) is notably high compared to 0 M, and thus perhaps a sign of effective electrolysis of water, it should be noted that the potential window for reducing water at the electrode has not been observed here up to -2.0 V. Instead, a reduction event is occurring at this potential of ~-1.8 V with the observation of a clear reduction peak. This correlates with the visual observation of fouling on the counter electrode as an orange coating. Furthermore, the peak strength at ~-1.8 V notably diminishes with continuous CV cycles, suggesting that the complex is being irreversibly consumed in some form. With this change only occurring with the presence of water, it suggests that water facilitates the deposition of Mn5N-3,2,3

on the electrode in some form, materially changing the complex. This was not observed with the similar complex Mn5N-2,2,2. Looking at the structural configuration in the crystal structure, Mn5N-3,2,3 is distorted, with the macrocyclic ligand bending at ~110° from the side and is accompanied by only one chloride. This configuration would lead to a higher susceptibility to substituting molecules such as chloride for water, and this decomposition possibly induced by electrolysis with water, although this was not explored in detail.

3.3.4 – Ni5N-3,2,3 Macrocycle Complex

The Ni5N-3,2,3 synthesis was conducted by two separate procedures, one by direct synthesis and another later by transmetalation with a prepared Ag template. Despite the complex being reported as not possible to directly synthesize, the complex was attempted to be made regardless. This led to a positive outcome where a discrete purple powder was made as a final product and was found to support the formation of a heterogeneous film under electrolysis. This product was established as not forming the intended macrocyclic complex, but an open-ended complex with 1,2-bis(3-aminopropylamino)ethane and $NiCl_2$. This product will be covered in detail in Chapter 4. The second procedure following the reported synthesis pathway in making Ni5N-3,2,3 involves the formation of the complex using Ag(I), then using transmetalation to substitute it with Ni(II).[61] A PhD candidate in our group, Somayeh Norouziyanlakvan, followed the initial procedural steps and successfully created the Ag precursor complex, with myself following up with the Ni complexation and further creation of Ag complex for

additional Ni5N-3,2,3 synthesis. Nitrite reduction to ammonia and/or hydroxylamine would later be tested as supplemental information in comparing to their previous incomplete Ni5N-3,2,3 macrocyclic complex. Ag5N-3,2,3 synthesis would be confirmed by single crystal XRD performed by Somayeh and ^{1}H NMR in CD_3CN. Ni5N-3,2,3 synthesis was confirmed by single crystal XRD.

Exploring cyclic voltammetry of Ni5N-3,2,3 under cathodic potentials, two reversible reductions events were observed with $E_{1/2}$ = -1.23 V and -1.85 V (*vs.* Fc/Fc^{+}) (Figure 26). The inset in Figure 26 shows under anodic potential a single irreversible oxidation event observed at 1.43 V (*vs.* Ag wire). Additions of water indicate an increase of current from the second reduction peak, moving from 27 µA to 51 µA with 0.37 M water present (Figure 27). The first reduction event increase in current as well from 11 µA to 28 µA, although the oxidation peak loses form and could be considered quasi-reversible. From 3.7 M to 5.6 M, a clear peak develops at -1.36 V, and maximizes at 7.4 M, -1.30 V at 76 µA. The potential continues to shift slightly right with further water additions, decreasing in current strength at 11 M and -1.26 V. It is not known whether this peak develops directly from the first reduction peak at 0 M, ~-1.4 V. A CV scan isolating from -0.31 to -1.51 V (*vs.* Fc/Fc^{+}) at 9.3 M does indicate that the reduction event is quasi-reversible, with E_{red} = -1.27 V, E_{ox} = -1.17 V, $E_{1/2}$ = -1.22 V. With the quasi-reversibility here, the high amount of potential shift it experiences (including accounting for ferrocene), and the disappearance/reemergence of the peak at 3.7 M water - it is suggested that the reduction event is not wholly transformed via decomposition. However, it does appear to be structurally affected beyond simple enhancement of the original first reduction peak.

With the second reduction event, information can be clearly gathered up to 5.6 M. At 5.6 M water, the reduction peak is approx. at -1.72 V with the return oxidation broadly around -1.60 V. Further additions gradually reduce the presence of the second reduction event, likely due to eclipsing of water reduction by the working electrode and the limits of the potential window.

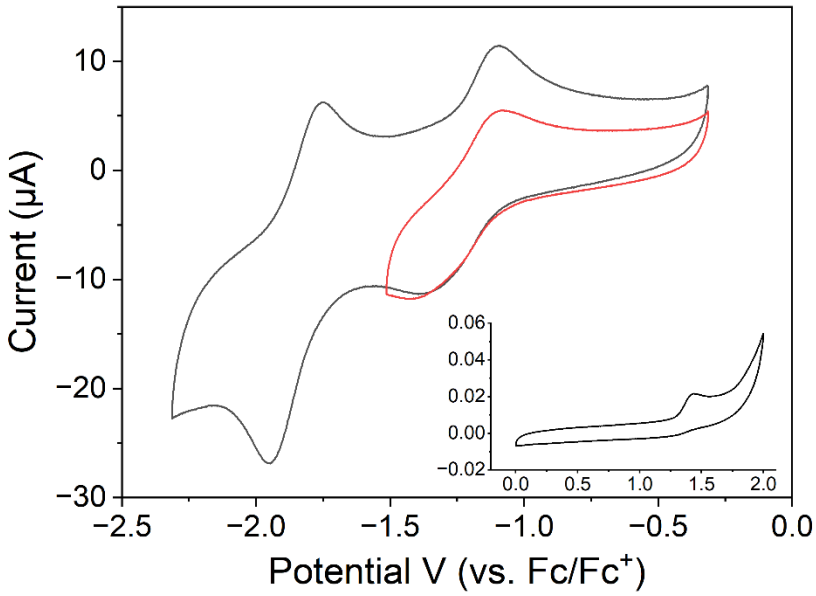

Figure 26: Cyclic voltammetry under cathodic potentials (*vs.* Fc/Fc^+) of 1.0 mM complex Ni5N-3,2,3 in 15 mL acetonitrile and 0.1 M TBAHFP as electrolyte, from -0.31 V to -2.31 V (black), and -0.31 V to -1.51 V (red). Inset graph is cyclic voltammetry under anodic potentials in acetonitrile from 0 to 2.0 V (*vs.* Ag wire).

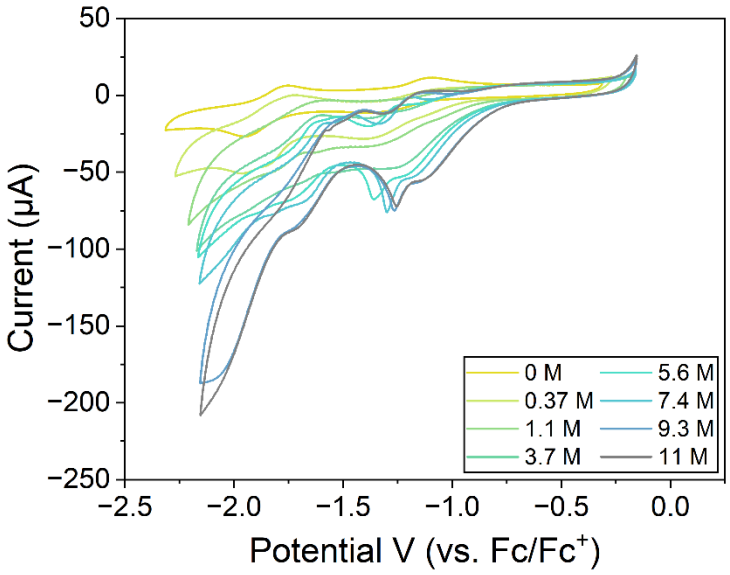

Figure 27: Cyclic voltammetry under cathodic potentials (*vs.* Fc/Fc^+) of 1.0 mM complex Ni5N-3,2,3 in acetonitrile and 0.1 M TBAHFP as electrolyte with listed amounts of water addition.

The Ni5N-3,2,3 complex was also tested for its potential for nitrite reduction using $NaNO_2$ in aqueous solution. The cell setup consists of 0.1 M KCl aqueous solution, with KCl as the electrolyte, 0.1 M 3-morpholinopropanesulfonic acid (MOPS) as buffer, adding 1.0 mM of Ni5N-3,2,3, and additions of $NaNO_2$ up to 100 mM. The electrodes used were the standard GC electrode for working electrode, 3.0 M KCl with Ag/AgCl reference electrode, and platinum counter electrode wire. A minor error was made in using the 0.1 MOPS as a free acid rather than the prepared pH 7 buffer version, but this did allow insights into the reactivity of the MOPS acid form.

The initial solution setup of 0.1 M KCl aqueous solution and 0.1 M MOPS was held as it needed establishment if MOPS possessed any innate reactivity on its own in solution. Looking at Figure 28, the addition of 0.1 M MOPS causing the cathodic shift of the onset

to ~-1.2 V (*vs.* Ag/AgCl) occurs significantly earlier compared to background of 0.1 M KCl alone. The overall width of current between reduction and return oxidation passes is pronounced in the reduction area past -1.20 V, but not regarded as impactful to testing. With 1.0 mM Ni5N-3,2,3 added, the initial CV shifted significantly lower in potential, with an irreversible reduction event onsetting at ~-0.8 V and increasing in current, peaking at -1.40 V at 865 µA. At this same current, the 0 mM solution required -1.88 V to induce this current rate. It should be noted that upon addition of the catalyst and application of current by CV, continuous gas bubbles were induced at the electrode, disrupting the scans. After 20 min, the production of bubbles significantly diminished, and repeatable CV scans were permitted with no detected disruption to the current.

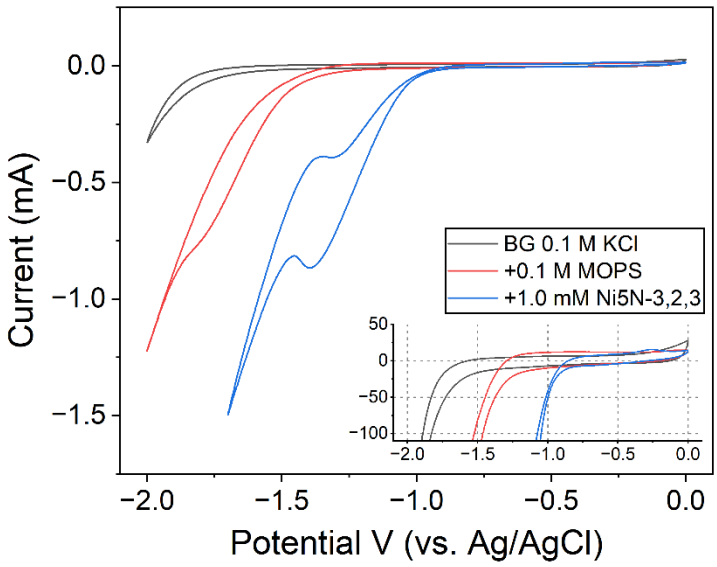

Figure 28: Cyclic voltammetry under cathodic potentials (*vs.* Ag/AgCl) with and without 1.0 mM complex Ni5N-3,2,3 in 0.1 M KCl aqueous solution, 0.1 M MOPS. Background measurement with 0.1 KCl alone (black), adding 0.1 M MOPS (red), and adding 1.0 mM Ni5N-3,2,3 (blue). Inset graph is a zoomed view of the main graph.

With $NaNO_2$ addition starting with 10 mM, the peak initially observed at -1.40 V at 865 µA shifted to ~-1.3 V and 690 µA (Figure 29). Notably, the onset for this reduction has significantly shifted to a lower potential of ~-0.5 V from the initial -0.82 V. 20 mM $NaNO_2$ generally completes this significant shift, with the peak moving to the ~-1.0 V region and 425 µA, with 30 mM paralleling this finding. Further additions up to 80 mM gradually maximizes the increase of current at -0.94 V and 490 µA. Overall, although there is an interesting cathodic shift of the reduction to significantly lower potentials, the lack of enhancement of current with higher amounts of $NaNO_2$, as well as the lack of a defined peak led to the conclusion that there was no appreciable catalytic reduction of NO_2^- under these conditions.

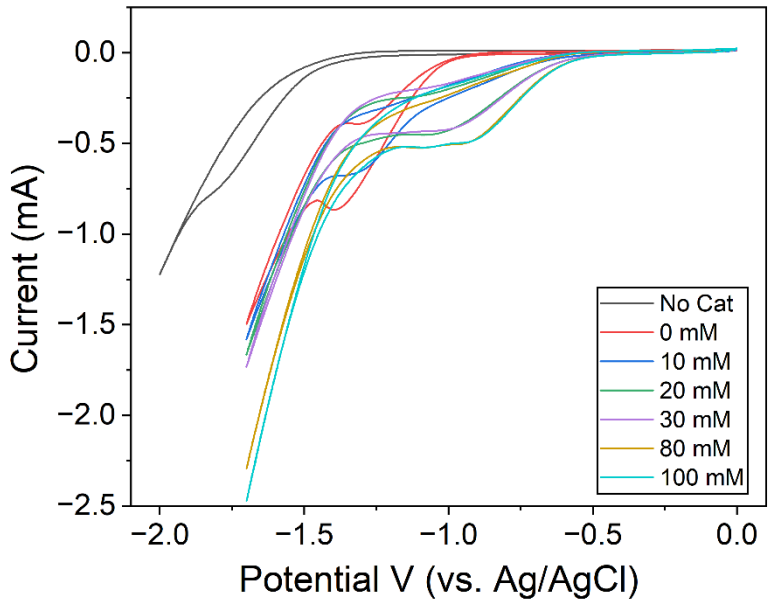

Figure 29: Cyclic Voltammetry under cathodic potentials (*vs.* Ag/AgCl) of 1.0 mM complex Ni5N-3,2,3 in 0.1 M KCl aqueous solution, 0.1 M MOPS with listed amounts of $NaNO_2$ addition.

In conclusion, this chapter covers the brief exploration of a number of macrocyclic complexes. The primary goal here was the creation and characterization of the complexes, which led to three new crystal structures not present in the Cambridge database. Furthermore, these macrocyclic complexes were investigated for their general electrochemical functionality in acetonitrile and for possible catalytic enhancement with the addition of water as a substrate. Mn3N2O, Mn5N-2,2,2 and Ni5N-3,2,3 showed interesting enhancements in the -1.0-1.5 V ranges, potentially indicative of some degree of HER process occurring and worthy of further investigation. However, with the remarkable discoveries made in Chapter 4, and the general detriments of organic solvent to that of aqueous, this was left as possible future work to explore.

3.4 – Crystal Structure

3.4.1 – Fe5N-2,2,2, Mn5N-2,2,2, and Ni5N-3,2,3

Fe5N-2,2,2 is arranged in a pentagonal bipyramidal configuration with the ligand forming a highly planar ring around the Fe(III) atom, with two chloride atoms on opposing sides (Figure 30). A perchlorate atom is observed tangentially attached to the main complex. Bond angle for Cl(1)-Fe(1)-N(1) is noted at 89.74 degrees, correlating to the observed planar ring structure. The sum of bond angles for nitrogen atoms coordinated around the iron atom is 360.44 degrees, noting higher or lower deviations from 360 degrees as distortions of a perfect ring structure. With Cl(1)-Fe(1)-Cl(2), the bond angle is

179.38, indicating minimum distortion from internal ring configuration or external perchlorate anion influence.

The bond distance for the chloride atoms are 2.3192 Å for Fe(1)-Cl(1) and 2.3462 Å for Fe(1)-Cl(2). These distances are quite similar to the base reagent $FeCl_3 \cdot 6H_2O$ for the complex, reported at 2.296 Å for Fe-Cl, suggesting a slightly weaker bond due to the additional length.[62] The Fe-N bonds are relatively closer, with the N(1/3/4/5) connections having distances ranging from 2.22-2.25 Å. In contrast, the Fe(1)-N(2) bond on the pyridine ring is markedly shorter at 2.175 Å, likely due to the higher electron density present along the conjugated pyridine ring. Additional crystal sample data and selected bond lengths and bond angles are provided in Table 2 and 3.

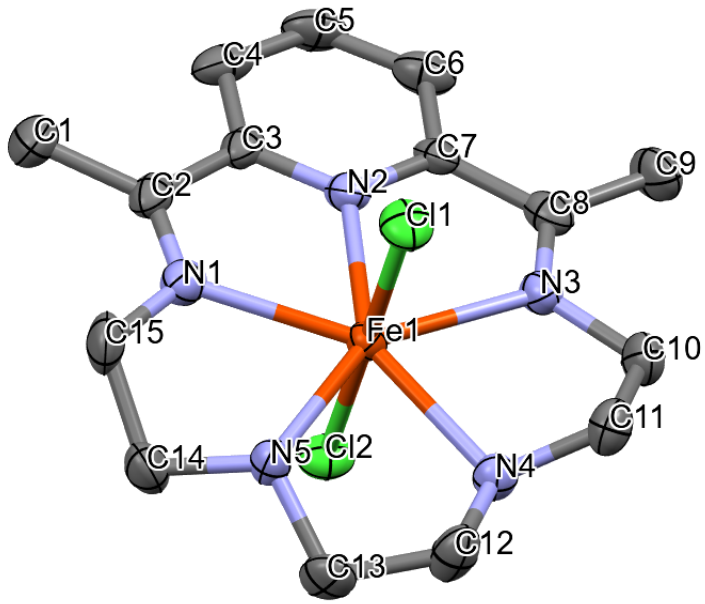

Figure 30: Structural representation of Fe5N-2,2,2 (Dichloro-(2,13-dimethyl-3,6,9,12,18-pentaazabicyclo[12.3.1]octadeca-1(18),2,12,14,16-pentaene-N^3,N^6,N^9,N^{12},N^{18})-iron(III) perchlorate), obtained from single crystal X-ray analysis. One perchlorate molecule and hydrogen atoms have been excluded for clarity.

Mn5N-3,2,3 is arranged in a distorted octahedral configuration, with the ligand forming a complete macrocycle around the Mn(II) atom, and a single chloride atom coordinated to the manganese atom on one side (Figure 31). One perchlorate and one water molecule are tangentially adjacent to the complex. The ligand ring is moderately distorted to one side opposite to the chloride. Bond angle for Cl(1)-Mn(1)-N(1) of the pyridine ring is 133.74 degrees, highlighting the overall flexing of the pyridine counter to the chloride, likely due to electron density repulsion. In contrast, Cl(1)-Mn(1)-N(2) bond angle is modest at 93.84 degrees, Cl(1)-Mn(1)-N(3) at 108.65 degrees, signifying the primary repulsion at the pyridine ring, with lesser flexing at the opposite side of the macrocycle ring. The sum of bond angles for nitrogen atoms coordinated around the iron atom is 363.73 degrees, paralleling to the overall ring flexing.

The bond distance for the chloride atoms are 2.4005(6) Å for Mn(1)-Cl(1). Compared to the base reagent $MnCl_2 \cdot 4H_2O$ for synthesis of the complex, reported at 2.549 Å for Mn-Cl, this reduced distance suggesting a slightly stronger bond with this length.[63] The Mn-N bonds are relatively closer, with the N2/4/5 connections having bond lengths close to 2.33 Å, with Mn(1)-N(3) notable longer at 2.3642 Å. The Mn(1)-N(1) bond on the pyridine ring is similar to Fe5N-2,2,2, in that it is shorter at 2.2297 Å, likely due to the higher electron density present along the conjugated pyridine ring. Overall, the nitrogen atom bond distance is increased to the metal center as compared to the previous Fe5N-2,2,2 complex. Additional crystal sample data and selected bond lengths and bond angles are provided in Table 2 and 4.

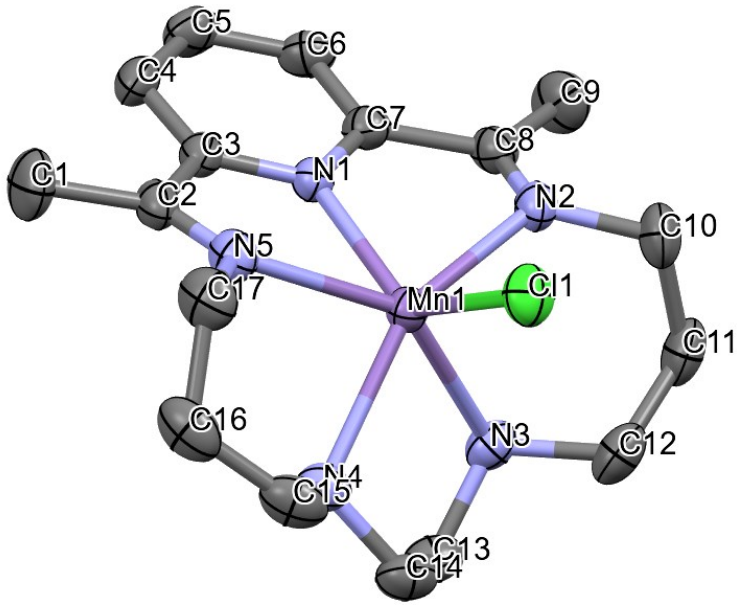

Figure 31: Structural representation of Mn5N-3,2,3 (Chloro-(2,15-dimethyl-3,7,10,14,20-pentaazabicyclo[14.3.1]eicosa-1(20),2,14,16,18-pentaene-N^3,N^7,N^{10},N^{14},N^{20})-aquamaganese(II) perchlorate), obtained from single crystal X-ray analysis. One perchlorate molecule, one water molecule, and hydrogen atoms have been excluded for clarity.

Ni5N-3,2,3 is arranged in an octahedral configuration with the ligand forming a complete macrocyclic, however distorting so that four nitrogen atoms (including the pyridine) are planar with each other, while one nitrogen atom of the macrocycle is approximately opposite to that of the coordinating methanol molecule with the central Ni(II) atom (Figure 32). Two perchlorate anions are tangentially adjacent to the complex, with one perchlorate hydrogen bonding with the methanol O-H group. Bond angle for N(4)-Ni(1)-O(1) is at 90.33 degrees, with the N(2/3/5) bonds to O(1) ranging from 86-92 degrees. The N(1)-Ni(1)-O(1) bond angle is 166.44 degrees, likely restricted in angle by the adjoining macrocycle ligand structure. Total bond angle around the N(2/3/4/5) planar

coordination is 359.98 degrees, highlighting a strong conformation to the octahedral configuration despite the clear non-planar nature to the entire macrocyclic ligand.

Bond lengths are overall shorter than the previous listed complexes, with Ni(1)-N(1/2/3/5) bond lengths approximately equal, ranging from 2.07 Å to 2.13 Å, with the N(1) atom opposite of methanol having the greatest length (2.132 Å). Ni(1)-N(4) from pyridine is notably shorter at 1.992 Å, likely due to the higher electron density the conjugated pyridine ring can provide. The Ni(1)-O(1) parallels the other bond lengths at 2.113 Å, indicating a highly balanced bond configuration. Additional crystal sample data and selected bond lengths and bond angles are provided in Table 2 and 5.

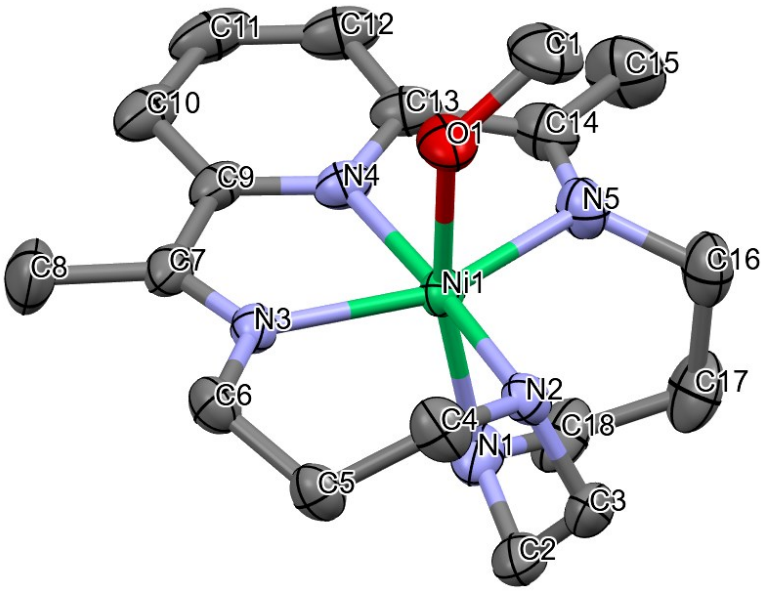

Figure 32: Structural representation of Ni5N-3,2,3 (Methanol-(2,15-dimethyl-3,7,10,14,20-pentaazabicyclo[14.3.1]eicosa-1(20),2,14,16,18-pentaene-N^3,N^7,N^{10},N^{14},N^{20})-nickel(II) diperchlorate), obtained from single crystal X-ray analysis. Two perchlorate molecules and hydrogen atoms from the main macrocyclic complex have been excluded for clarity.

3.4.2 – Crystal Sample Data and Select Bond Angles, Bond Lengths

Table 2: Crystal sample data for Fe5N-2,2,2, Mn5N-3,2,3 and Ni5N-3,2,3.

	Fe5N-2,2,2	Mn5N-3,2,3	Ni5N-3,2,3
Empirical Formula	$C_{15}H_{21}Cl_2N_5O_4Fe$	$C_{17}H_{29}Cl_2N_5O_5Mn$	$C_{18}H_{31}Cl_2N_5O_9Ni$
Formula weight ($g \cdot mol^{-1}$)	497.57	509.29	591.09
Crystal System	monoclinic	triclinic	monoclinic
Space group	P $2_1/c$	P -1	P $2_1/c$
a (Å)	7.9559(2)	8.0365(3)	9.9524(5)
b (Å)	22.2128(5)	10.9805(5)	16.5098(6)
c (Å)	11.4670(4)	13.8218(6)	15.1274(7)
α (°)	90	67.127(1)	90
β (°)	90.159(2)	84.234(1)	90.825(1)
γ (°)	90	81.266(1)	90
V (Å^3)	2026.47(10)	1109.61(8)	2485.36(19)
Z	4	2	4
T (K)	200(2)	200(2)	200(2)
ρ_{calcd} ($g \cdot cm^{-3}$)	1.613	1.524	1.580
μ (mm^{-1})	1.172	0.874	1.053
$2\vartheta_{max}$ (°)	52.778	53.066	58.260
Parameters	255	331	319
Total Reflections	4093	4584	6686
R, wR^2 [$I_o \geq 2_\sigma(I_o)$]	0.0689, 0.1865	0.0288, 0.0771	0.0474, 0.1261
S (Goodness of fit)	1.060	1.032	1.058

Table 3: Selected bond lengths and bond angles for Fe5N-2,2,2 crystal sample data.

Selected Bond Distances for Fe5N-2,2,2	
Atom-Atom	Length (Å)
Fe(1)-N(1)	2.221(5)
Fe(1)-N(2)	2.175(5)
Fe(1)-N(3)	2.248(5)
Fe(1)-N(4)	2.227(5)
Fe(1)-N(5)	2.239(5)
Ni(1)-Cl(1)	2.3192(17)
Ni(1)-Cl(2)	2.3462(17)

Selected Bond Angles for Fe5N-2,2,2	
Atom-Atom-Atom	Angle (˚)
N(1)-Fe(1)-N(2)	71.12(17)
N(1)-Fe(1)-N(3)	141.69(17)
N(1)-Fe(1)-N(4)	147.46(18)
N(1)-Fe(1)-N(5)	72.79(17)
N(1)-Fe(1)-Cl(1)	89.74(13)
Cl(2)-Ni(1)-Cl(1)	179.38(7)

Table 4: Selected bond lengths and bond angles for Mn5N-3,2,3 crystal sample data.

Selected Bond Distances for Mn5N-3,2,3	
Atom-Atom	Length (Å)
Mn(1)-N(1)	2.2297(16)
Mn(1)-N(2)	2.3321(19)
Mn(1)-N(3)	2.3642(16)
Mn(1)-N(4)	2.3334(19)
Mn(1)-N(5)	2.3263(15)
Mn(1)-Cl(1)	2.4005(6)

Selected Bond Angles for Mn5N-3,2,3	
Atom-Atom-Atom	Angle (˚)
N(1)-Mn(1)-N(2)	69.13(6)
N(1)-Mn(1)-N(3)	106.75(6)
N(1)-Mn(1)-N(4)	121.86(6)
N(1)-Mn(1)-N(5)	69.37(6)
N(1)-Mn(1)-Cl(1)	133.74(4)
N(2)-Mn(1)-Cl(1)	93.84(4)

Table 5: Selected bond lengths and bond angles for Ni5N-3,2,3 crystal sample data.

Selected Bond Distances for Ni5N-3,2,3	
Atom-Atom	Length (Å)
Ni(1)-N(1)	2.132(2)
Ni(1)-N(2)	2.074(2)
Ni(1)-N(3)	2.107(2)
Ni(1)-N(4)	1.992(2)
Ni(1)-N(5)	2.098(2)
Ni(1)-O(1)	2.113(2)

Selected Bond Angles for Ni5N-3,2,3	
Atom-Atom-Atom	Angle (˚)
N(1)-Ni(1)-N(2)	83.34(10)
N(1)-Ni(1)-N(3)	100.07(10)
N(1)-Ni(1)-N(4)	101.46(10)
N(1)-Ni(1)-N(5)	84.34(11)
N(1)-Ni(1)-O(1)	166.44(10)
N(2)-Ni(1)-O(1)	85.60(10)
N(4)-Ni(1)-O(1)	90.33(10)

3.5 – Experimental Details

3.5.1 – General Methods

Commercial reagents were purchased from Sigma-Aldrich, Alfa-Aesar and TCI America and were used without further purification. Synthesis reactions that were performed in an inert atmosphere were conducted under nitrogen. NMR spectra measurements were carried out on a Bruker Avance II 400 instrument at room temperature. Electrochemical measurements were performed on a Princeton Applied

Research VersaSTAT 3 Potentiostat. Single crystal XRD measurements were performed by the X-ray Core Facility staff at the University of Ottawa.

3.5.2 – Electrochemical Cell Setup

Electrochemical characterization of the complex was performed in a 40 mL three-neck flask with a glassy carbon working electrode for CV characterization, a silver wire as the reference electrode, and a platinum wire for the counter electrode. The regular cell standard is 15 mL of acetonitrile, 0.1 M of TBAHFP, and 1 mM of examined sample while purged under a nitrogen atmosphere. When water was the solvent, an Ag/AgCl reference electrode (3 M KCl) was used in place of the silver wire.

3.5.3 – Initial Synthesis Attempts for Mn3N2O, Fe^{3+}3N2O, Fe^{2+}3N2O

Synthesis of Mn3N2O Complex: $MnCl_2 \cdot 4H_2O$ (0.247 g, 1.25 mmol), 2,6-diacetylpyridine (0.204 g, 1.25 mmol), and 1,8-diamino-3,6-dioxaoctane (0.185 g, 0.96 g/mL, 1.25 mmol), and were measured in a 1:1:1 molar ratio. These reagents were dissolved in 6 mL ethanol with an additional 6 mL DI water added within a 50 mL round bottom flask. After all reagents were dissolved resulting in a light brown solution, 0.125 mL (0.002 mol) of glacial acetic acid was added under stirring. The solution turned black upon impact of the acetic acid. The reaction flask was kept under reflux under moderate stirring for a period of 18 h, after which the flask was removed from heat, appearing as a light brown solution. After cooling, sodium perchlorate (0.168 g, 1.38 mol) was added in

a 1.1 molar ratio and stirred for 30 min. Pressure was reduced to remove ethanol from the mixture, which appeared to leave white/brown crystalline residue on the sides. This was filtered and washed with cold water, resulting in a light brown clumping material, left to dry overnight. Product mass was 0.175 g. No yield is calculated as the initial synthesis attempts were shown to be unsuccessful.

Synthesis of Fe^{3+}3N2O Complex: $FeCl_3 \cdot 6H_2O$ (0.338 g, 1.25 mmol), 2,6-diacetylpyridine (0.204 g, 1.25 mmol), and 1,8-diamino-3,6-dioxaoctane (0.185 g, 0.96 g/mL, 1.25 mmol), were measured in a 1:1:1 molar ratio. These reagents were dissolved in 6 mL ethanol with an additional 6 mL DI water added within a 50 mL round bottom flask. After all reagents were dissolved resulting in a light orange solution, 0.125 mL (0.002 mol) of glacial acetic acid was added under stirring. An orange floating precipitate appeared and collated at the bottom of the flask. The reaction flask was kept under reflux under moderate stirring for a period of 18 h, after which the flask was removed from heat, appearing as an opaque orange solution with brown chunks of matter. After cooling, the solution changed to opaque yellow, and sodium perchlorate (0.168 g, 1.38 mol) was added in a 1.1 molar ratio and stirred for 30 min. Pressure was reduced to remove ethanol from the mixture, with it filtered and washed with cold water. This was left to dry overnight, resulting in a light-yellow fluffy product. Product mass was 0.043 g. No yield is calculated as the initial synthesis attempts were shown to be unsuccessful.

Synthesis of Fe^{2+}3N2O Complex: $FeCl_2$ (0.158 g, 1.25 mmol), 2,6-diacetylpyridine (0.204 g, 1.25 mmol), and 1,8-diamino-3,6-dioxaoctane (0.185 g, 0.96 g/mL, 1.25 mmol), were measured in a 1:1:1 molar ratio. These reagents were dissolved in 6 mL ethanol with

an additional 6 mL DI water added within a 50 mL round bottom flask. After all reagents were placed and mixed into solution, the solution appeared as opaque dark blue, with white-blue crystalline material collecting on the sides. After, 0.125 mL (0.002 mol) of glacial acetic acid was added under stirring. The solution turned black with an orange tinge. The reaction flask was kept under reflux under moderate stirring for a period of 18 h, after which the flask was removed from heat, appearing as an opaque dark blue solution. Sodium perchlorate (0.168 g, 1.375 mol) was added in a 1.1 molar ratio and stirred for 30 min. Pressure was reduced to remove ethanol from the mixture, with it filtered and washed with cold water. This was left to dry overnight, resulting in a black chunky, magnetic material. Product mass was 0.133 g. No yield is calculated as the initial synthesis attempts were shown to be unsuccessful.

3.5.4 – Synthesis of Mn5N-2,2,2, Fe5N-2,2,2, Mn5N-3,2,3, Ag5N-3,2,3, Ni5N-3,2,3

Synthesis of the Mn5N-2,2,2 complex: $MnCl_2 \cdot 4H_2O$ (0.247 g, 1.25 mmol), 2,6-diacetylpyridine (0.204 g, 1.25 mmol), and triethylenetetramine (0.188 g, 1.25 mmol), were measured in a 1:1:1 molar ratio. Each reagent was pre-dissolved in ~5 mL 95% ethanol, with holding vials washed with ~1 mL ethanol to collect remnants, to be combined in a 50 mL round bottom flask. The initial solution colour was dark orange, and the reaction flask was refluxed under moderate stirring for a period of 2 h, after which the flask was removed from heat. After cooling, sodium perchlorate (0.168 g, 1.38 mol)

was added in a 1.1 excess molar ratio and stirred for 30 min. An orange precipitate presented which was filtered and washed with ethanol through a coarse silica frit. This was left to dry overnight, with the dry powder mass as 0.462 g and a yield of 74%. Crystals of Mn5N-2,2,2 suitable for SC-XRD were acquired by slow diffusion of acetonitrile with diethyl ether.

Synthesis of the Fe5N-2,2,2 complex: $FeCl_3 \cdot 6H_2O$ (0.3379 g, 1.25 mmol), 2,6-diacetylpyridine (0.204 g, 1.25 mmol), and triethylenetetramine (0.188 g, 1.25 mmol), were measured in a 1:1:1 molar ratio. Each reagent was pre-dissolved in ~5 mL 95% ethanol, with holding vials washed with ~1 mL ethanol to collect remnants, to be combined in a 50 mL round bottom flask. The initial solution colour was orange brown, with the reaction flask refluxed under moderate stirring for a period of 2 h, after which the flask was removed from heat. After cooling, sodium perchlorate (0.168 g, 1.38 mol) was added in a 1.1 molar ratio and stirred for 30 min. The solution was passed and washed with ethanol through a paper filter and left to dry overnight. The final product was a light brown powder, with a dry product mass of 0.560 g and a yield of 90%. Crystals of Fe5N-2,2,2 suitable for SC-XRD were acquired by slow diffusion of acetonitrile with diethyl ether.

Synthesis of the Mn5N-3,2,3 complex: $MnCl_2 \cdot 4H_2O$ (0.247 g, 1.25 mmol), 2,6-diacetylpyridine (0.204 g, 1.25 mmol), and 1,2-bis(3-aminopropylamino)ethane (0.218 g, 0.952 g/mL, 1.25 mmol) were measured in a 1:1:1 molar ratio. Each reagent was pre-dissolved in ~5 mL 95% ethanol, with holding vials washed with ~1 mL ethanol to collect remnants to a total of 40 mL ethanol, combined in a 50 mL round bottom flask. These

were added step-wise by the order above to the flask with the initial solution colour being orange, no change with 2,6-diacetylpyridine addition, and a strong colour change to orange with addition of 1,2-bis(3-aminopropylamino)ethane. The reaction flask was refluxed under moderate stirring for a period of 2 h, after which the flask was removed from heat. After cooling, sodium perchlorate (0.168 g, 1.38 mol) was added in a 1.1 molar ratio and stirred for 30 min. After leaving to sit overnight, the sample crystallized out of solution as large orange crystals. These crystals were collected and filtered out of solution, with the dry crystal mass resulting as 0.341 g, with a yield of 54%. Crystals were characterized by SC-XRD.

Synthesis of the Ag5N-3,2,3 complex: $AgClO_4 \cdot H_2O$ (0.192 g, 0.854 mmol), 2,6-diacetylpyridine (0.140 g, 0.856 mmol), and 1,2-bis(3-aminopropylamino)ethane (0.140 g, 0.952 g/mL, 0.86 mmol) were measured in an approximate 1:1:1 molar ratio. Each reagent was pre-dissolved in ~5 mL methanol (99.8% assay), with holding vials washed with ~1 mL methanol to collect remnants, to be combined in a 50 mL round bottom flask. These were added step-wise by the order above to the flask with the initial solution colour being clear, changed to cloudy white with 2,6-diacetylpyridine addition, and a colour change to yellow with addition of 1,2-bis(3-aminopropylamino)ethane. The reaction flask was refluxed under moderate stirring overnight (~16 h), after which the flask was removed from heat. The flask held large quantities of olive green precipitate, with the yellow solution decanted into a new flask. The solvent was removed by rotary evaporation, with a yellow precipitate remaining in the flask. The precipitate was lightly washed with methanol and placed under vacuum overnight. Final product was a flaky

yellow precipitate with a dry product mass of 0.074 g and a yield of 13%. Product was confirmed via ^{1}H NMR in CD_3CN to crystallized samples suitable for SC-XRD.

Synthesis of the Ni5N-3,2,3 complex: $NiClO_4 \cdot 6H_2O$ (0.027 g, 0.073 mmol) and Ag5N-3,2,3 (0.051 g, 0.079 mmol) was measured in an approximate 1:1 molar ratio. Each reagent was pre-dissolved in ~5 mL methanol (99.8% assay), with holding vials washed with ~1 mL methanol to collect remnants, with a total of 15 mL methanol present in a 50 mL round bottom flask. The reaction flask was refluxed under moderate stirring for 2 h, after which the flask was removed from heat. Ag5N-3,2,3 required heating to dissolve fully. The initial solution colour was yellow, rapidly turning brown (~10 min) after heat was applied. Brown precipitate was observed after removed from heat, and the remaining methanol was left to evaporate. The precipitate washed with small amounts of ethanol and placed under vacuum overnight. The final product was a brown powder with a dry mass of 0.042 g and yield of 96%. Crystals of Ni5N-3,2,3 suitable for SC-XRD were acquired by slow diffusion of methanol with diethyl ether.

3.5.5 – FTIR

FTIR characterization was performed on samples Mn3N2O, Mn5N-2,2,2, and Fe5N-2,2,2. Notable features for the macrocyclic complexes in literature are mentioned are the imine linkage at 1650 cm^{-1}, the pyridine ring for 1590 cm^{-1}, and absence of residual carbonyl groups (as part of 2,6-diacetylpyridine) with a lack of absorption at 1700 cm^{-1}.[56] In particular for complexes with ether linkages (e.g. Mn3N2O), no absorption detected for the 3200-3300 cm^{-1} region.

First comparing Mn3N2O, notable in the 4000 to 1800 cm^{-1} region are two, clear peaks at 2884 and 2927 cm^{-1} (m, C-H) and one peak at 3494 cm^{-1} (m, N-H) (Figure 33). There is mild absorption in the 3200-3300 cm^{-1} region, but no defined peak significantly deviating from the baseline rate. From 1800 to 600 cm^{-1}, responses are approximately similar, with choice peaks highlighted as 1650 cm^{-1} (m, N-H), 1580 cm^{-1} (m, C=C), 1460 cm^{-1} (m, C-H), 1351 cm^{-1} (m, C-N, pyridine), 1250 cm^{-1} (m, C-O), and a broad, strong peak at ~1060 cm^{-1} (s, C-O and C-N). Briefly comparing with reported data for 2,6-diacetylpyridine, the reported very strong peak at 1700 cm^{-1} associated with the carbonyl groups is not significantly present in Mn3N2O, which assists in establishing the reaction of 2,6-diacetylpyridine with the associated ligand, 1,8-diamino-3,6-dioxaoctane.[64]

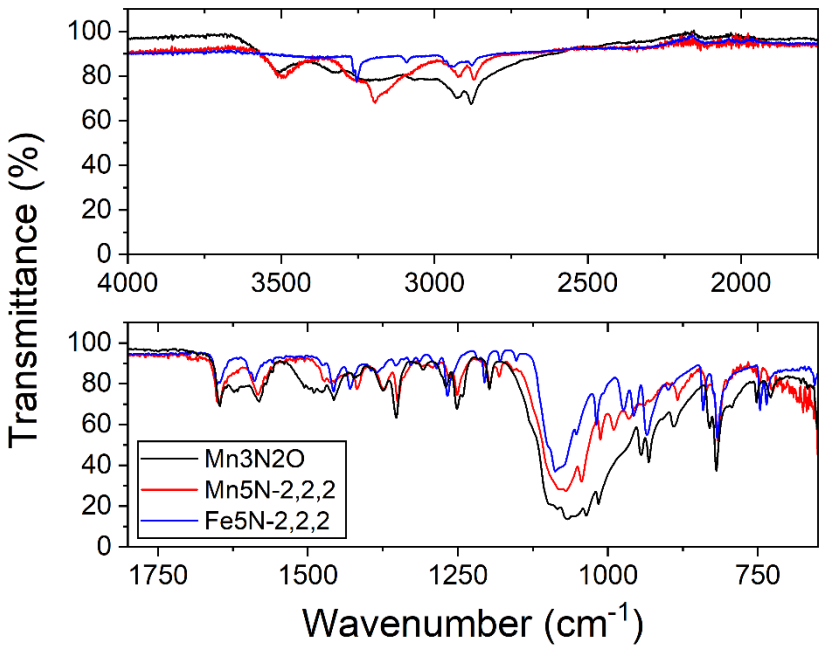

Figure 33: FTIR readings of samples Mn3N2O, Mn5N-2,2,2 and Fe5N-2,2,2.

With samples Mn5N-2,2,2 and Fe5N-2,2,2, strong similarities were found in the lower region (1800 – 600 cm^{-1}), with some moderate differences in the upper region (4000-1800 cm^{-1}) (Figure 33). In this upper region, Mn5N-2,2,2 presented peaks at 3494 cm^{-1} (m, N-H), 3199 cm^{-1} (m, N-H), 2916 cm^{-1} (m, C-H) and 2871 cm^{-1} (m, C-H). Fe5N-2,2,2 presents a peak at 3254 cm^{-1} (m, N-H), 2940 cm^{-1} (m, C-H) and 2877 cm^{-1} (m, C-H), notably lacking the absorption at 3494 cm^{-1}. In the lower region (1800 – 600 cm^{-1}), notable peaks are 1648 cm^{-1} (m, N-H), 1582 cm^{-1} (m, C=C), 1455 cm^{-1} (m, C-H), 1429 cm^{-1} (m, C-H), 1375 cm^{-1} (m, C-H), 1351 cm^{-1} (m, C-N), 1267 cm^{-1} (m, C-N) and 1083 cm^{-1} (m, C-N). Fe5N-2,2,2 does not strongly present the peaks at 1375 cm^{-1} and 1351 cm^{-1} seen with Mn5N-2,2,2 and Mn3N2O.

Chapter 4: Heterogeneous Catalysis

4.1 – Preamble

Early during the exploration of the macrocycle complexes and soon after the adjustment of the reaction solvent to 95% ethanol from 50:50 water/ethanol, it was decided to try an experimental run with copper in an attempt to form the macrocycle complex similar to Mn3N2O. Although it had been reported previously that this type of macrocycle formation was not possible, there was a few positive aspects in attempting this regardless.[56] One is that the general synthesis is relatively straight-forward, although some live adjustments based on observations were necessary to obtain a successful product. Another is that copper complexes have shown reductions in the general area for water reduction, with some possibility that the previous authors had some deviation in testing that made their macrocycle synthesis unsuccessful. Even though these authors were the ones that led to the earlier shift to 95% ethanol solvent use, some small changes could lead to different outcomes. At this time, heterogeneous catalysis was not in the scope for possible objectives. However, certain discoveries such as the formation of a thin film on the working electrode and the formation of bubbles under applied potential gave this area an increased interest and culminating into the main focus for the remainder of this thesis.

Three complexes will be covered in this chapter, with a focus on formation of electrode films and the heterogeneous catalytic abilities of these films towards HER and electrolysis of water. Specifically, the three complexes schematically shown in Scheme 10.

These are Dibromo-(2,13-dimethyl-6,9-dioxa-3,12,18-triazabicyclo[12.3.1]octadeca-1(18),2,12,14,16-pentaene-κN^3,κN^{12},κN^{18},κO^6,κO^9)-copper(II) (Cu3N2O), Dichloro-(N1',N3-ethane-1,2-diyldipropane-1,3-diamine)-nickel(II) (Ni4N) and Dibromo-(N1',N3-ethane-1,2-diyldipropane-1,3-diamine)-copper(II) (Cu4N). Initial exploration was performed on Cu3N2O, with the main focus settling on Ni4N's capabilities and Cu4N created for a supplemental comparison. These complexes were synthesized by direct reaction of the divalent metal halide and the appropriate chelating ligand (Scheme 11) with full details in the Experimental Details at the end of the chapter.

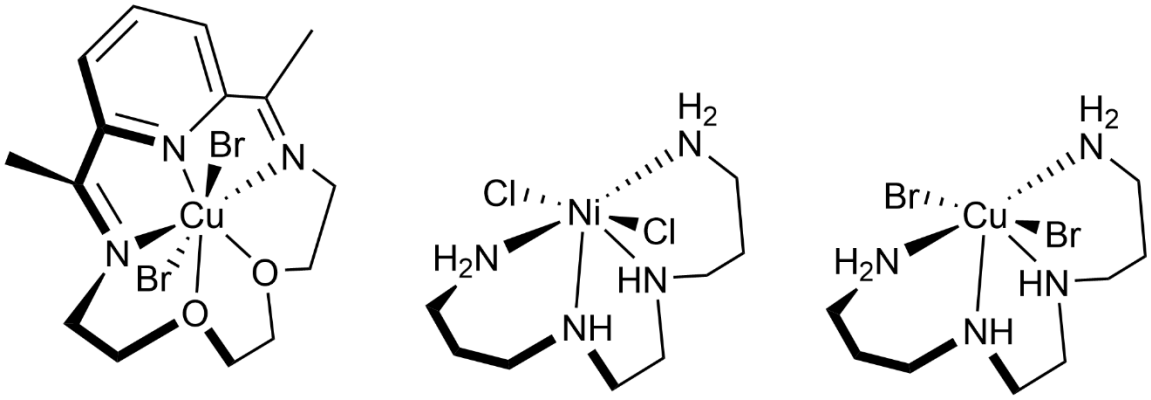

Scheme 10: General scheme for Cu3N2O, Ni4N and Cu4N complexes.

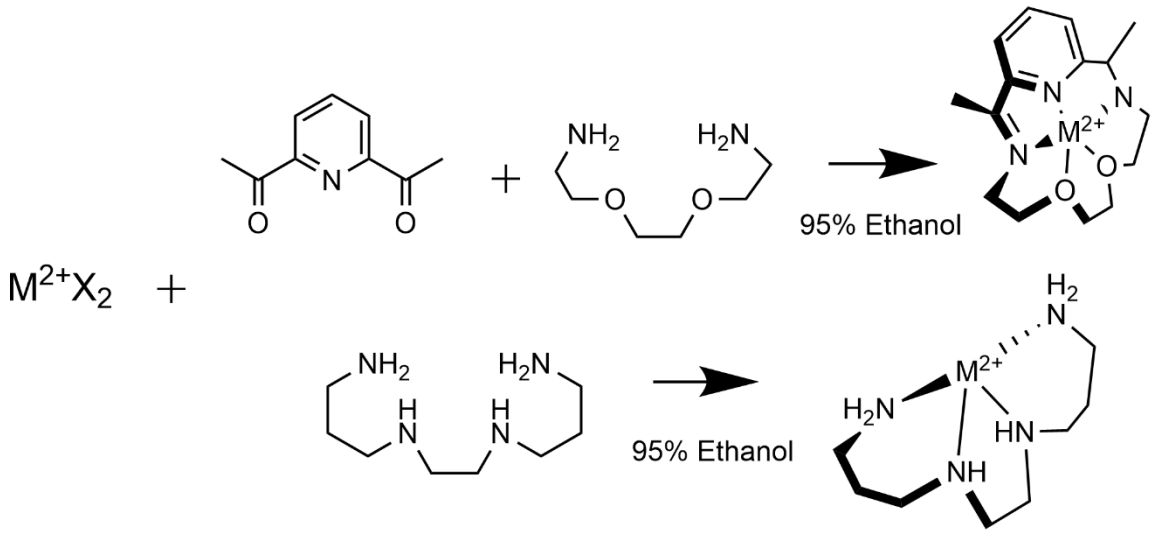

Scheme 11: General synthesis path for the three complexes Cu3N2O, Ni4N, and Cu4N.

4.2 – Cu3N2O

Electrochemical testing of Cu3N2O was done using acetonitrile with incremental additions of water up to 11 M to the initial 15 mL solution (Figure 34). Initial scans from 0 to -2.5 V (*vs.* Ag wire) revealed no detected electrochemical events. This appeared to be an issue with the solubility and a large amount of precipitate (undissolved complex) remained at the bottom of the electrochemical cell. Additions of water resulted in improved solubility and gave rise to the appearance of two clear reduction peaks at -0.70 V and -1.10 V. Associated oxidation peaks at -1.06 V and -0.66 V (*vs.* Ag wire) displayed smaller current responses. With continued addition of water, these events shifted in potential and the reduction peaks gave increased currents. The maximum current was observed with addition of 7.4 M water (Figure 35). At this point the first reduction appeared at -0.53 V and the second at -0.93 V. Similarly, the oxidation peaks also shifted.

With a total addition of 11 M of water, the reduction events appeared as a single event at -0.83 V and oxidation peaks appeared to have become a single event at -0.37 V. These observations are thought to be associated with an irreversible reaction or complexation with water. Further exploration of these results revealed that this complex will deposit and form a layer that can effectively produce hydrogen.

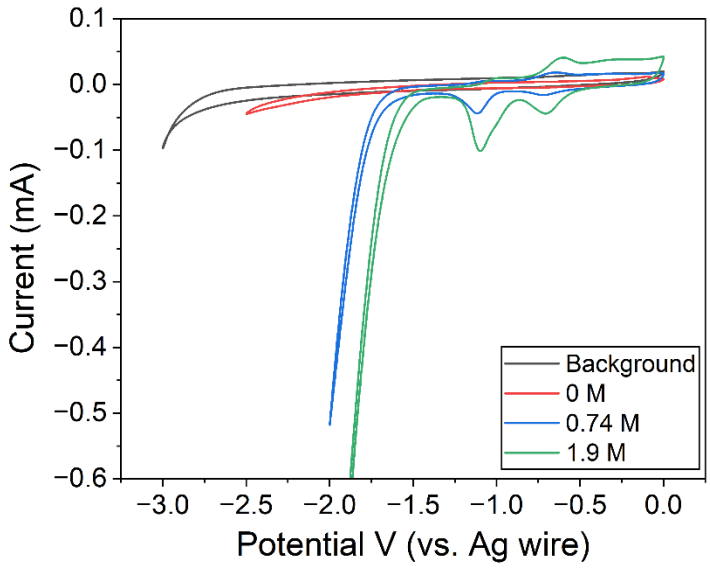

Figure 34: Cyclic Voltammetry under cathodic potentials (*vs.* Ag wire) of Cu3N2O in 15 mL acetonitrile and 0.1 M TBAHFP as electrolyte, without complex present (black), with 1.0 mM Cu3N2O (red), and with additions of 0.74 M water (blue), 1.9 M water (green).

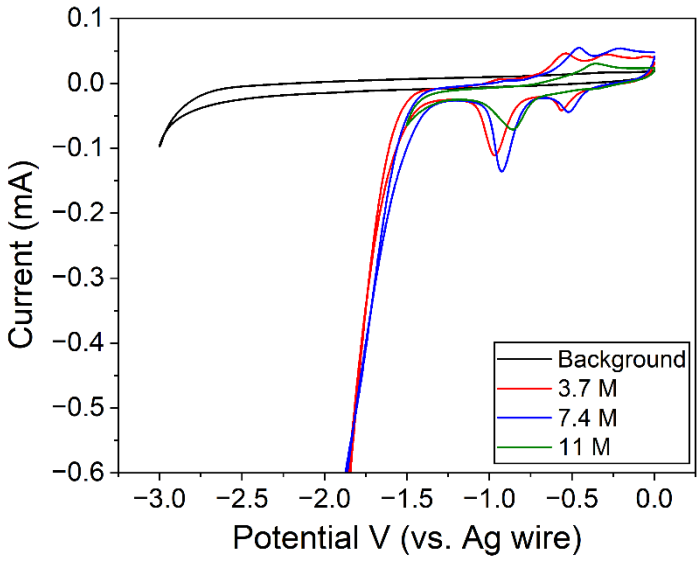

Figure 35: Cyclic Voltammetry under cathodic potentials (*vs.* Ag wire) of Cu3N2O in 15 mL acetonitrile and 0.1 M TBAHFP as electrolyte, without complex present (black), and with 1.0 mM Cu3N2O with 3.7 M water (red), 7.4 M water (blue), 11 M water (green).

Further testing was performed with Cu3N2O in 15 mL 0.1 M KCl aqueous solution, with later additions of acetic acid to test viability of hydrogen production with that substrate. Scanning from 0 to -2.0 V (*vs.* Ag wire) in the absence of AcOH, there was an immediate strong current response past ~-1.2 V (*vs.* Ag/AgCl) (Figure 36). An interesting peak formed at -1.56 V, with a current of ~386 µA, indicating the reaction of the complex with water at this reduction event. More importantly though, repeated scans significantly strengthened this current response with each pass, with magnitudes well into the mA level. Two associated peaks also began to appear at this time – a reduction peak around -0.64 V and some overlapping oxidation peaks around -0.27 V. It is difficult to firmly define these peaks as being located at a certain potential, especially with the strong reduction

peak having some variability. Once the scans appeared stable, one scan from 0 to -1.5 V was done with the reduction peak seen at -0.60 V. However, scans performed to more negative potentials, from 0.5 to -1.7 V, displayed a reduction peat at -0.80 V. Generally, this is thought to be a merging of catalytic events from the complex still present in solution and of the coating that has been created on the surface of the electrode. Some mild gas bubbles were observed to be formed on the working electrode during these CV trials before acetic acid additions.

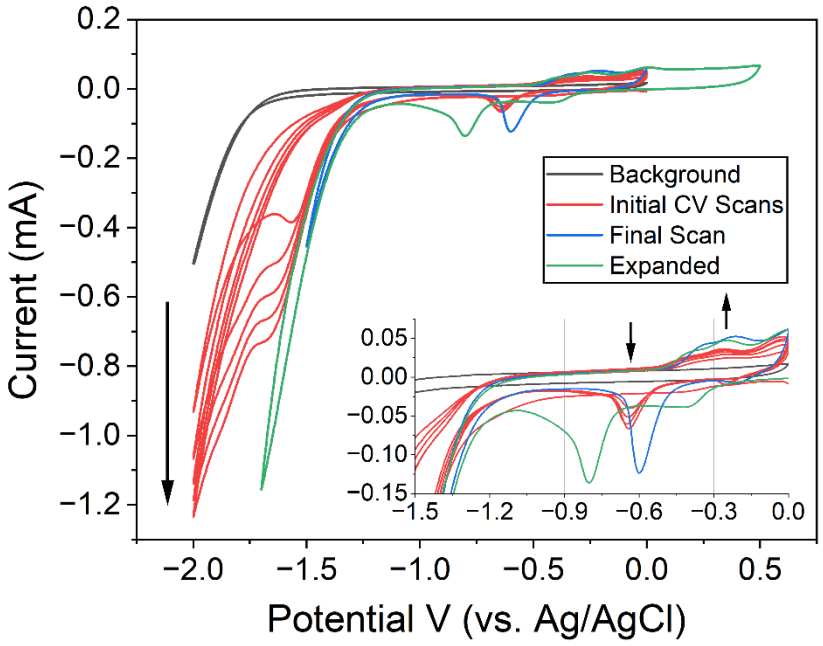

Figure 36: Cyclic Voltammetry under cathodic potentials (*vs.* Ag/AgCl) of 1.0 mM Cu3N2O in 0.1 M KCl aqueous solution, without complex (black), initial continuous scans of the sample (red), an expanded window from 0.5 V to -1.7 V (green), and the final scan before AcOH additions (blue). Inset graph in bottom right is a zoomed view of the main graph.

Testing proceeded with acetic acid additions being incrementally added from 0.02 M to 0.28 M, dissolved in a 1:4 ratio with water for higher accuracy additions. With acid concentrations of 0.02 M an immediate response appeared with an increase of current starting around -0.7 V, and a strong reduction peak forming at -1.08 V at 148 μA (Figure 37). The return oxidation scan closely follows that of the original solution without acetic acid present. Interesting is that the previous reduction/oxidation peaks have disappeared and is now marked with a reduction at -0.13 V and an oxidation past 0 V. Sequential additions increases the enhancement trend past the onset at -0.7 V, with 0.05 M forming the reduction peak at -1.19 V and 532 μA, and 0.08 M AcOH at approx. -1.32 V and 1.03 mA. With additions to 0.08 M and higher, the reduction peak becomes less clear, and the overall reduction becomes linear. Additions of AcOH begin to have negligible impact on current increases from 0.16 M to the final addition to 0.28 M. For comparison, the final current at -1.5 V for 0.16 M was ~2.7 mA, with 0.28 M at ~3.0 mA.

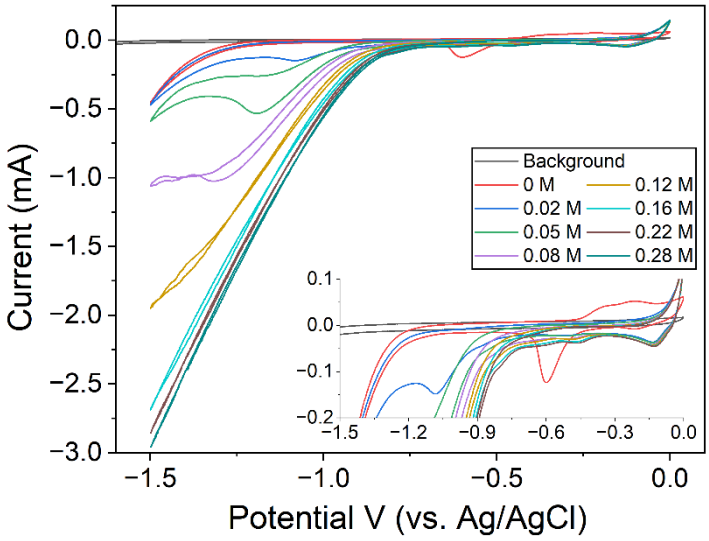

Figure 37: Cyclic Voltammetry under cathodic potentials (*vs.* Ag/AgCl) of Cu3N2O in 0.1 M KCl aqueous solution, without complex present (black), without acetic acid present (red), and with additions of acetic acid as shown from 0.02 M to 0.28 M. Inset graph in bottom right is a zoomed view of the main graph.

During the previous trials in the absence of acetic acid, evidence of hydrogen formation was indicated by visual observation of gas bubbles forming on the electrode. This led to testing with 0.1 M KCl aqueous solution using a graphite electrode as the WE in an attempt to produce hydrogen via electrolysis from water. For this test, CPE was performed at -1.3 V (*vs.* Ag/AgCl) held for 1 h. Gas bubbles formed on the WE disperse over time, with bubbles accumulating on the surface as foam. After the run and during cleaning, a shiny copper-colour coating was observed at the bottom of the graphite electrode (~0.5 cm height), with a blue colour coating (~0.5 cm) forming closer to the top where it would meet the air/solution general interface. These coatings are suggested to

be copper metal and copper hydroxide species by visual colour assessment alone. Using cyclic voltammetry to compare before and after state of the WE, the overall current increased after the experiment, at -1.5 V from 6.2 mA to 9.0 mA (Figure 38). The hydrogen gas as detected by GC-TCD was 24.2 µmol (Appendix, Table 13), noting this quantity to earlier results occurring at a significantly lower overpotential (-1.3 V *vs*. Ag/AgCl to ~-2.1 *vs.* Fc/Fc^{+}). This was remarkably comparable to Majumder et al.'s results of 21.6 µmol with their copper-based complex.[28] Although in this comparison, it should be noted that differing test parameters regarding the FTO glass, surface area, pre-coating, cell headspace and voltages (-1.3 V for 1 h *vs.* -1.2 V for 4000 s) are significant considerations. This group's findings would continue to be a valuable reference in detailing future experiments and testing criteria.[28]

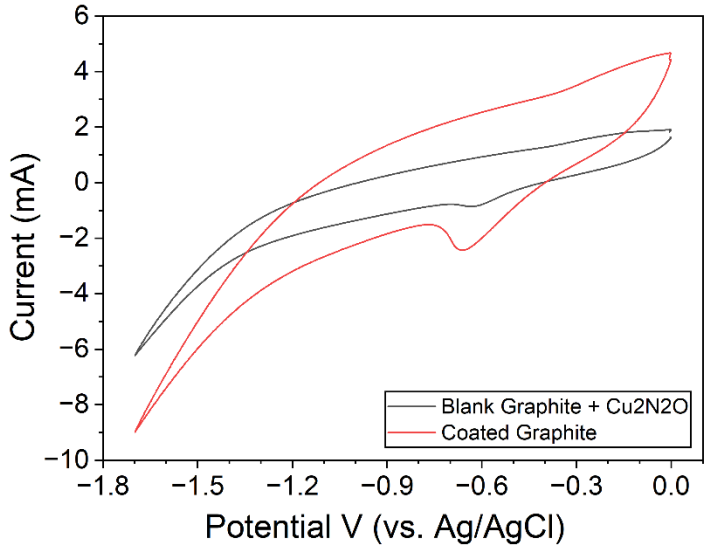

Figure 38: Cyclic voltammetry under cathodic potentials (*vs.* Ag/AgCl) for coating a graphite WE with Cu3N2O in 0.1 M KCl aqueous solution, before coating (black) and after coating (red).

As a final comparison point to confirm the effectiveness of the Cu3N2O-derived films over that of copper metal, background measurements were carried out using copper wire as the WE as a comparative model. The copper wire was finely sanded down to clean the surface immediately before use as the working electrode. A CV scan from 0 to -1.7 V (*vs.* Ag/AgCl) was performed before and after testing, showing a similar reduction peak to Cu3N2O at -0.6-0.7 V, although with minor shifts (Figure 36, 38, 39). It should be noted that during voltage measurement more cathodic than -1.5V (~4 s per pass), minor gas bubbles began to form on the copper wire electrode, indicating that it will function for electrolysis past those points. Afterwards, CPE was conducted at -1.3 V for 3600 s. Despite observed bubble formation during CV testing, the hydrogen that was detected was negligible at only 1.2 μmol. With this result, it was generally determined that plain copper as a working electrode at -1.3 V is beyond the range of concern for background comparison and reinforces -1.3 V and below as a suitable target for testing. Overall, Cu3N2O was not further explored this point for heterogeneous catalysis, as Ni4N gradually indicated to be a superior option in terms of total hydrogen production, but Cu3N2O remains an interesting species in this regard.

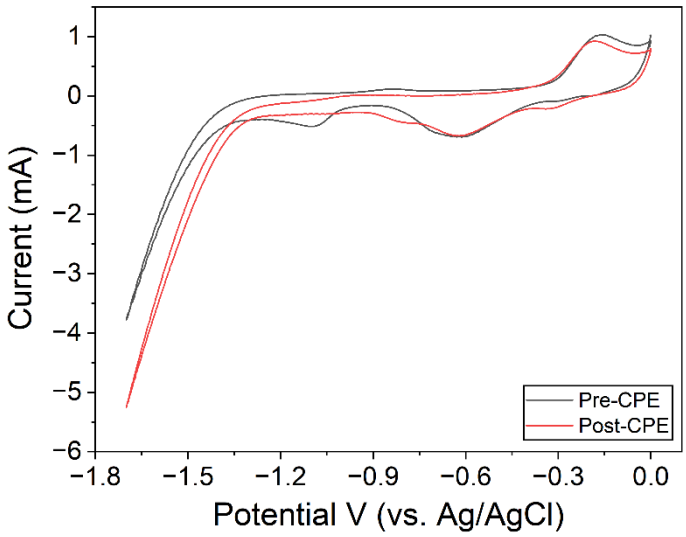

Figure 39: Cyclic voltammetry under cathodic potentials (*vs.* Ag/AgCl) of a copper wire as the WE in 0.1 M KCl aqueous solution, with before (black) bulk CPE at -1.3 V for 1 hr and after CPE (red).

4.3 – Ni4N

4.3.1 – Preliminary Electrochemical Investigation

The investigation of Ni4N continued from the findings using Cu3N2O, specifically towards film formation and heterogeneous HER in water. Literature support for this approach was found for some analogous use of copper-based complex for the formation of Cu-based films.[28] Nickel presented an opportunity for comparison with these previous findings, and particularly with determining the efficacy of copper *vs.* nickel. This work began with the attempted synthesis of a nickel macrocycle using the template method previously described with 2,6-diacetylpyridine and 1,2-bis(3-aminopropylamine)ethane (1,2-bis) used for ligand construction. This reaction yielded crystals viable for single crystal

XRD that revealed the formation of a complex that consisted of $NiCl_2$ coordinated with the starting tetraamine, 1,2-bis, as shown in Scheme 11. Therefore, this complex was further synthesized by the direct addition of 1,2-bis to $NiCl_2$ in ethanol. The complex was then examined as a starting material for possible film formation under similar conditions that were used with Cu3N2O.

Initial testing with Ni4N focused on water electrochemistry and comparing results to that of Cu3N2O, primarily for overall current in the -1.0 V to -1.5 V region (*vs.* Ag/AgCl) for electrolysis targeting. Cyclic voltammetry was performed with a glassy carbon WE in 0.1 M KCl aqueous solution with an Ag/AgCl reference electrode (3 M KCl), and platinum wire as counter electrode with 1.9 mM Ni4N complex present (Figure 40). The initial CV from 0 to -1.5 V displayed a strong deviation from that of background, with a reduction onset around -1.0 V. The indications of heterogeneous activity here are less certain than was observed in Cu3N2O, with the lack of a defined peak and substantial growth of current with each pass (Figure 36). However, a small cross-over event is observed with the first pass at -1.35 V. This cross-over of the current is a typical sign of a heterogeneous reaction occurring as well – a reactant present in solution agglomerating to the electrode surface which may modify conductivity with the solution and thus the changes in current. Continuing to -2.0 V the current is significantly stronger, with 3.6-4.0 mA observed with Ni4N versus the maximum of 1.2 mA with Cu3N2O. At -1.5 V the difference is less significant, with Ni4N in the 0.5-0.6 mA range and Cu3N2O within 0.4-0.5 mA. Visually at the end of testing, the glassy carbon WE had a grey coating on the surface. With the

overall high current strength and the formation of a film on the WE, further examination with Ni4N continued.

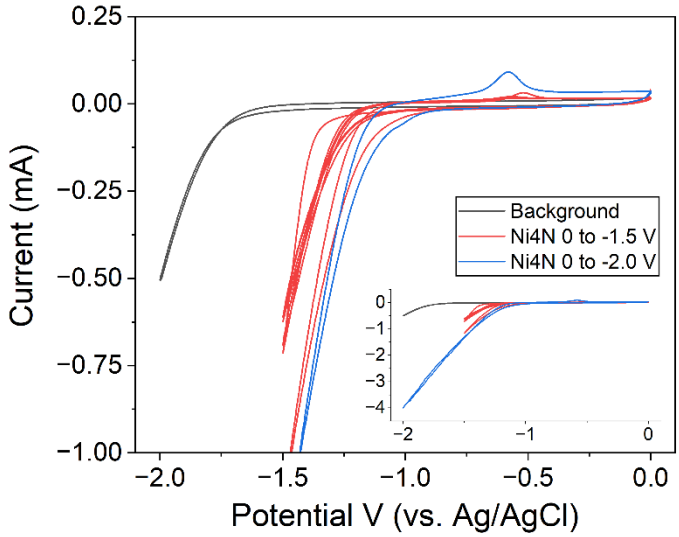

Figure 40: Initial CV under cathodic potentials (*vs.* Ag/AgCl) with 1.9 mM Ni4N in 0.1 M KCl aqueous solution, showing background without complex (black), initial CV from 0 to -1.5 V (red), and from 0 to -2.0 V (blue). The inset graph is an expanded view of the CV.

Heterogeneous hydrogen production was examined following an analogous process as was used with Cu3N2O, using a graphite working electrode, 1.9 mM of Ni4N complex immersed into a 0.1 M KCl aqueous solution with an Ag/AgCl reference electrode and platinum mesh counter electrode. The cell was purged with nitrogen and sealed with parafilm. After initial CV scans were complete, CPE was performed at -1.3 V (*vs.* Ag/AgCl) for 1 hr, with the hydrogen analysis by GC. The graphite rod has a strong overall current, but the overall current increases after the coating process, increasing from 5.3 mA to 9.4 mA at -1.5 V (Figure 41). Compared to Cu3N2O's 6.2 mA to 9.0 mA, this is a relatively large

increase (77% *vs.* 45%). However, the main results arose from hydrogen production. From the coating process 29.0 µmol was found to be produced (24.2 µmol for Cu3N2O), with the prepared coated electrode in fresh solution producing 52.9 µmol (Appendix, Table 13). These observations and the fact that HER seemed slightly higher than with Cu3N2O encouraged further investigation. Visually, the coat itself appeared dull grey on the graphite.

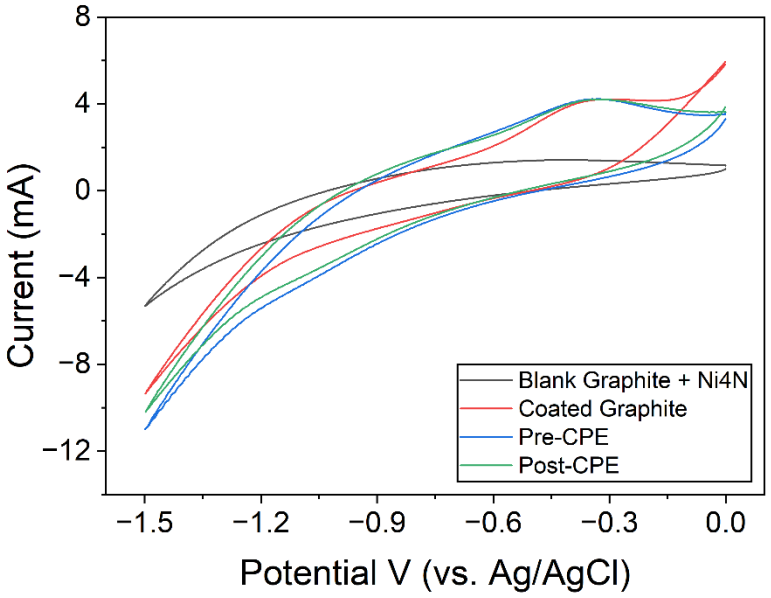

Figure 41: Cyclic voltammetry under cathodic potentials (*vs.* Ag/AgCl) for 1.9 mM Ni4N with 0.1 M KCl aqueous solution using a graphite WE, showing the blank graphite with Ni4N (black), the coated graphite (red), pre-CPE (blue) and post-CPE (green).

4.3.2 – FTO Glass as the Working Electrode

At this point a more suitable electrode for coating was desired, as continuously coating the graphite rod may eventually incur damage or passivation of some kind, as well as needing to have a consistent known surface area of exposure. A disposable electrode that has the capability to send out samples for testing or harsher experiments was also noted, including cutting of samples for equipment sizing requirements. FTO glass was chosen due to fulfilling these requirements, as well as it being a common for working electrodes. It is critical to consider that there is a wealth of variables that can be considered with varying amounts of significance on the total outcome. Some of note include: (1) FTO surface area immersed, (2) FTO electrical connection to solution contact distance, (3) FTO surface cleanliness, (4) electrolyte concentration, (5) electrolyte choice, (6) catalyst concentration, (7) start/end pH, (8) purging of DI water, (9) electrode type (FTO vs ITO, graphite, GC, etc.), (10) electrode distance, (11) stir bar effect both positive/negative, (12) solution/headspace volume, (13) potential set for coating, (14) time of coating, (15) potential/time of coating on impact of surface stability. The surface area of the FTO glass was generally held as the most significant of these variables on performance, as it modifies the amount of surface-interaction with the solution and thus impacts current flow amounts. This in turn has the most direct correlation with the total formation rate of hydrogen as that formation of product naturally necessitates interaction with the working electrode. The FTO glass preparation and coating details are listed in the experimental details section.

The majority of these variables were standardized, and attempts were made to minimize them in the testing and characterization, but likely several variables will require further investigations for their specific impact. With this in mind, most attention focused on identifying optimal catalyst concentration and the interactions of the catalyst with the FTO plate, specifically with the goal of maximizing hydrogen production. Particular attention was given to the characteristics needed for water electrolysis onset parameters for comparison and consideration of the real-world production applications. This is important as the primary complex highlighted here (Ni4N) has recently in 2012 been examined for electrochemical activity in a similar water electrochemical cell.[65] These researchers specifically state restricting their CV scans to not go beyond -1.2 V versus their 1 M KCl reference electrode, since 'below that voltage the reduction of the solvent (water) started to dominate the electrochemistry'.[65] However, it is argued here that if an added complex's presence will substantially affect the electrochemistry, it can still be observed past the background reduction as seen in Figure 40. Furthermore, it is generally noted in even teaching literature that 'While the thermodynamic potential difference required to drive water electrolysis is theoretically 1.23 V, significant overpotentials (η) are required to achieve a desired current density on both electrodes kinetically'.[17] As a result of the cathodic potential not reaching values less than -1.2 V, these researchers did not fully appreciate the electrochemical significance of this particular complex, at least in terms of heterogeneous catalysis, and thus potentially limiting further electrochemical research for this complex. An example for the visualization of the coated samples can be seen below in Figure 42. With the subsequent trials, guidance and comparisons would continue

to be used with Majumder et al.*'s* copper complex results, as briefly mentioned in Cu3N2O's results.[28]

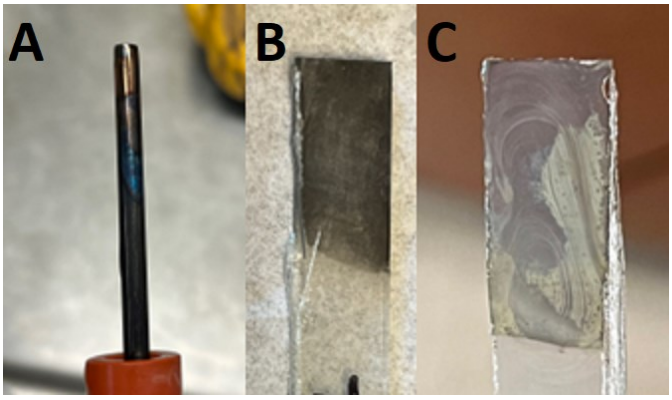

Figure 42: Examples of coated samples of Cu3N2O on a graphite electrode (A), a Ni4N-coated FTO glass (B), and a Cu4N-coated FTO glass with salt deposits remaining on surface (C).

Compared against FTO glass without complex presence via the same procedure, it shows a highly repeatable linear trend, starting a slow increase in current at -1.2 V and more rapidly around -1.3 V (Figure 43). The after graph shows an affected electrode, with an increase in current around -0.42 V, ramping down to around -0.70 V and 60 µA. The curve inclining for the potential window also occurs earlier, generally declining around -1.05 V and more rapidly around -1.2 V instead. While the overall current density is significantly less than that of the coated variant, perhaps a magnitude less, this suggests that the FTO glass is not entirely inert or non-affected by experimentation in this setup and has some potential of affecting the CV shape or hydrogen production itself. Overall, hydrogen production was deemed the critical factor to consider, and it was determined as negligible at 1.2 µmol and comparable to background.

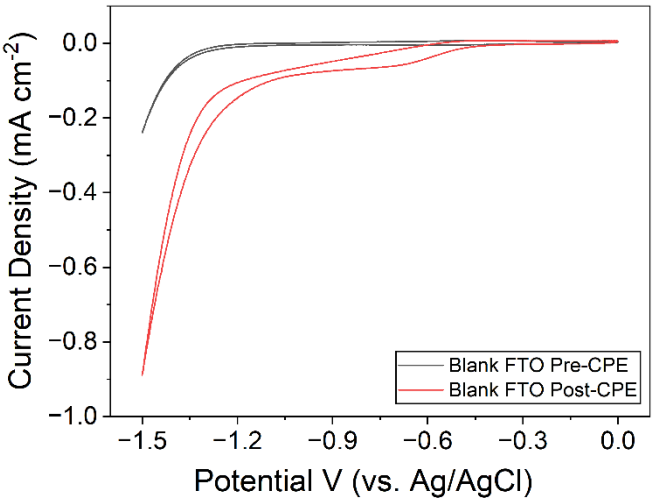

Figure 43: Cyclic voltammetry under cathodic potentials (*vs*. Ag/AgCl) in 0.1 M KCl aqueous solution comparing a blank FTO glass before (black) and after (red) bulk CPE testing, with no complex present in solution.

4.3.3 – Electrochemical Characterization with FTO Glass

Investigation of the electrochemical features for the FTO glass in 0.1 M KCl aqueous solution began with a CV scan in the absence of a complex. The appearance was very similar to a glassy carbon WE and displayed a flat current trend until an onset of ~-1.1 V (*vs.* Ag/AgCl) (Figure 44). At -1.5 V, the maximum current density is 0.12 mA cm^{-2}, representative of the background behavior. With the addition of 1.9 mM Ni4N into solution, cyclic voltammetry follows a similar profile to that of testing Ni4N with a glassy carbon WE. The current with solutions of Ni4N increase from the first to second voltametric cyclic, changing from 1.3 mA cm^{-2} to 2.0 mA cm^{-2}, then settling to 1.3 mA cm^{-2}. In addition, a cross-over event is apparent with the first scan, a signature of film formation.

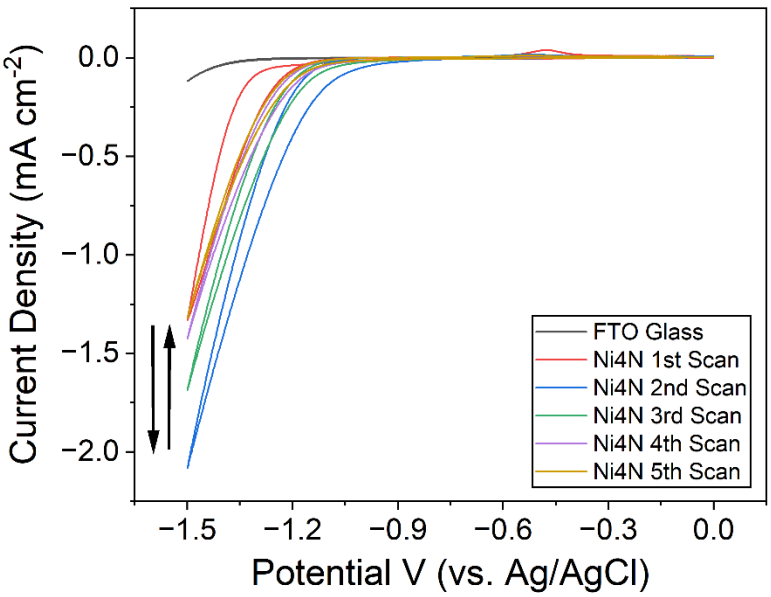

Figure 44: Initial CV scans under cathodic potential (*vs.* Ag/AgCl) of an FTO glass showing background without catalyst (black), and sequential scans with Ni4N complex present.

An important consideration on the overall film forming process is the impact of cycling the voltage after coating. Figure 45 shows the relative impact that continuous scans can have on reduction and oxidation events, even from low variations of voltage from 0 to -1.5 V (*vs.* Ag/AgCl). Broadly, during reduction, the baseline current during the first cycle of ~0.5 mA cm^{-2} increased, by the sixth cycle, to 1.6 mA cm^{-2} at -1.1 V. In addition, there is a corresponding oxidation event at -0.3 V that also increases from 1.4 mA cm^{-2} to 2.2 mA cm^{-2} with an increasing number of voltage cycles. The possible impact of this on the experiment was recognized, however in evaluating if a FTO glass was successfully coated, the responsiveness and strength of current with the film was important in predicting overall performance in hydrogen testing. Generally, if the overall

current was reduced during CV, it could be expected to perform proportionally lower. To standardize potential impact, the post-coating cyclic voltammetry were typically held at a maximum of three scan cycles. However, this area could be explored further for exact effects on total outcomes such as hydrogen production, and film surface morphology.

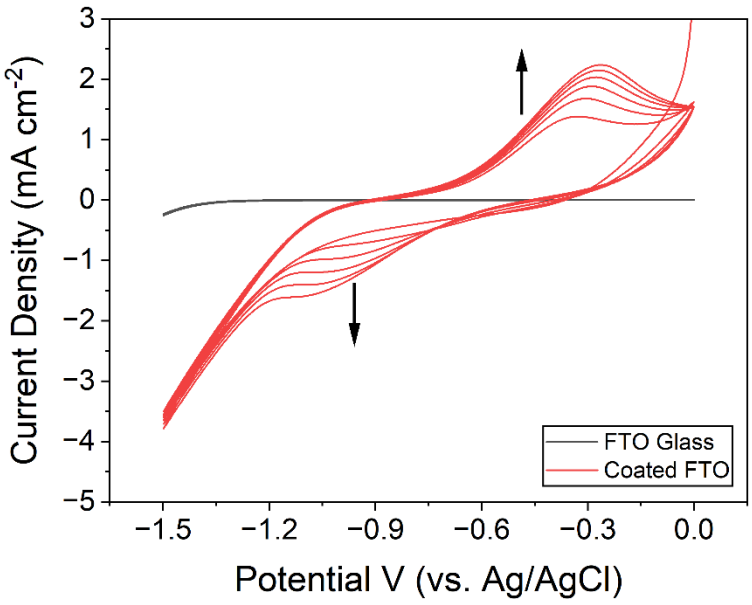

Figure 45: Post-coating cyclic voltammetry under cathodic potentials (*vs.* Ag/AgCl) for Ni4N (red), showing continuous CV passes and the impact on detected reduction and oxidation events. FTO glass without complex present (black) is included as reference.

4.3.4 – Background Comparison with $NiCl_2$ and FTO Glass

To examine if the presence of the polyamine ligand was essential for these observations, a simple nickel salt $NiCl_2{\cdot}6H_2O$ was examined for comparison. A similar approach was described for the Cu work of Majumder et al.*'s* work where they used $CuCl_2$

as their comparative analogue.[28] Identical processing steps was performed with $NiCl_2 \cdot 6H_2O$ under CPE conditions at -1.3 V (*vs.* Ag/AgCl) for 1 h, with CVs conducted before and after. With the CVs, an interesting peak develops with both $NiCl_2$ and Ni4N, with a peak at -1.04 V with 0.19 mA cm^{-2} for $NiCl_2$ and a significantly stronger response from Ni4N at the same potential of 1.62 mA cm^{-2}, with the peak broadly in the -1.1 V region (Figure 46). A significant return oxidation event is observed for both $NiCl_2$ and Ni4N, presenting at -0.25 V and 0.16 mA cm^{-2} for $NiCl_2$, and -0.30 V with 2.15 mA cm^{-2} for Ni4N. The general shape and appearance of the post-CPE CV is very similar to that for Ni4N; however, the magnitude of current is significantly less. The current strength at -1.5 V is at ~0.45 mA cm^{-2} for $NiCl_2$, whereas Ni4N is at ~4.3 mA cm^{-2}.

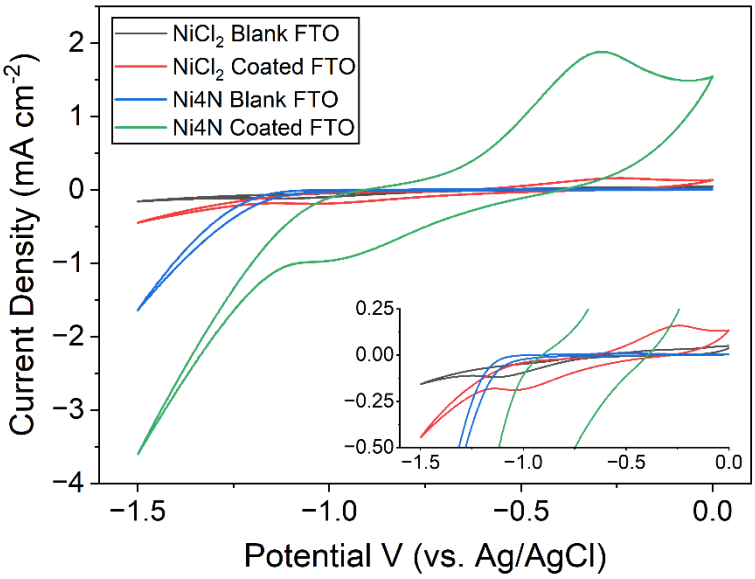

Figure 46: A comparison of cyclic voltammetry (*vs.* Ag/AgCl) for coating an FTO glass in 0.1 M KCl aqueous solution, with 1.0 mM $NiCl_2 \cdot 6H_2O$ with an initial blank FTO (black) and $NiCl_2$-coated FTO (red), 0.5 mM Ni4N with the initial blank FTO (blue), and Ni4N-coated FTO (green). Inset graph in the bottom right is a zoomed view of the main graph.

Visual observations of the films provided another important difference between these two starting materials. For example, the films formed from $NiCl_2$ appear to be darker than those from Ni4N. During reduction, bubble formation was only observed in the case of the Ni4N originated films and was absent for $NiCl_2$ derived films. Notably, the production of hydrogen was also particularly low for films generated from $NiCl_2$, providing only 2.6 μmol of H_2. With the similarities in CV shape between Ni4N and $NiCl_2$, it can be reasoned that nickel substrates are likely being formed on some level on the surface of the FTO glass. However, the stability and exact molecular method of coating must significantly differ, with the $NiCl_2$ discolouring the glass grey enough to be fairly opaque. The significant differences in overall current strength, along with hydrogen production amounts and general visual observations, suggest that although $NiCl_2$ films are similar to those obtained from Ni4N, as the post-coating CV does show strong similarity in shape, the quality of the films is much lower in quality.

4.3.5 – CPE during Ni4N-Coating Process

The previous CV scanning would be followed with CPE at a potential -1.3 V (*vs.* Ag/AgCl) held steady for 3600 s as part of the electrodeposition process. For baseline comparisons, samples with 1 mM of $NiCl_2$ in place of Ni4N and with FTO glass alone were run under the same initial conditions, with their individual CV analysis carried out after this process. These results are displayed in Figure 47. The sample with Ni4N stands out with a rapid increase in current density early in the process that levels out at 1.75 mA cm^{-2}

(Figure 47). The test with $NiCl_2$ also rapidly increased to 0.15 mA cm^{-2}, however this immediately levelled out and approximately remained at this current for the duration. The bare FTO in contrast started with a lower initial current of 0.02 mA cm^{-2} and gradually approached an end current of ~0.16 mA cm^{-2} similar to the $NiCl_2$ sample. Hydrogen production was also compared. Although these runs were tested during the coating process, typical hydrogen production during coating can minimally range from 23 to 26 µmol using the Ni4N catalyst, occasionally going above. $NiCl_2$ and FTO glass during this same process yield only 2.6 µmol and 1.2 µmol respectively.

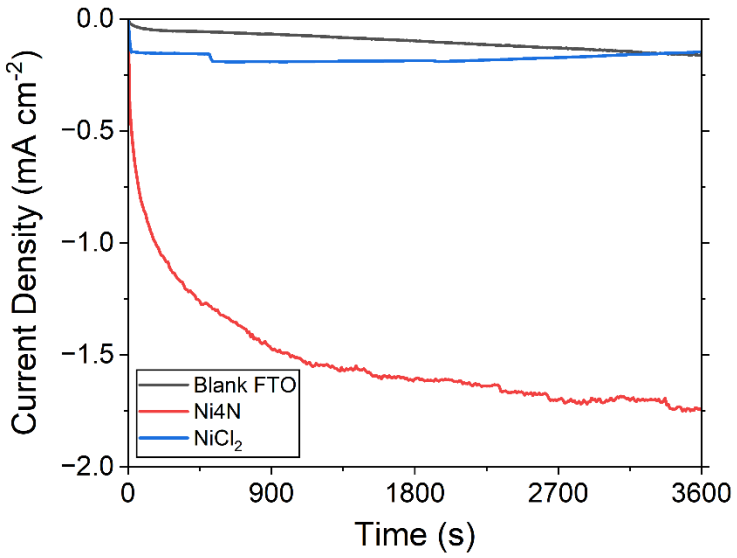

Figure 47: CPE results for the electrodeposition process in 0.1 M KCl aqueous solution of a blank FTO plate without complex presence (black), 0.5 mM Ni4N (red) and 1.0 mM $NiCl_2$ (blue), held at -1.3 V (*vs.* Ag/AgCl) over 3600 s.

4.3.6 – Ni-Coated FTO Surface Characterization

Surface characterization for the Ni-coated FTO samples were performed by Dr. Jurca's research group. Key analysis numbers and initial graphs were provided by them, with further graph refinement, discussion points provided by myself. To assess the surface morphology and composition, characterization was done by scanning electron microscopy with energy dispersive spectrometer (SEM-EDS), atomic force microscopy (AFM), energy dispersive X-ray spectroscopy (EDX) analysis, X-ray photoelectron spectroscopy (XPS), and powder X-ray diffraction (XRD) with full details provided in Section 4.6. Two overview examples are provided here. The surface morphology of the Ni4N-coated FTO sample by SEM can be seen in Figure 48 at 1 µm scaling. The coating appears to be a fairly regular pattern, with evenly distributed irregularites across the top layer. Closer features are noted to be spherical formations that may range from 100 to 300 nm in size, forming non-uniform protrusions and channels on the surface. The XPS survey is shown in Figure 49, showing a strong response at 856 eV and 532 eV, fitted with experimental data to Ni 2p and O 1s respectively, with O 1s identified for metal-oxygen/$(OH)_2$ species and of chemisorbed water. This contributes significantly to the finding for this coating to be comprised primarily from NiO/$Ni(OH)_2$. Further examination of these elements by high-resolution XPS is provided in Section 4.6.

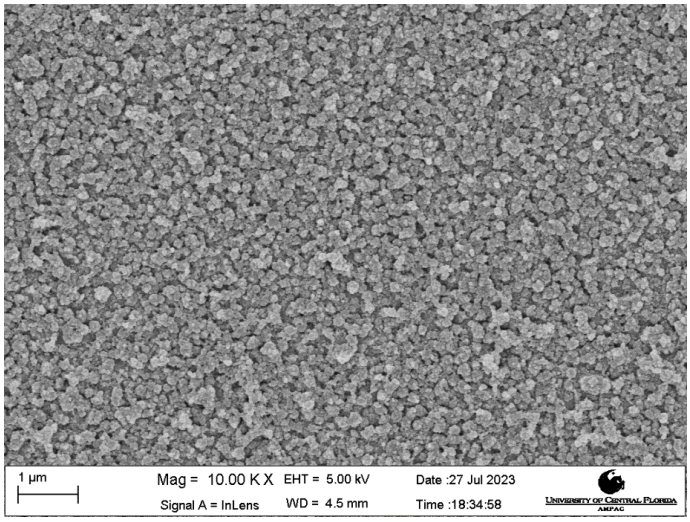

Figure 48: SEM-EDS imaging of a Ni4N-coated FTO species, scaling at 1 µm.

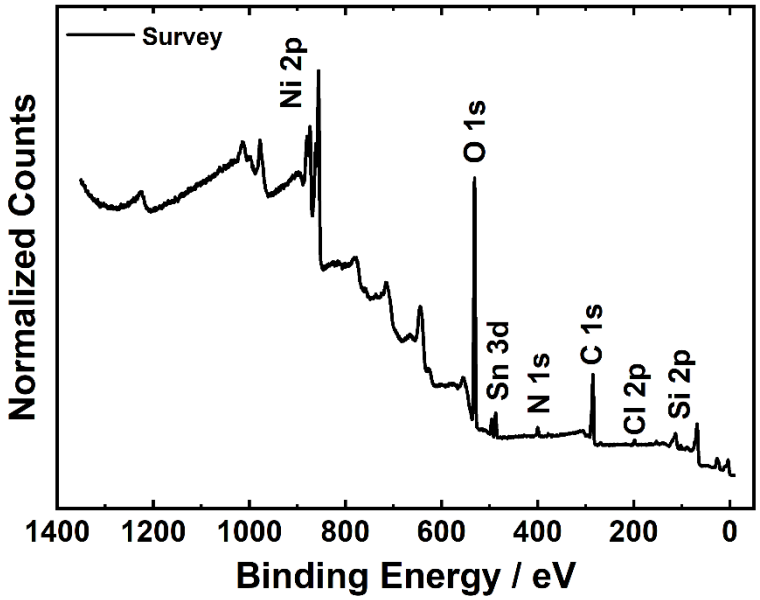

Figure 49: XPS survey for a Ni4N-coated FTO sample, with fitted experimental (black) and associated deconvoluted peaks.

4.3.7 – Ni-Coated FTO Glass Oxidation CV

For a comprehensive examination of the Ni-coated FTO electrode, oxidation electrochemistry was initially performed by CV from 0 to 1.0 V (*vs.* Ag/AgCl). This investigation was to establish if OER-type catalysis could be attainable with this material, and otherwise determine the characteristics present under applied oxidative potentials. Stability of the material under this type of loading would also be of interest. However, exploration of the Ni-coated FTO sample under oxidative scans was found to be highly limited. As demonstrated in Figure 50, a large one-time oxidation event occurs for the FTO supported film. The example shows two sample runs with an oxidation peak at 0.36 V (*vs.* Ag/AgCl) with a current density of 1.74 mA cm^{-2}, and at 0.68 V with 5.66 mA cm^{-2}. After this event, the current drops to ~1.0 mA cm^{-2}, a value corresponding to the electrochemical behavior of an FTO electrode. Visual observations of the FTO glass after the oxidation event indicated loss of the film material and subsequent reduction CVs are similar to that of the bare FTO before coating. These observations suggest that application of a positive/oxidative potential led to Ni-based film destabilization or oxidation.

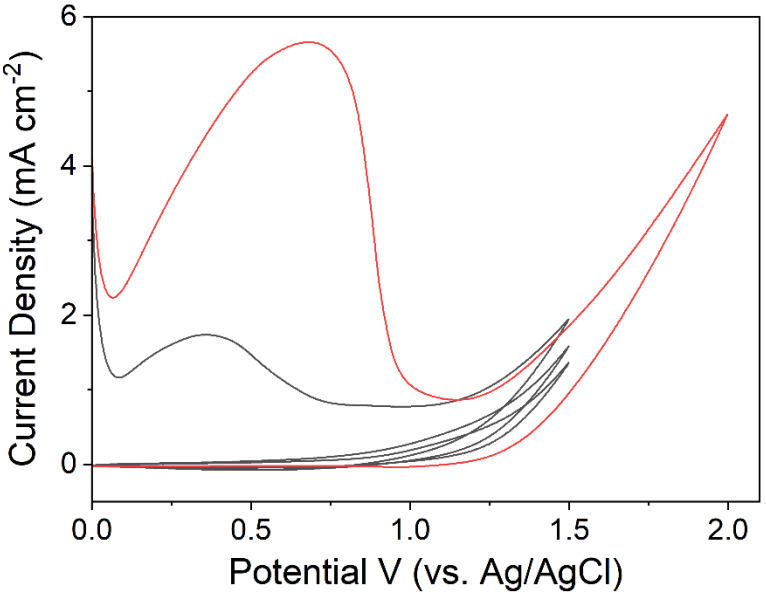

Figure 50: Cyclic voltammetry under anodic potentials (*vs.* Ag/AgCl) of two samples of a Ni4N-coated FTO glass tested from 0 to 1.5 V (black) and 0 to 2.0 V (red).

4.3.8 – Ni4N Potential Required for Coating FTO Glass

For further investigation into what potential was required to coat the FTO glass using Ni4N, a brief set of tests was conducted using CPE as the analysis method with a summary provided in Table 6. It was noted early on in experimentation that the typical coating process with Ni4N complex at -1.3 V over 1 hr included a steep increase of current from the initial state and gradually levelled off at a significantly higher current. This increase of current has been seen in all coating trials, levelling broadly in the region of 1.5-2.0 mA cm^{-2}. With this concept that an increase in sustained current with a set potential correlate to successful coatings, CPE was performed at five-minute intervals at lower specified potentials was done to observe this increase. The five-minute time

interval was considered to be a long enough duration to indicate substantive changes. The general intention of this analysis is not purely quantitative, but to gain some insight into the general trends or patterns that might be observed, focusing on percent current change and total current. The initial current at -1.00 V (*vs.* Ag/AgCl) is low at 29.4 μA cm^{-2}, with little change over the five-minute duration (Table 6). However, at -1.05 V this current increases by 19.6% over the timeframe. Lowering the voltage from here shows a continuous increase in initial current as well as increases over five minutes, to a minimum of -0.70 V. At this point, the voltage was reset to -1.05 V, with a notably higher initial current than previous (152 vs 44 μA cm^{-2}). Voltage was incrementally increased from here with a final voltage of -1.30 V held over 1 h to parallel the typical film formation process and compare relative end currents, approximately 1.5 mA cm^{-2} versus 1.75 mA cm^{-2} observed in Figure 47. With these results, it was theorized that the FTO glass surface must be conditioned at a relatively higher potential (-1.05 V), where the initial electrodeposition of Ni4N onto the surface. This initial formation increases the capability for further formations of the heterogeneous species, which is reflected as increases in current as well as reducing the minimum voltage required.[28] It is proposed that this relates to a minimum onset of electrolysis with water, which provides the source of oxygen and hydroxide in the formation of $NiO/Ni(OH)_2$ layers. As an additional note, a brief test for the minimum potential viable with for detectable hydrogen production yielded 5.9 μmol at -1.0 V (*vs.* Ag/AgCl), and 15.9 μmol at -1.1 V using CPE over 3600 s.

Table 6: Sequential testing of a Ni4N-coated FTO glass in 0.1 M KCl aqueous solution at varied cathodic potentials (*vs.* Ag/AgCl) held for 5 min, with detected current output at the stated potentials, and the current change after 5 min.

Potential (V)	Initial Current ($\mu A\ cm^{-2}$)	Percent change (End Current)	End Current ($\mu A\ cm^{-2}$)
-1.00	29.4	1.4%	29.8
-1.05	44.1	19.6%	52.8
-1.00	45.5	15.8%	52.7
-0.95	51	15.3%	58.8
-0.90	59.2	8.3%	64.1
-0.85	69.6	5.5%	73.4
-0.80	76.3	4.4%	79.6
-0.75	76.4	6.2%	81.2
-0.70	82.7	1.6%	84.0
-1.05	152.0	-4.9%	144.5
-1.10	189.6	0.0%	189.6
-1.15	278.5	7.1%	298.4
-1.20	453.2	11.4%	504.7
-1.23	680.1	6.5%	724.5
-1.25	880.7	3.6%	912.0
-1.27	1100.9	-1.4%	1082.9
-1.30 (1hr)	1374.9	8.9%	1497.1

4.3.9 – Ni4N Concentration Optimization and H_2 Production Results

Experiments were also performed to determine the effect of Ni4N complex concentration on film formation with the specific focus on the impact of this on hydrogen production from the film. Concentrations of 0.1, 0.3, 0.5, and 1.0 mM were chosen to be tested. Tests with 0.5 mM appeared to have consistently the highest results. Films prepared from 0.5 mM concentration generated H_2 ranging from 44 to 49 µmol. For comparison, films prepared from solution with 1.0 mM Ni4N showed decreased performance typically yielding around 35 to 37 µmol of H_2. Two tests using solutions with 0.3 mM Ni4N showed results with a broader range of 35.0 µmol and 43.2 µmol of H_2. A single test with 0.1 mM solution of Ni4N produced 25.4 µmol of H_2, notably lower than the other results. While exploratory, the general consistency of the other results in the 40+ µmol range gave enough evidence to settle on 0.5 mM as the optimal concentration in regard to preparing the most effective Ni-based films for hydrogen production.

Using the films prepared from initial concentrations of 0.5 mM, 0.3 mM, and 0.1 mM of Ni4N, H_2 production results are summarized in Table 7. An average of 46.7 µmol was produced with the 0.5 mM samples, with the inclusion of 0.3 and 0.1 mM samples bringing the average to 40.5 µmol. Faradaic efficiency for the 0.5 mM trials indicates an average FE of 95.8% and an error of ± 6.2% (Table 7). The inclusion of the 0.3 and 0.1 mM concentrations gave FE > 90% and brings the average FE to 96.6% and an error of ± 4.5%. Two 5-hour experiments are also included, using two different initial Ni4N concentrations. H_2 detected for the 1.9 mM was 114.0 µmol and 0.5 mM with 131.2 µmol, with a Faradaic efficiency of 41.3 % and 57.1 % respectively, calculated by Equation 6. This

lower Faradaic efficiency is suspected to be due to potential cell leakage of H_2 gas over the longer duration, which combined with a higher accumulation of H_2 present in the headspace, increases the total rate of leakage. The use of a single cell compartment may also impact results as potential products created at the anode/counter electrode, such as oxygen, is not separate from hydrogen output. The change of pH of the solution by depletion of H_2 may also be of concern, although this was not explored here. CPE current generally increased over this 5-hour duration, increasing from ~1.1 mA cm^{-2} to ~1.5 mA cm^{-2}. Hydrogen calibration details are provided in the experimental details section.

Table 7: Comparison of final Ni4N-coated FTO samples for gaseous H_2 production, showing values for Initial Ni4N concentrations for coating, Time (seconds), H_2 area (as detected by GC-TCD), H_2 in µmol, current area (A·seconds), Faradaic efficiency (%). The lower two rows indicate the average results for 0.5 mM and 0.5, 0.3, 0.1 mM tests.

Initial Ni4N Concentrations	Time (seconds)	H_2 Area (uV·s)	H_2 (µmol)	Current Area (A·seconds)	Faradaic Efficiency (%)
0.5 mM	3600	1206.1	44.4	9.30	92.3
0.5 mM	3600	1325.6	48.9	9.16	103.0
0.5 mM	3600	1271.9	46.9	9.83	92.1
0.3 mM	3600	1168.5	43.0	8.47	98.0
0.3 mM	3600	946.5	34.8	6.70	100.3
0.1 mM	3600	686.4	25.1	5.15	94.1
5 hr 1.9 mM	18000	3082.4	114.1	53.30	41.3
5 hr 0.5 mM	18000	3546.9	131.4	44.45	57.1
0 Area (BG)	3600	0	-0.4	--	--
Avg. 0.5 mM	3600	1267.9	46.7	9.43	95.8 (6.2) %
Avg. 0.5-0.1 mM	3600	--	40.5	--	96.6 (4.5) %

4.3.10 – Linear Sweep Voltammetry Testing with H_2SO_4

Noting that the onset and overpotentials are less than clear for the Ni4N-derived film on FTO in 0.1 M KCl aqueous solution, an alternate investigation was conducted following the methodology of Pumera et al.[66] This would allow a clear observation of onset with HER by reduction at the electrode with measurements of overpotentials at given current densities. Additionally, it would allow calculation of a Tafel slope that would provide a comparison point versus literature. A Ni4N-coated FTO was placed in 0.5 M H_2SO_4, performing an LSV at 2 mV s^{-1} scan rate (*vs.* Ag/AgCl) and comparing performance to that of a platinum working electrode. The general approach is to provide an ideal proton-rich source and compare against a known high performance HER catalyst. In Figure 51, a Pt electrode showed an onset at approximately -0.208 V (*vs.* Ag/AgCl), or 11 mV (*vs.* RHE), which is similar to reported values of 10 mV (*vs.* RHE).[31] Onset voltage values defined by set current density values were -0.249 V (*vs.* Ag/AgCl) for 0.1 mA cm^{-2}, and -0.278 V at 1.0 mA cm^{-2}. With the Ni4N-coated FTO sample, the onset potential was -0.265 V (*vs.* Ag/AgCl) or an approximate overpotential of 68 mV (*vs.* RHE). Again, the onset voltages needed to generate a set current value were measured to be 0.417 V (*vs.* Ag/AgCl) at 0.1 mA cm^{-2} (220 mV *vs.* RHE), and -0.542 V (*vs.* Ag/AgCl) at 1.0 mA cm^{-2} (345 mV *vs.* RHE). These values compared well with Majumder et al.*'s* work, with overpotential values of 168 mV (*vs.* RHE) for onset, 210 mV at 0.1 mA cm^{-2} and 440 mV at 1.0 mA cm^{-2}.[28] A comparison of the onset and overpotentials at 0.1 mA cm^{-2} and 1.0 mA cm^{-2} can be found in Table 8.

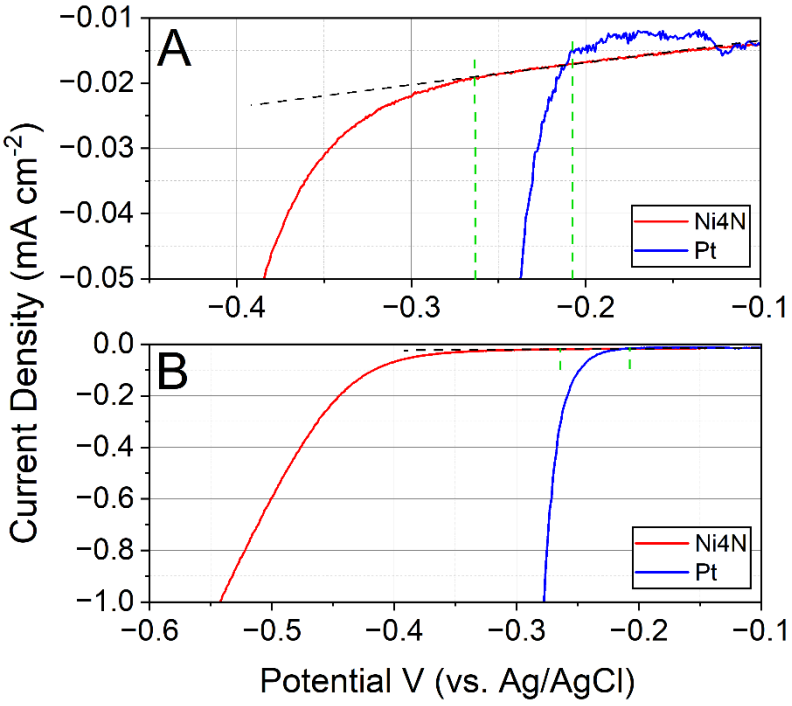

Figure 51: LSV comparison under cathodic potentials (*vs.* Ag/AgCl) of Ni4N-coated FTO glass (red) and a bare platinum wire (blue) as the working electrode in 0.5 M H_2SO_4 at a scan rate of 2 mV s^{-1}. (A) expands from -0.01 to -0.05 mA cm^{-2}, (B) expands from 0 to -1.0 mA cm^{-2}.

Table 8: Comparison of LSV overpotentials (*vs.* RHE) of Ni4N, Pt Wire, and Cu_2L as reference, at onset, 0.1 mA cm^{-2} and 1.0 mA cm^{-2}. [28]

	Ni4N	Pt Wire	Cu_2L
Onset	68 mV	11 mV	168 mV
0.1 mA cm^{-2}	220 mV	52 mV	210 mV
1.0 mA cm^{-2}	345 mV	81 mV	440 mV

A Tafel plot was constructed from the data acquired using 0.5 M H_2SO_4, in order to help isolate the kinetics of the Ni4N-derived film, as the exchange current density relates to the catalytic activity.[67] From the potentials of -184 mV to -247 mV (*vs.* RHE), the Tafel slope was found to be 94 mV dec^{-1} (Figure 52), as found with equation 11. More conventionally, this notes how much potential is required to induce one log unit worth of current change.

$$\frac{1\ V}{10.67\ dec} * \frac{1000\ mV}{1\ V} \quad (11)$$

A second sample for Ni4N with identical coating standards is included to correlate the detected slope along the linear region. This value of 94 mV dec^{-1} places it highly similar in rankings to such examples as methyllithium (102 mV dec^{-1}), tert-butyllithium (94 mV dec^{-1}), n-butyllithium (96 mV dec^{-1}) as lithium intercalation used in exfoliation of bulk MoS_2 – with Pt/C as superior at reported values of 30, 35 mV dec^{-1}.[66,67] The high correlation with these known HER catalysts under the same test conditions further substantiates performance. Figure 53 additionally shows the Tafel plot for a platinum wire WE, calculating to 32 mV dec^{-1}, which is comparable to the reference slope of 30, 35 mV dec^{-1} for platinum.[66,67]

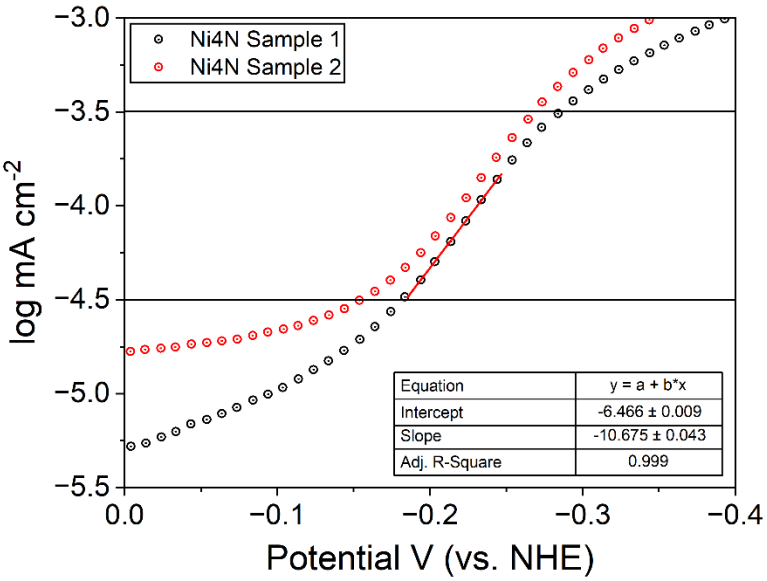

Figure 52: Tafel plot of two identical Ni4N-coated FTO samples as the WE with LSV performed under cathodic potentials at 2 mV s^{-1} in 0.5 M H_2SO_4. Ni4N Sample 1 (black) is the main sample for comparison, with Ni4N Sample 2 (red) as additional reference for the slope as detected. Horizontal lines included at -3.5 and -4.5 log mA cm^{-2} are present for ease of comparison.

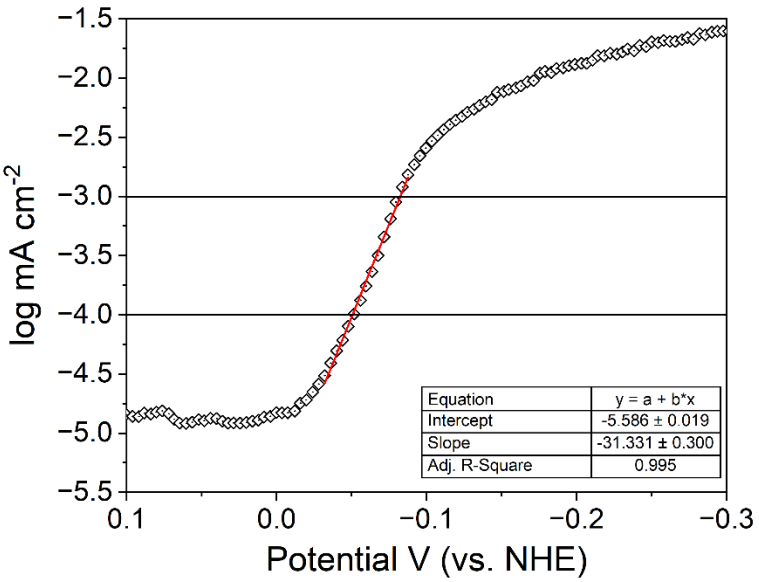

Figure 53: Tafel plot of a platinum wire as the WE with LSV performed at 2 mV s^{-1} in 0.5 M H_2SO_4.

4.3.11 – Ni4N Discussion

In this section for the creation of a NiO-based film, it should be noted that there are several NiO-based films or heterogeneous materials present in recent literature.[68–71] These are all capable electrocatalysts with effective properties, particularly in regard to Tafel slope and overpotential, with many more stated in literature.[20] The following examples are not exhaustive, but provide a sample comparison (Table 9).

Table 9: Comparison of selected NiO-type heterogeneous catalysts for HER.

Name	Solvent	Tafel Slope (mV dec^{-1})	Overpotential (*vs.* RHE)	Synthesis
NiO/Ni-CNT[68]	1.0 M KOH	82	<100 mV 10 mA cm^{-2}	Low temperature hydrolysis of Ni salts with NiOH, CNT, followed by low pressure annealing at 300 °C in Argon.
NiO_x-SC/FTO[69]	0.5 M KOH	89	350 mV, 10 mA cm^{-2}	1:1 water/ethanol mix of 0.1 M $NiCl_2 \cdot 6H_2O$, interval spray on preheated FTO to 250 °C.
NiO/Ni[70]	1.0 M Phosphate	115	88 mV 10 mA cm^{-2}	Ni-MOF precursor, stepwise calcination in Argon.
Ni/Gd_2O_3/NiO[71]	1.0 M KOH	45	190 mV 10 mA cm^{-2}	Electrospinning Nickel Acetate/Gadolinium Nitrate solution, 25 kV, 2 mL/h, calcined at 600 °C under air/argon for 3 hr.
This work (Ni4N)	Water + 0.1 M KCl (0.5 M H_2SO_4)	94	345 mV 1 mA cm^{-2}	Electrodeposition with 0.5 mM Ni4N solution at -1.3 V (*vs.* Ag/AgCl) over 1 hr.

Note that the current density between this work and literature has some disparity, however this is also observed using platinum as the WE. The tested overpotential for

platinum in 0.5 M H_2SO_4 requires 170 mV (*vs.* RHE) for 10 mA cm^{-2}, 250 mV for 20 mA cm^{-2}, with a literature example requiring ~40 mV, ~70 mV for the same current densities (Appendix, Figure 77).[70] This suggests that the difference may relate to the electrochemical cell parameters as platinum should provide an optimal comparison.

Notable with the above references in Table 9, and likewise with many other HER catalysts, the primary solvent typically used for testing is either 0.5/1.0 M KOH or 0.5/1.0 M H_2SO_4.[20,72] These solvents provide an ideal known environment for testing the catalytic performance of their prepared species, particularly in relation to the Nernst equation and pH calculations and provide valuable characterization conditions. However, it is fairly uncommon that they are reported under more benign or neutral conditions, such pH 7 salt solutions or near pH 7 buffer solutions. The above reference (Table 9) with NiO/Ni performs their characterization under these conditions with 1.0 M phosphate buffer.[70] This neutral pH is more likely to reflect real world conditions as used in bulk electrolysis. The other factor is ease of synthesis with cost of materials. Some syntheses require more exotic materials, such as carbon nanotubes (CNT) or metal organic frameworks (MOFs) or require highly specific conditions such as high heat (250 °C to 600 °C), and under argon. It's possible these considerations can be streamlined or otherwise minimized, but they remain overall factors in greater scaling.

With this work, the most immediate positive aspect is that this catalyst can work under the simplest and perhaps desirable conditions. Ni-based film formation was carried out in water and KCl, and the process of generating hydrogen carried out under the same conditions. Water is generally the most sought-after substrate due to the environmental

impact, its ready availability and low cost, and KCl is similar in terms of cost and safety. Not needing an additional substrate such as a buffer to help protonation is also ideal. The most ideal conditions for exploitation may be ocean water already providing an ample electrolyte, with the idea that this can be diluted if necessary. The material required is not necessarily restricted to FTO glass with the limited observations towards this aspect – coating onto a graphite rod for example and producing similar levels of hydrogen. Relatively long-term stability in the same solution appears to be productive for at least up to 5 h, if not eventually becoming inert due to hydrogen expulsion and the possibility for the pH of the solution becoming too basic.

The synthesis of the complex is very simple, with the mixture of the two reagents $NiCl_2 \cdot 6H_2O$ and 1,2-bis(3-aminopropylamino)ethane in equal molar amounts in 15 mL of 95% ethanol, and a low application of heat for 2 h. Upscaling of the synthesis would be relatively simple with minimal in-depth chemical knowledge needed or training. In terms of potential negative factors, there are aspects that give some cause for concern, or at least have a need to address for full optimization of the complex. A consideration to factor would be stability of the film under anodic potentials. It was demonstrated that the films can be readily oxidized and destroyed with an applied potential of ~0.5 V or above (*vs.* Ag/AgCl).

In more general aspects for future work, optimization of the coating procedure as well as determining an optimal electrode for electrodeposition of the complex. It has been shown that this Ni4N complex can form films that have a similar degree of hydrogen production while attached to a graphite rod. Whether or not it is more functional under

this alternate electrode is a pertinent question, along with simpler, cheaper forms such as solid steel or copper plates, meshes to take advantage of surface area exposure, or other formats of a platform. Annealing may improve the properties of this film, noted to dehydrate $Ni(OH)_2$ substituents to NiO, which may improve the overall electrical conductivity.[73] Some other notable limitations for the exploration performed here are the impact of similar salts or other pH neutral electrolytes. The impacts of buffers in particular due to their noted ability to reduce the overpotential of a particular electrocatalyst (e.g. 180 mV lowered to 30 mV vs RHE).[39] However, it is also possible for a buffer to negatively affect the overpotential requirements, increasing it >40 mV as an example.[74] These various factors for development should be ranked in terms of maximum possible impact – such as better overall efficiency, onset/overpotentials, cost, simplification, environmental impact and so on.

In concluding this chapter, this has discussed creating a thin-film $NiO/Ni(OH)_2$ catalyst that performs HER efficiently in a neutral pH solution which requires only a simple mix of 0.1 KCl and water, without need of an additional proton donor source. The hydrogen output is comparable with the primary literature reference operating under similar conditions, with the chosen optimal concentration providing ~47 µmol H_2 with a Faradaic efficiency of ~96% versus the references 21.6 µmol and FE of ~92%.[28] Longer-term stability for hydrogen production over 5 h yielded 131.2 µmol, indicating a moderate longevity to consistent output from a single solution. Primary considerations to be addressed is assuring stability of the coating, and refining the coating process to maximize hydrogen production.

4.4 – Cu4N

An examination of the application of an analogous Cu complex, dibromo-(N1',N3-ethane-1,2-diyldipropane-1,3-diamine)-copper(II) (Cu4N), was stimulated by the performance of the complex Ni4N. In this case, the investigations are of a more limited scale to serve as a point of comparison. A brief overview of the electrochemical characteristics of the species is carried out here. With the likelihood that Cu4N would likely electrodeposit and form films on the working electrode similarly to Cu3N2O and Ni4N, testing began with using a blank FTO glass with 0.1 M KCl with an Ag/AgCl reference electrode. Initial CV response from the blank FTO with 0.5 mM Cu4N presents a minor reduction event at -0.53 V (*vs.* Ag/AgCl) with 0.07 mA cm^{-2}, and an associated undefined oxidation event at -0.31 V at a current of ~0.14 mA cm^{-2} (Figure 54). These peaks would be associated with the large peaks seen in the Cu4N-derived films on FTO that will be detailed below. Comparing against a blank FTO without complex present generally onsets reduction at ~-1.3 V at 0.02 mA cm^{-2}, with a current of 0.24 mA cm^{-2} at -1.5 V – approximately 8 times higher current when Cu4N is present in solution. After film formation, a clear reduction peak is observed at -0.78 V (*vs.* Ag/AgCl) with a current of 1.53 mA cm^{-2}. The oxidation peak linked with this reduction appears at -0.23V with current density of 0.84 mA cm^{-2}, although this remains broad and not well-defined. Continuing in the cathodic directeion another reduction appears with an onsetsat -1.07 V and 0.26 mA cm^{-2}. The current at -1.5 V remains largely the same as the initial state, reaching ~2.1 mA cm^{-2}. The Cu4N-derived film on FTO electrode was removed, dried,

dipped in DI water for 2 min to remove residual KCl surface deposition, and placed in fresh 0.1 M KCl solution further CVs conducted.

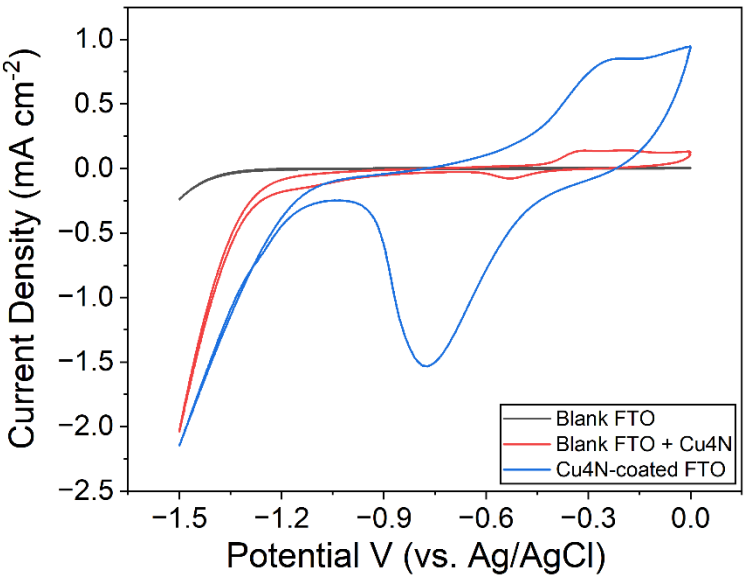

Figure 54: Cyclic voltammetry under cathodic potentials (*vs.* Ag/AgCl) for a blank FTO without complex (black), blank FTO with 0.5 mM Cu4N present in solution (red), the Cu4N-coated FTO (blue).

CPE was carried out for electrodeposition of Cu4N onto the FTO glass, in 0.1 M KCl at -1.3 V (*vs.* Ag/AgCl) for 3600 s. The current increase is surprisingly similar to what was observed during the analogous process with Ni4N (Figure 55). However, in the case of Cu4N the current density did not appear to plateau as Ni4N does. At the end of the CPE run with Cu4N, the current density was 1.26 mA cm^{-2} compared to 1.74 mA cm^{-2} in the film formation with Ni4N. After the coating process was complete, hydrogen production with the film was tested.

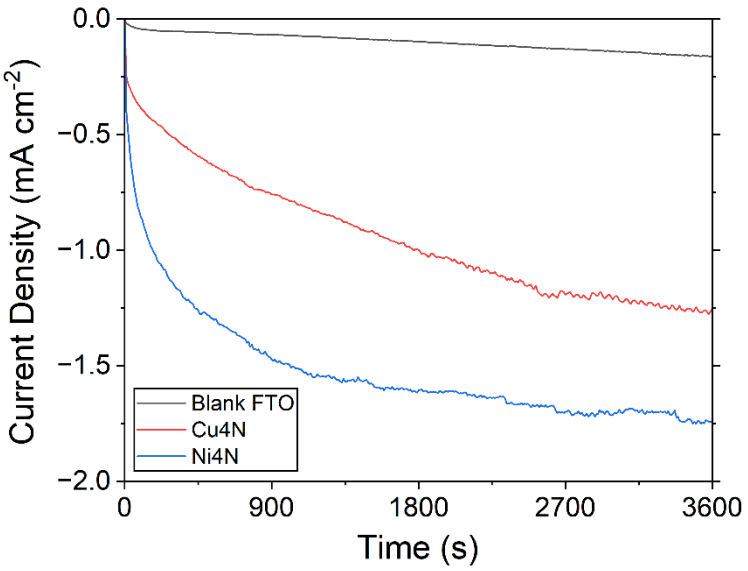

Figure 55: CPE results for the electrodeposition process of an FTO plate in 0.1 M KCl alone (black), 0.5 mM Cu4N (red), and 0.5 mM Ni4N (blue) held at -1.3 V (*vs.* Ag/AgCl) over 3600 s.

Hydrogen production testing by CPE followed the same procedure as with Ni4N, applying -1.2 V (*vs.* Ag/AgCl) over 3600 s, with hydrogen results detected by GC-TCD measurement. Cu4N-coated FTO yielded a modest 19.7 µmol vs. 46.7 µmol for Ni4N, noting the significant difference clearly in favour for the Ni4N-derived films. Cyclic voltammetry was additionally performed before hydrogen production by CPE (Pre-CPE) and comparing to after hydrogen production (Post-CPE) (Figure 56). For Cu4N-derived films, there appears to be no notable difference between Pre-CPE and Post-CPE CVs. With Ni4N-derived films, a minor decrease in current strength is observed, notably at -1.5 V from ~4.1 mA cm^{-2} to 3.6 mA cm^{-2}. This potentially may indicate that despite a lower hydrogen output, Cu4N-derived films may be more stable than Ni4N-derived films during HER with water, but this would need to be further investigated to verify.

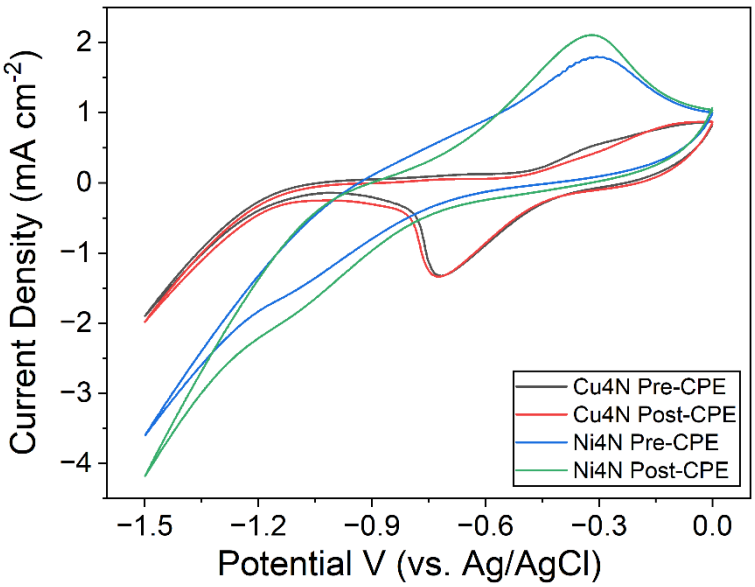

Figure 56: Cyclic voltammetry under cathodic potentials (*vs.* Ag/AgCl) comparison of Cu4N-coated FTO pre-CPE (black), post-CPE (red) and of a Ni4N-coated FTO species, pre-CPE (blue) and post-CPE (green).

4.5 – Crystal Structure for Ni4N, Cu4N Complexes

4.5.1 – Ni4N, Cu4N Structure

Ni4N is arranged in an octahedral configuration with the open-ended tetradentate ligand forming a relatively planar open-ended macrocycle around the Ni(II) atom, with two chloride atoms on opposing sides (Figure 57). No solvent molecules or other molecules aside from the main complex is observed in the crystal structure. Bond angles for nitrogen atoms are approximately 90 degrees, with N(1)-Ni(1)-N(2) as 92.39(11)°, N(1)-Ni(1)-N(4) as 93.18(12)° (Table 11). Total bond angles for nitrogens around the nickel

atom amount to 359.98 degrees, with this calculated value being exact to that of Ni5N-3,2,3, highlighting to the planarity of both complexes. Opposing nitrogens reveal little distortion of the ligand, with N(1)-Ni(1)-N(3) at 175.61(11)°, N(2)-Ni(1)-N(4) at 174.37(12)° (~1.3 degree difference). Chloride atoms bond close to 90 degree intervals, with N(1)-Ni(1)-Cl(1) at 89.60(8)°, Cl(1)-Ni(1)-Cl(2). Bond lengths between central atoms are highly regular, with Ni(1)-N(1-4) lengths ranging 2.075-2.099 Å. Ni-Cl bond lengths mildly deviate, with Ni(1)-Cl(1) as 2.4680(10) Å, and Ni(1)-Cl(2) as 2.5198(9) Å. Further crystal sample data is presented in Table 10.

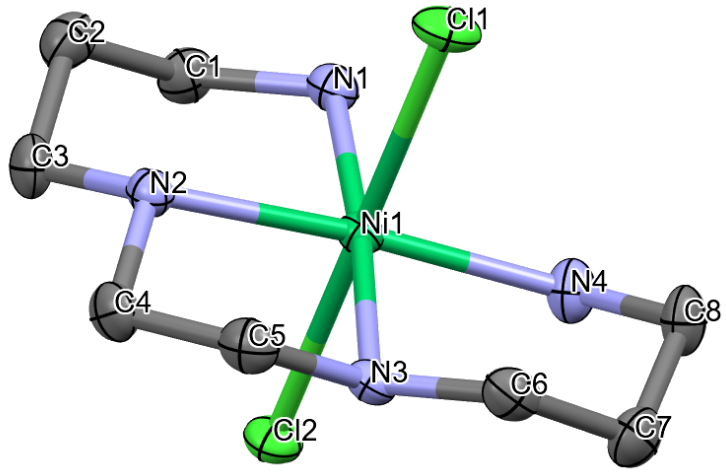

Figure 57: Structural representation of Dichloro-(N1',N3-ethane-1,2-diyldipropane-1,3-diamine)-nickel(II) (Ni4N), obtained from single crystal X-ray analysis. Hydrogen atoms have been excluded for clarity.

The structure of Cu4N is reported in the Cambridge database with the identified 'AYIZEO'. Connectivity was estabilised by crystallography to confirm the identity as

dibromo-(N1',N3-ethane-1,2-diyldipropane-1,3-diamine)-copper(II), with the structure not completely solved (Figure 58). As seen in Figure 59, the structure presents with as a bromide bridged dinuclear [(N1',N3-ethane-1,2-diyldipropane-1,3-diamine)Cu]$_2$ cation with an additional bromide anion that is beyond bonding distance. The bond length between bromide demonstrated as attached and the nearest without bonding is 2.875(3) Å and 3.196(4) Å respectively (Table 12). An ancillary perchlorate and acetonitrile molecule additionally is observed as part of the overall crystal structure. It forms a Jahn-Teller 'distorted CdI_2 type' structure, layering in a 4+2 coordination where four short bond lengths of 2.4143 Å and two longer bond lengths of 3.1478 Å.[75]

With the above consideration, Cu4N is arranged in an distorted configuration, with the ligand forming a relatively planar open-ended tetradentate ligand around the Cu(II) atom, with two bromide atoms on opposing sides. Bond angles for the Br-Cu-N are approximately 90 degrees, with N(5)-Cu(3)-Br(1) (89.5(5)°) and N(6)-Cu(3)-Br(1) (87.6(5)°) (Table 12). Bond angles for Cu-N bonds are approximately 90 degrees, with choice bonds highlighted as N(5)-Cu(3)-N(6) (91.7(7)°) and N(5)-Cu(3)-N(8) (86.0(7)°). Total bond angles for nitrogen atoms coordinated around the copper atom amount to 359.7 degrees, correlating to a high degree of planarity. Opposing nitrogens reveal the mild degree of flexing the ligand experiences to one side of the plane, with N(5)-Cu(3)-N(7) (170.9(7)°) and N(6)-Cu(3)-N(8) (177.2(8)°) (~7.2 degrees difference). At a larger scale the bonded internal bromide distorts slightly to the open-ended side of the ligand. Interestingly, the ligands as observed also align as a pair, effectively mirroring each other. This greater structural behaviour is not observed in the later Ni4N crystal structure. The proposed

reason is the larger bromide atom is sterically inclined to the open, less-conflicting side of the ligand as opposed to chloride in Ni4N.

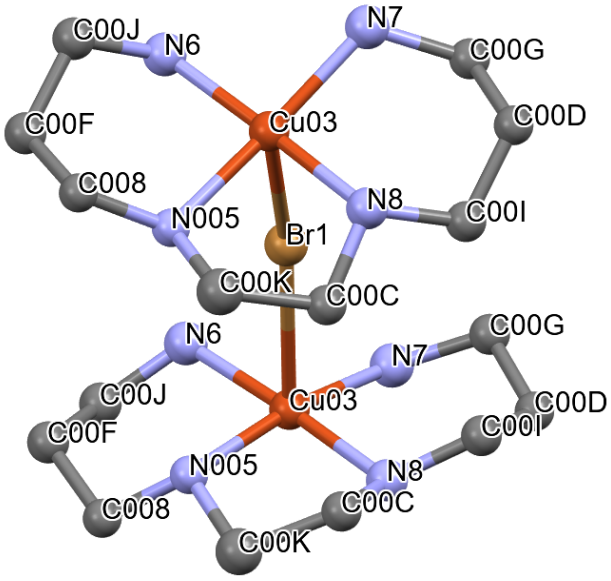

Figure 58: Structural representation of Dibromo-(N1',N3-ethane-1,2-diyldipropane-1,3-diamine)-copper(II) (Cu4N), obtained from single crystal X-ray analysis. One perchlorate molecule, one acetonitrile molecule, one bromide atom and hydrogen atoms have been excluded for clarity.

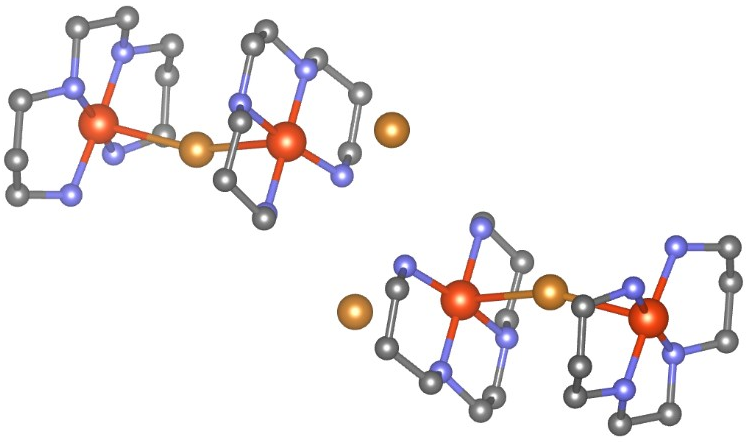

Figure 59: Alternate structural representation of Dibromo-(N1',N3-ethane-1,2-diyldipropane-1,3-diamine)-copper(II) (Cu4N), highlighting position of bromide relative to remainder of complex.

4.5.2 – Crystal Sample Data and Select Bond Angles, Bond Lengths

Table 10: Crystal sample data for Ni4N, Cu4N. Cu4N is noted as lower quality.

	Ni4N	Cu4N
Empirical Formula	$C_8H_{22}Cl_2N_4Ni$	$C_8H_{22}Br_2N_4CuClO_4$
Formula Weight ($g \cdot mol^{-1}$)	303.90	497.09
Crystal System	orthorhombic	monoclinic
Space group	P 2_1 2_1 2_1	P $2_1/m$
a (Å)	6.6004(3)	9.2508(8)
b (Å)	8.4134(4)	20.7134(17)
c (Å)	24.0478(8)	9.2706(10)
α (°)	90	90
β (°)	90	114.342(5)
γ (°)	90	90
V (Å^3)	1335.42(10)	1618.5(3)
Z	4	15
T (K)	200(2)	200(2)
ρ_{calcd} ($g \cdot cm^{-3}$)	1.512	2.268
μ (mm^{-1})	1.830	6.107
$2\vartheta_{max}$ (°)	57.820	56.602
Parameters	136	82
Total Reflections	3487	3533
R, wR^2 [$I_o \geq 2_\sigma(I_o)$]	0.0295, 0.0605	0.1505, 0.3692
S (Goodness of fit)	0.990	1.606

Table 11: Select bond lengths and bond angles from Ni4N crystal sample data.

Bond Lengths for Ni4N	
Atom-Atom	Length (Å)
Ni(1)-N(1)	2.075(3)
Ni(1)-N(2)	2.090(3)
Ni(1)-N(3)	2.099(3)
Ni(1)-N(4)	2.080(3)
Ni(1)-Cl(1)	2.4680(10)
Ni(1)-Cl(2)	2.5198(9)

Bond Angles for Ni4N	
Atom-Atom-Atom	Angle (˚)
N(1)-Ni(1)-N(2)	92.38(11)
N(1)-Ni(1)-N(3)	175.61(11)
N(1)-Ni(1)-N(4)	93.18(12)
N(2)-Ni(1)-N(4)	174.37(12)
N(1)-Ni(1)-Cl(1)	89.60(8)
Cl(1)-Ni(1)-Cl(2)	179.20(4)

Table 12: Select bond lengths and bond angles from Cu4N crystal sample data.

Bond Lengths for Cu4N	
Atom-Atom	Length (Å)
Cu(3)-N(5)	2.036(18)
Cu(3)-N(6)	2.027(17)
Cu(3)-N(7)	2.026(17)
Cu(3)-N(8)	1.993(16)
Cu(3)-Br(1)	2.875(3)
Cu(3)-Br(2)	3.196(4)

Bond Angles for Cu4N	
Atom-Atom-Atom	Angle (˚)
N(5)-Cu(3)-N(6)	91.7(7)
N(5)-Cu(3)-N(7)	170.9(7)
N(5)-Cu(3)-N(8)	86.0(7)
N(6)-Cu(3)-N(8)	177.2(8)
N(5)-Cu(3)-Br(1)	89.5(5)
N(6)-Cu(3)-Br(1)	87.6(5)

4.5.3 – FTIR for Cu3N2O, Ni4N and Cu4N

FTIR characterization was performed on Cu3N2O, Ni4N and Cu4N. Much like the criteria presented in Chapter 3, the macrocyclic complexes employed in this thesis are noted for their characteristic imine C=N stretches at 1650 cm^{-1}, for the pyridine ring at 1590 cm^{-1}, and absence of residual carbonyl C=O stretches at approximately 1700 cm^{-1} that were associated with unreacted 2,6-diacetylpyridine.[56] When ether linkages replace the amine linkages with NH moieties, no absorption is observed in the 3200-3300 cm^{-1} region of the spectra. Cu3N2O is compared to Mn3N2O in Figure 60 as a reference point. The overall aspects between these samples are very similar for nearly all features, with exceptions of a reduced absorbance at 1650 cm^{-1} (m, C=N). The similarity of all four samples at 1580 cm^{-1} could be represented by (m, C=C) for Mn3N2O and Cu3N2O, and (m, N-H) for Ni4N, Cu4N. Peaks at 2900-2800 cm^{-1} (m, C-H) match for all samples. The absorbance at 1450 cm^{-1} (m, C-H) is likewise shifted. Key features appear to be represented, with two peaks at 2926 cm^{-1} and 2876 cm^{-1} (m, C-H). As expected, these spectra did not show absorbances characteristic of the carbonyl starting materials at 1700

cm^{-1}. Other features align with Mn3N2O, with peaks at 1350 cm^{-1} (m, C-N, pyridine), 1250 cm^{-1} (m, C-O), and a broad, strong peak at ~1060 cm^{-1} (s, C-O and C-N). Examining Ni4N and Cu4N, notable absences relative to Cu3N2O, Mn3N2O occurs at 1650 cm^{-1} (m, N-H) and 1350 cm^{-1} (m, C-N, pyridine). Defined peaks are observed for Ni4N, Cu4N in the 3300-3200 cm^{-1} region (m, N-H). A significant reduction and variability in transmittance are also observed at 1100-900 cm^{-1}, while lacking a response at ~810 cm^{-1} which is present for Cu3N2O and Mn3N2O. With single crystal XRD obtained for Ni4N and Cu4N confirming their synthesis, and the high similarity between Mn3N2O and Cu3N2O samples, there is substantial evidence in the successful synthesis for these two latter complexes.

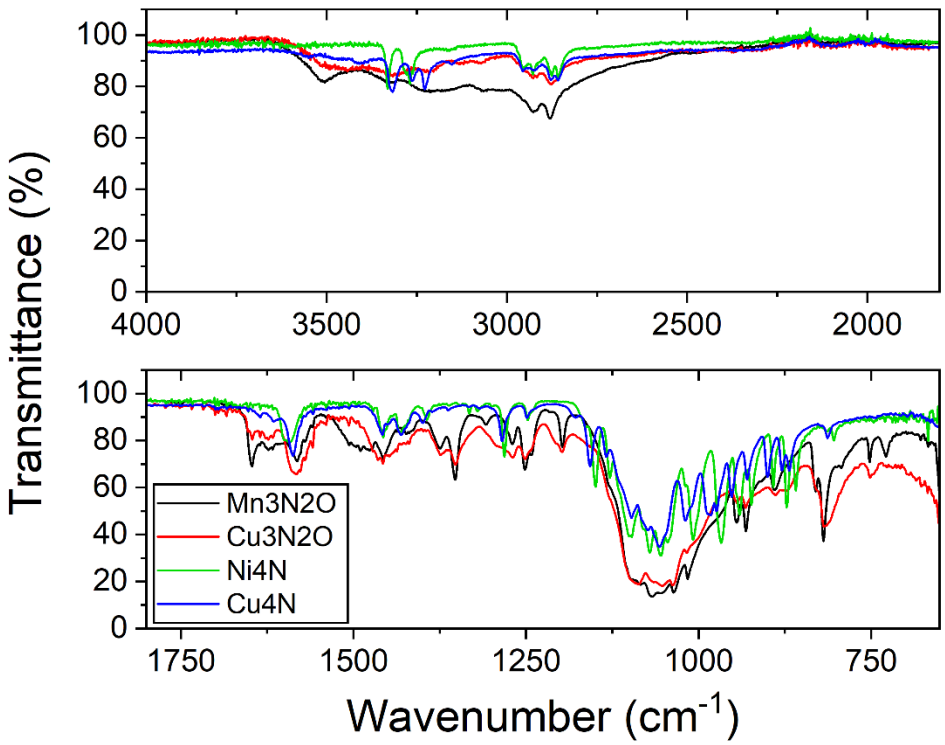

Figure 60: FTIR measurements of samples Cu3N2O, Cu4N, and Ni4N, with Mn3N2O provided as a comparison point.

4.6 – Surface Characterization of Ni4N-Coated FTO Glass

Surface characterization for the Ni4N-coated FTO samples were performed by Dr. Jurca's research group at the University of Central Florida. Key analysis numbers and initial graphs were provided by them, with further mild refinement, discussion points provided by myself. Scanning Electron Microscopy (SEM) imaging was performed on the FTO Ni4N-coated sample. The surface morphology is observed at three magnifications. As seen in Figure 61 (1 μm scale bar), the surface appears to form a regular pattern across the observed area. Irregularities in the layering are evenly dispersed on the top layer. At higher magnifications of 200 nm and 100 nm it would appear that the irregular features contribute significantly to distributed spherical formations approximately 100-300 nm in size, with non-uniform protrusions and channels across this layer. Atomic force microscopy (AFM) measurements of seven 1.0 μm x 1.0 μm sample areas indicated an average root mean-square surface roughness of 53.45 (5.63) nm, a mean roughness of 42.16 (3.62) nm, and a surface area per 1 μm_2 project area of 1.60 (0.19) μm_2 (Figure 62, Figure 63). EDX analysis of the Ni4N-coated FTO sample indicated the presence of C and N in a single strong peak in the lower 0 to 0.5 eV range, and peaks for nickel in the 0.9 and 7.5 eV range (Figure 64). Au presents as a result of gold dusting in preparation of EDX analysis, Sn from the FTO glass itself, and Cl as residual surface elements from solution electrolyte KCl during film creation.

Further characterization was carried out using X-ray photoelectron spectroscopy (XPS) to conduct an overall survey as well as high-resolution scans for specific elements

of the sample presented in Figure 65. Isolating to specific atoms, Figure 66 shows the spectrum for the Ni 2p spectrum. This spectrum was fit to the Ni $2p_{3/2}$ (855.84 eV) and Ni $2p_{1/2}$ (873.51 eV) peaks as fitted to a Ni(II) halide component at 855.75 eV. A second Ni(II) halide component at 857.02 eV fit the experimental values for $Ni^{\delta+}$ in the figure for Ni $2p_{3/2}$ (857.50 eV) and Ni $2p_{1/2}$ (857.02 eV). (Figure 66). The spectrum for Cl-Ni was fitted for components of Cl $2p_{3/2}$ (198.34 eV) and Cl $2p_{1/2}$ (200.04 eV) (Figure 67). The O 1s spectrum was fitted to two peaks at 531.18 and 532.11 eV, attributed to lattice oxygen and adsorbed oxygen, respectively (Figure 68). These associations directly align to our primary reference values for 531.1 eV and 532.4 eV, determined to be assigned to metal-oxygen and $(OH)_2$ species and of the chemisorbed water. Similarly, the N 1s spectrum displayed a peak with binding energy of 399.94 eV which was deconvoluted into two contributions that were assigned as C-NH-C (399.39 eV) and C-NH_2 (400.49 eV) (Figure 71). SnO_2 from the FTO glass itself is likewise fitted for Sn $3d_{3/2}$ (487.33 eV) and Sn $3d_{3/2}$ (495.73 eV) (Figure 70). Fitting for fluoride was below detection limits, as would be present from the FTO glass (Figure 71). Fitting for C 1s peak binding energy provides four data points, C-C (284.84 eV), C-N (285.40 eV), C-O-C (286.00 eV), and O-C=O (288.77 eV) (Figure 72). Accompanying in the figure is fitting for K $2p_{3/2}$ (293.77 eV) and K $2p_{1/2}$ (296.11 eV), notably with area counts per second per eV (Area CPS eV^{-1}) of 646.21 and 236.35 respectively (Figure 72). Compared to a Ni4N-coated FTO sample with KCl residue left on, the Area CPS eV^{-1} is ~34800 and ~15900 for K $2p_{3/2}$ and K $2p_{1/2}$ (Figure 73). Testing with Cl likewise follows this increase, with the prepared Ni4N-coated FTO sample indicating an Area CPS eV^{-1} of ~1070 and ~580 for Cl $2p_{3/2}/2p_{1/2}$ respectively, with the KCl residue

sample presenting ~20100 and ~9500 for the same fittings. The large difference in response (approximately 20 fold) between these two samples may suggest that the rinsing method used in removing excess surface salt is acceptable. Powder XRD measurements as tested on the prepared Ni4N-coated FTO glass displayed no diffraction peaks assignable to the deposited film (Figure 74). From these combined observations and data, the proposed film constitution is of an amorphous $Ni(OH)_2$ and NiO layer.

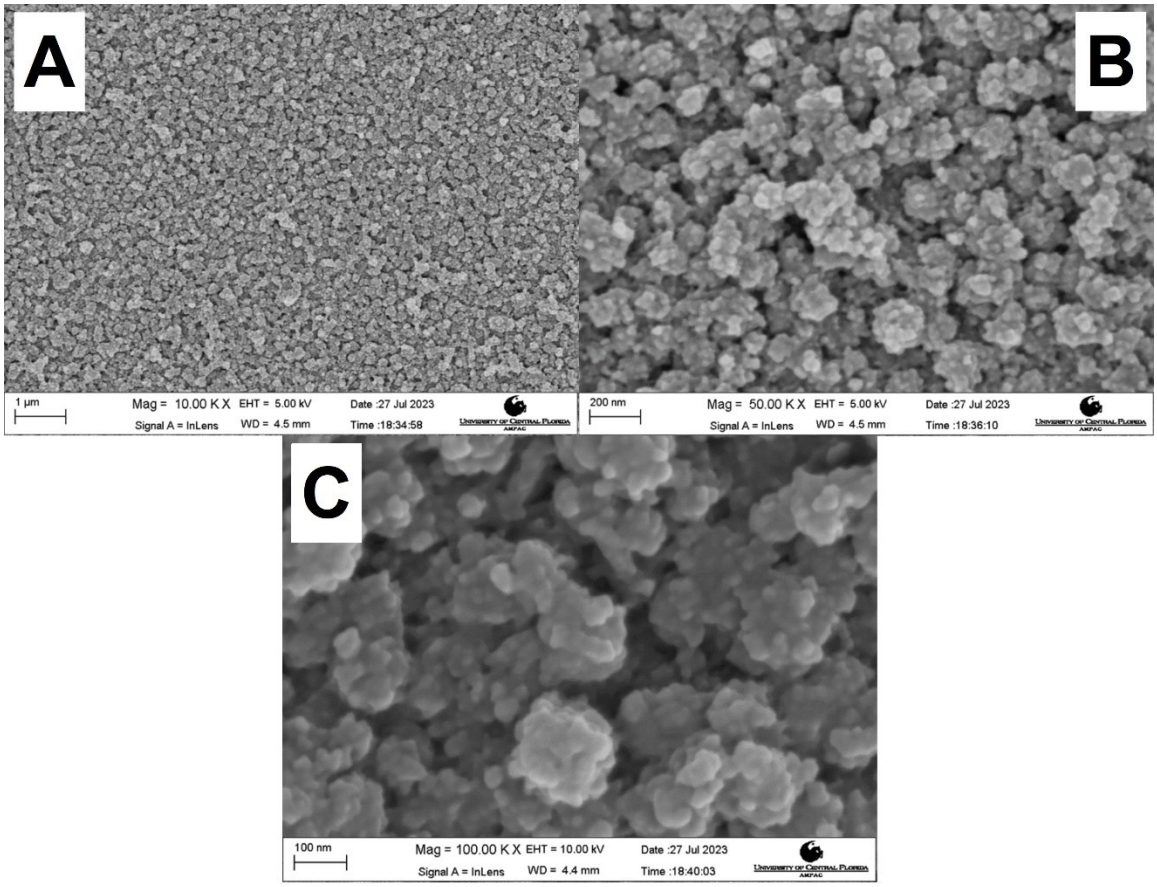

Figure 61: SEM-EDS surface morphology of a Ni4N-coated FTO species, scaling represented at 1 µm (A), 200 nm (B) and 100 nm (C).

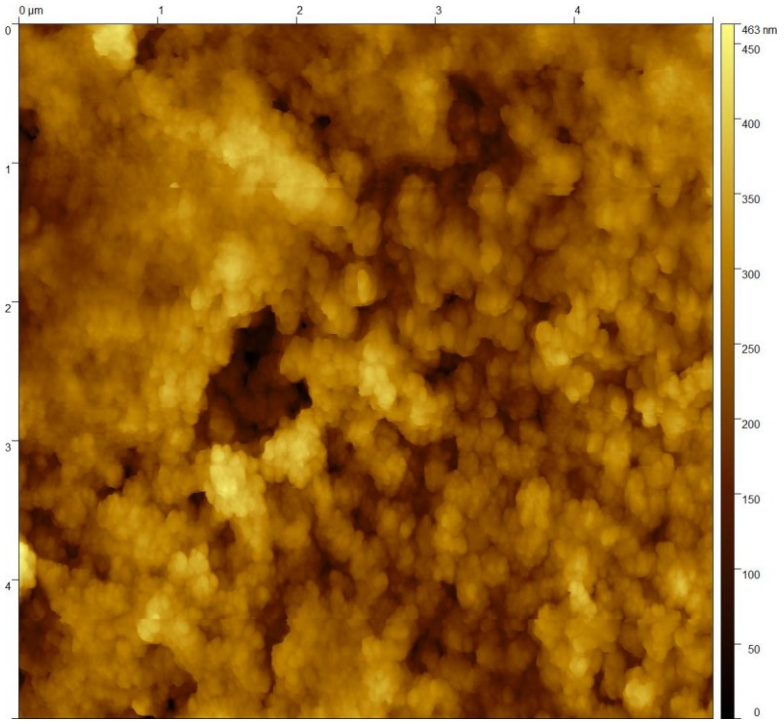

Figure 62: 2D representation of AFM surface scans for a Ni4N-coated FTO glass sample.

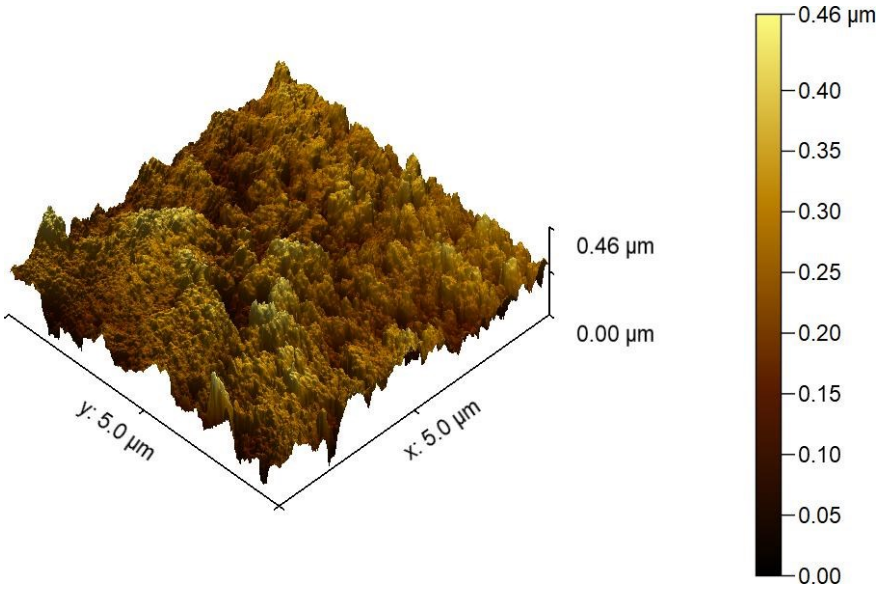

Figure 63: 3D representation of AFM surface scans for a Ni4N-coated FTO glass sample.

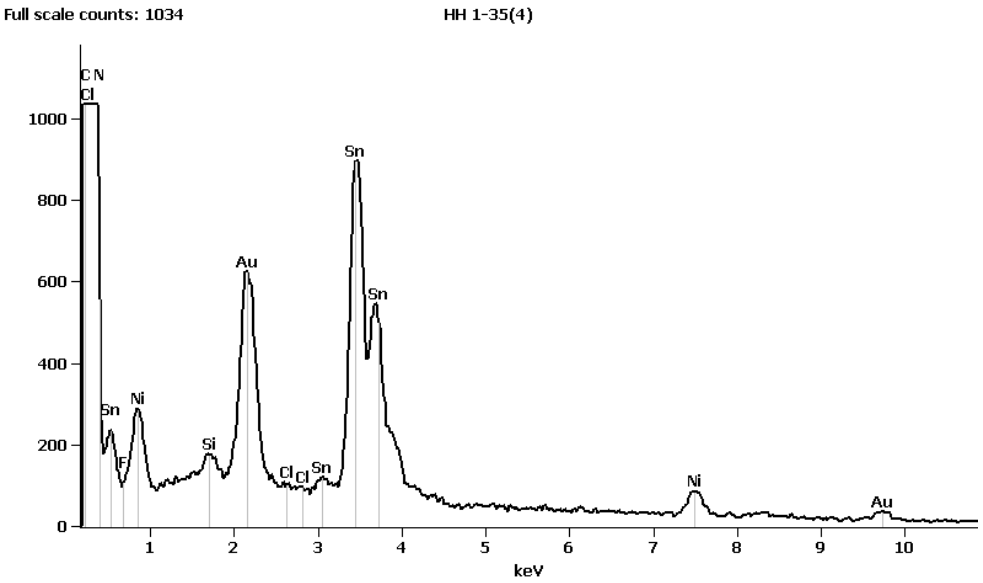

Figure 64: EDX spectrum of the Ni4N-coated FTO glass. Acc. Voltage: 20.0 kV, Take Off Angle: 35.0 deg.

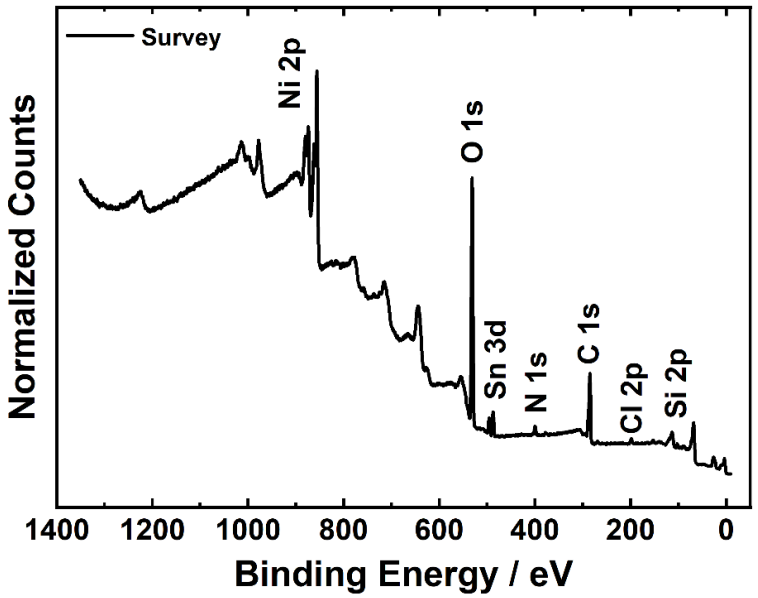

Figure 65: XPS survey for a Ni4N-coated FTO sample, with fitted experimental (black) and associated deconvoluted peaks.

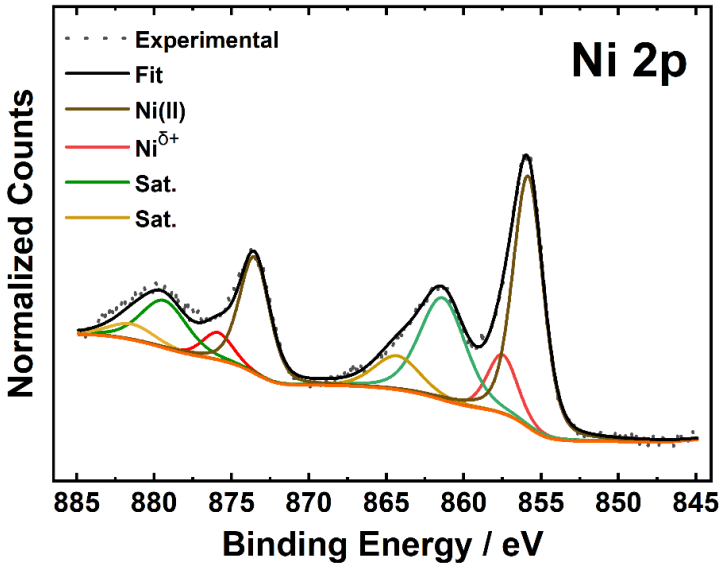

Figure 66: High-resolution XPS scan centered on the Ni 2p peaks for a Ni4N-coated FTO sample, with fitted experimental (black) and associated deconvoluted peaks.

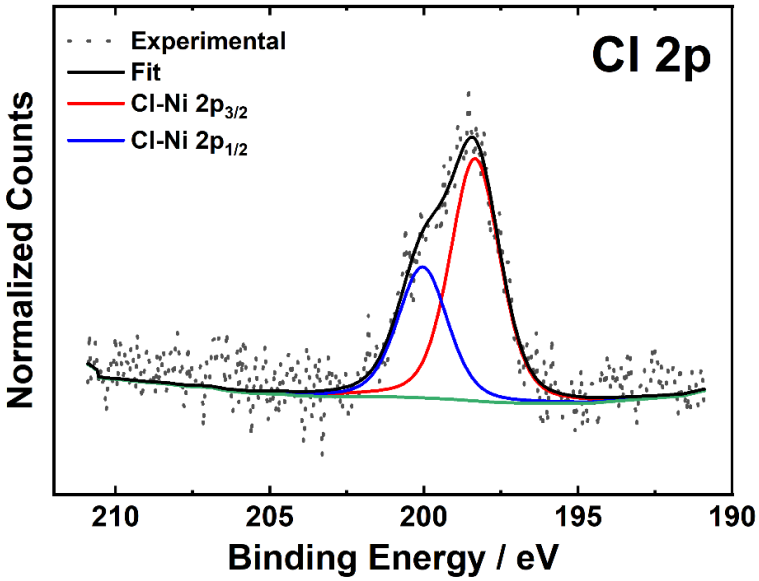

Figure 67: High-resolution XPS scan centered on the Cl 2p peaks for a Ni4N-coated FTO sample, with fitted experimental (black) and associated deconvoluted peaks.

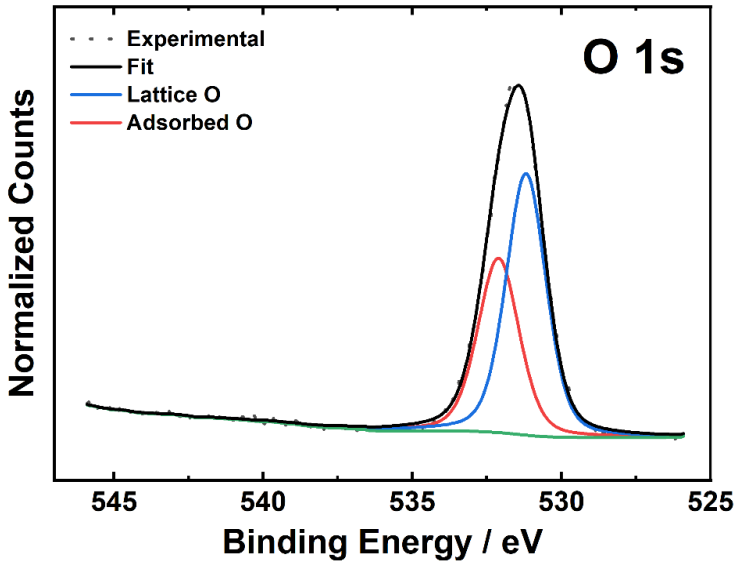

Figure 68: High-resolution XPS scan centered on the O 1s peaks for a Ni4N-coated FTO sample, with fitted experimental (black) and associated deconvoluted peaks.

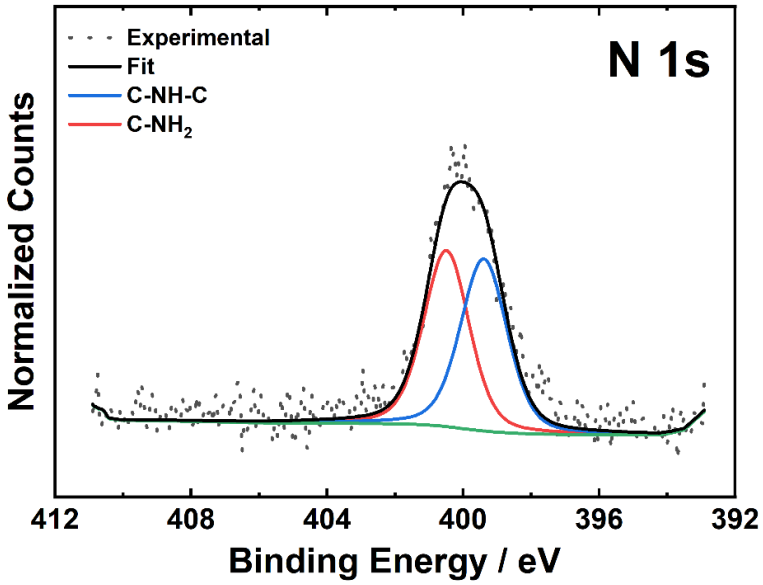

Figure 69: High-resolution XPS scan centered on the N 1s peaks for a Ni4N-coated FTO sample, with fitted experimental (black) and associated deconvoluted peaks.

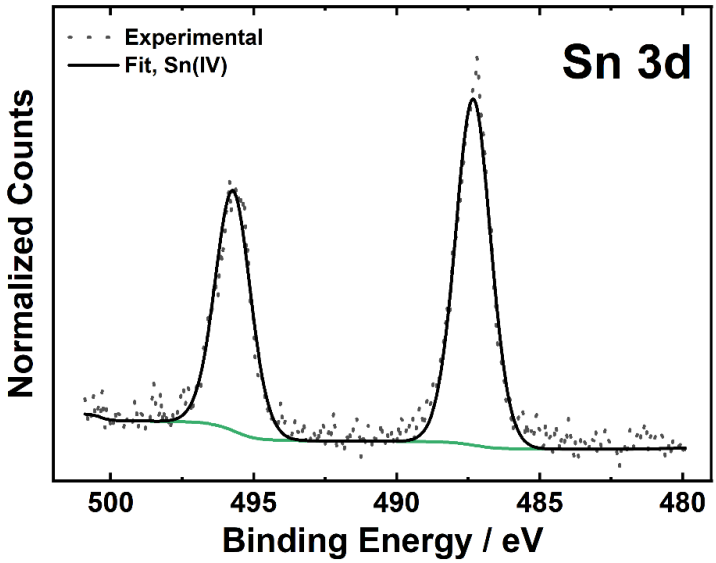

Figure 70: High-resolution XPS scan centered on the Sn 3d peaks for a Ni4N-coated FTO sample, with fitted experimental (black) and associated deconvoluted peaks.

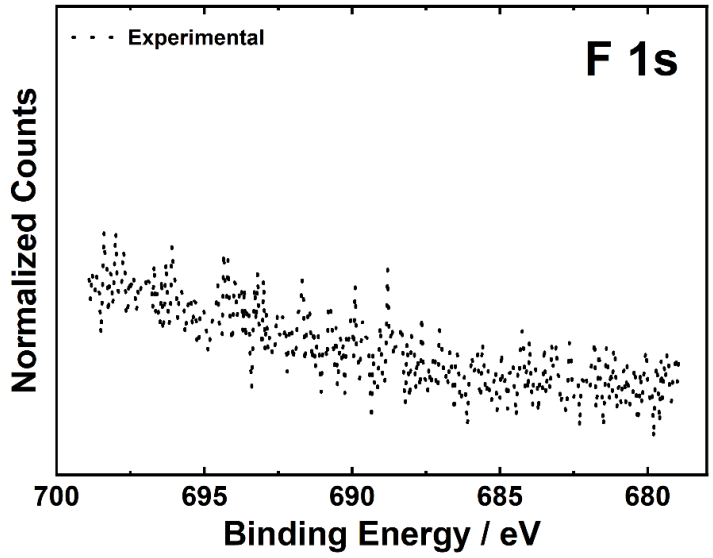

Figure 71: High-resolution XPS scan centered on the F 1s peaks for a Ni4N-coated FTO sample, with fitted experimental (black) and associated deconvoluted peaks.

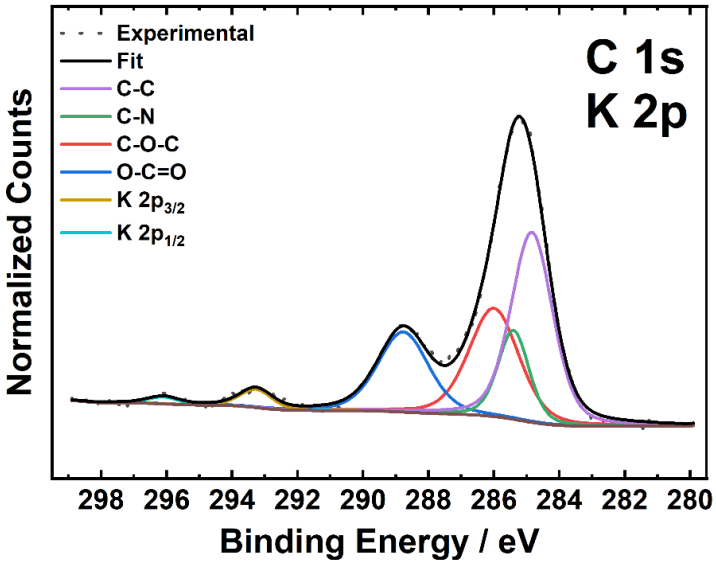

Figure 72: High-resolution XPS scan centered on the C 1s and K 2p peaks for a Ni4N-coated FTO sample, with fitted experimental (black) and associated deconvoluted peaks.

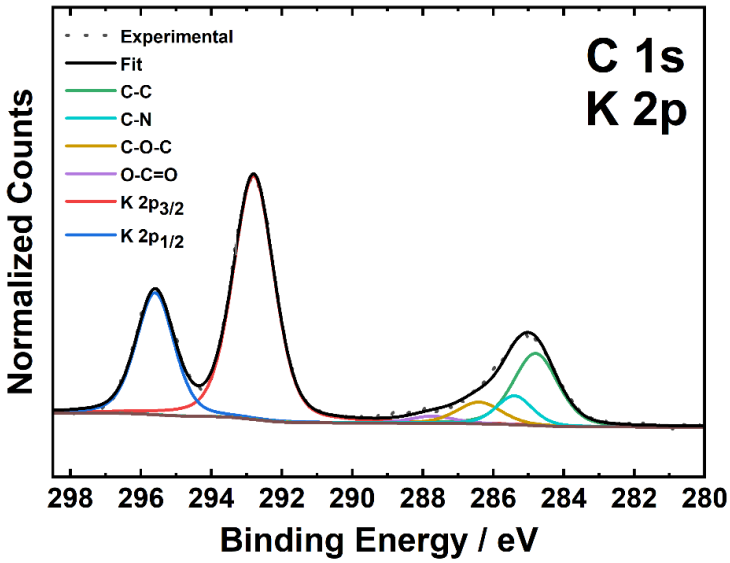

Figure 73: High-resolution XPS scan centered on the C 1s and K 2p peaks for a Ni4N-coated FTO sample with KCl deposition kept on surface, with fitted experimental (black) and associated deconvoluted peaks.

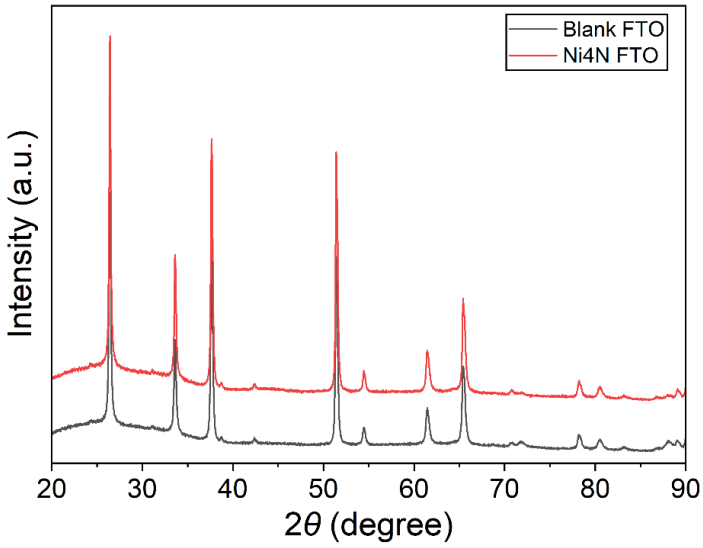

Figure 74: Graph of powder XRD for a blank FTO glass (black) and for a Ni4N-coated FTO sample (red).

4.7 – Experimental Details

4.7.1 – General Methods

Commercial reagents were purchased from Sigma-Aldrich, Alfa-Aesar and TCI America and were used without further purification. FTO Glass was purchased from Sigma-Aldrich. Synthesis reactions that were performed in an inert atmosphere were conducted under nitrogen. Electrochemical measurements were performed on a Princeton Applied Research VersaSTAT 3 Potentiostat. Single crystal XRD measurements were performed by the X-ray Core Facility staff at the University of Ottawa. Gas chromatography (GC) measurements were performed using an Agilent 7820 A equipped with a thermal conductivity detector (TCD) and Agilent select permanent gases column.

For detection of hydrogen gas, gas samples of 200 µL were taken using a 250 µL gas tight syringe, extracted from the headspace of the electrochemical cell. Hydrogen molar quantities were calculated from the detected area (µV·s) by GC-TCD from a prepared hydrogen calibration curve.

4.7.2 – Electrochemical Cell Setup

Electrochemical characterization of the complex was performed in a 40 mL three-neck flask with a glassy carbon working electrode for CV characterization, a silver wire as the reference electrode, and a platinum wire for the counter electrode. The regular cell standard is 15 mL of acetonitrile, 0.1 M of TBAHFP, and 1 mM of examined sample while purged under a nitrogen atmosphere. When water was the solvent, an Ag/AgCl reference electrode (3 M KCl) was used in place of the silver wire.

4.7.3 – Hydrogen Calibration Curve

Hydrogen results were calibrated by quantized gas injections of pure hydrogen into an Agilent 7820 A equipped with a thermal conductivity detector (TCD) and Agilent select permanent gases column. Four injections of 5 µL and 10 µL were performed, with single injections of 50 µL and 100 µL. A non-fixed zero data point was also included. Main calibration fitting including all data points is $Y = 139.5x + 9.71$ with $R^2 = 0.999$ (Figure 75). As an example, excluding the 50 and 100 µL samples, fitting is $Y = 137.68x - 38.39$ with R^2

= 0.995. Area results were parsed into the equation and converted from µL into µmol by the ideal gas law equation (PV = nRT) at NTP of 20 °C and 1 atm. Experimental tests injected a 200 µL gas sample of the electrochemical cell, with this result converted upward to 24.95 mL of contained headspace.

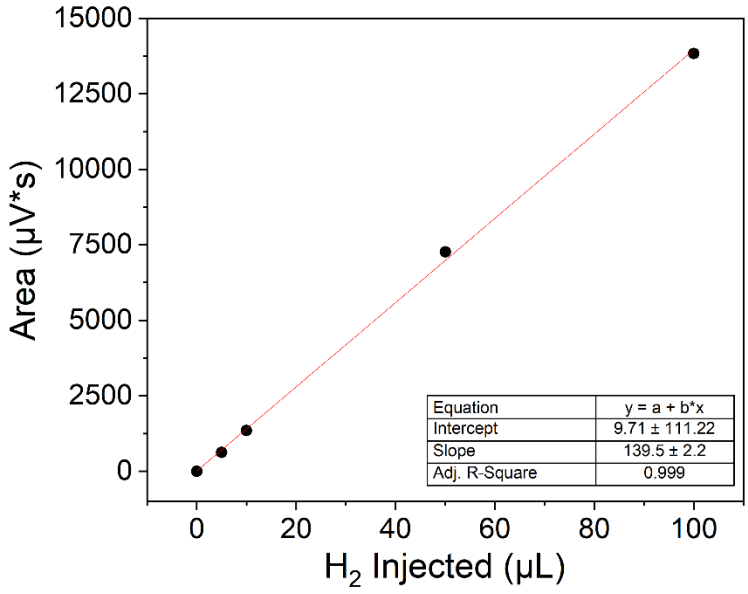

Figure 75: H_2 Calibration Curve with pure hydrogen samples injected into a GC-TCD.

4.7.4 – Surface Characterization Methods

Surface characterization measurements were performed by Dr. Jurca's group at the University of Central Florida. SEM-EDS measurements were performedon a Zeiss ULTRA-55 FEG SEM. Samples were mounted on the holder using carbon tape and coated with gold for measurement to improve imaging. The Noran System 7 EDS system with Silicon Drift Detector x-ray detector acquired the EDS spectrum. The resolution is 1 nm at

15 KV and 1.7 nm at 1 KV. AFM was performed in contact mode (Park NX10) at a resonance frequency of 200-400 kHz and force constant of 13-77 N/m using a AppNANO cantilever (SPM Probe model: ACTA Part # ACTA-20). Measurements were conducted on several areas (1 μm × 1 μm) to yield an average roughness for each sample. Data was processed via Gwyddion software. XPS data was obtained using a Thermo Scientific ESCALAB XI+ X-ray Photoelectron Spectrometer with an Al Kα X-ray source (1486.67 eV) and spot size of 200 μm. Samples were mounted on carbon tape for analysis. A pass energy of 20.0 eV was used with energy step sizes of 0.05 eV and 50 ms dwell times for the high-resolution spectra and step sizes of 0.5 eV with 20 ms dwell times for the survey scans. XPS peak fitting was completed through Thermo Scientific's Advantage Data System. Binding energies acquired were calibrated to carbon 1s sp^3 at 284.8 eV.

4.7.5 – Synthesis of Cu3N2O, Cu4N, Ni4N

Synthesis of the Cu3N2O Complex: $CuBr_2$ (0.279 g, 223.37 g/mol, 1.25 mmol), 2,6-diacetylpyridine (0.204 g, 163.17 g/mol, 1.25 mmol), and 1,8-Diamino-3,6-dioxaoctane (0.185 g, 148.20 g/mol, 0.96 g/mL, 1.25 mmol), were measured in a 1:1:1 molar ratio. Each reagent was pre-dissolved in ~5 mL 95% ethanol, with holding vials washed with ~1 mL ethanol to collect remnants, to be combined in a 50 mL round bottom flask. These were added stepwise by the order above to the flask with the initial solution colour of $CuBr_2$ alone being brown-black, lighter brown with 2,6-diacetylpyridine addition, and with addition of 1,8-diamino-3,6-dioxaoctane slowly changed colour to a lighter green. The reaction flask was kept significantly below reflux temperature and heated to

approximately 45-50 °C under moderate stirring for a period of 1 h, where the solution slowly changed colour to dark green blue (Figure 76, A and B). After 1 h, a large amount of light green precipitate was observed. After cooling to room temperature, this solution with precipitate was filtered and washed with ethanol, which left a wet light green solid was initially agglomerated together. After drying overnight this solid easily broke apart and formed a light green powder weighing 0.171 g, with the yield calculated for the proposed product as 34% (397.64 g/mol). The species was characterized by FTIR with positive correlations at 1650 cm^{-1} (m, N-H, imine), 1580 cm^{-1} (m, C=C, pyridine), lack of absorption at 1700 cm^{-1} (carbonyl), and discrete differences to species Ni4N and Cu4N.[56]

During the initial trial to synthesis Cu3N2O, it experienced some troubles during the initial steps. During the initial heating, the temperature was brought up to 55 °C and rising as detected in the oil bath, intending to reflux the ethanol solution over 2 h. It was observed that the solution slowly discoloured from a prominent green blue to a murky brown, with black precipitate stuck to the bottom of the flask (Figure 76, C). Overall, the physical characteristics did not match that of expected observations, with distinct colours often decorating metal complexes and colours along brown or black may indicate some form of unsuccessful synthesis. Retaining the temperature lower at 45-50 °C, the solution retained its primary green colour and produced a light green precipitate, used in further testing (Figure 76, D).

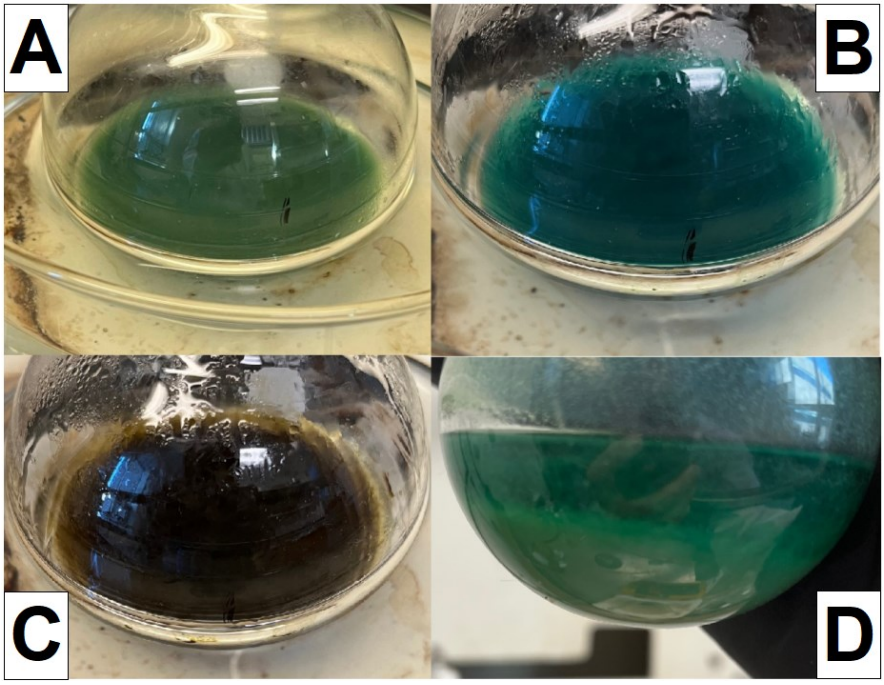

Figure 76: Reaction flask for synthesis of Cu3N2O at varying stages. Initial state of flask (A), flask under ~45-50 °C after 10 min (B), flask under ~55-60 °C after 2 h (C), flask retained at lower ~45-50 °C, after 1 h, removed from heat (D).

Synthesis of the Ni4N complex: $NiCl_2 \cdot 6H_2O$ (0.297 g, 237.69 g/mol, 1.25 mmol), and 1,2-bis(3-aminopropylamino)ethane (0.218 g, 174.29 g/mol, 0.952 g/mL, 1.25 mmol), were measured in a 1:1 molar ratio. Each reagent was pre-dissolved in ~5 mL 95% ethanol, with holding vials washed with ~1 mL ethanol to collect remnants, to be combined in a 50 mL round bottom flask. These were added step-wise by the order above to the flask with the initial solution colour being light green, and a strong colour change to dark blue-purple with addition of 1,2-bis(3-aminopropylamino)ethane. The reaction flask was refluxed under moderate stirring for a period of 2 h, after which the flask was removed from heat. The solution appeared blue at this point. This solution was placed under rotary

evaporation until a minimal amount of liquid remained (~1-2 mL). A significant amount of light purple precipitate was observed collecting on the sides and bottom. ~40 mL of diethyl ether was added to collect the remaining liquid as well as to cause remaining product to precipitate out. With two additional washings with diethyl ether, the solution was removed and the solid was left to dry overnight, seen as a dark purple powder. The product weighed 0.293 g (303.89 g/mol), with a yield of 77%. Crystals of Ni4N suitable for SC-XRD were acquired by slow diffusion of acetonitrile with diethyl ether.

Synthesis of the Cu4N Complex: $CuBr_2$ (0.279 g, 223.37 g/mol, 1.25 mmol), 2,6-diacetylpyridine (0.204 g, 163.17 g/mol, 1.25 mmol), and 1,2-bis(3-aminopropylamino)-ethane (0.218 g, 174.29 g/mol, 0.952 g/mL, 1.25 mmol), were measured in a 1:1:1 molar ratio. Each reagent was pre-dissolved in ~5 mL 95% ethanol, with holding vials washed with ~1 mL ethanol to collect remnants, to be combined in a 50 mL round bottom flask. These were added step-wise by the order above to the flask with the initial solution colour of $CuBr_2$ alone being brown-black, lighter brown with 2,6-diacetylpyridine addition, and a strong colour change to dark purple-blue with addition of 1,2-bis(3-aminopropylamino)ethane. The reaction flask was refluxed under moderate stirring for a period of 2 h, after which the flask was removed from heat with the solution colour as dark blue green. After cooling, sodium perchlorate (0.168 g, 1.375 mol) was added in a 1.1 molar ratio and stirred for 30 min. This solution was filtered with a paper filter, and the solution was placed under rotary evaporation with solvent removed until approx. 2 mL remained. The remaining blue liquid had ~40 mL of diethyl ether mixed with it. The solution turned cloudy purple, with dark blue solid rapidly (<30 seconds) agglomerating

on the sides. With two additional washing with diethyl ether, the solution was removed and the solid was left to dry overnight. While wet this powder was dark blue, and after drying seen as a purple powder with a mass of 0.538 g (497.09 g/mol), with a yield of 87% yield. Crystals of Cu4N suitable for SC-XRD were acquired by slow diffusion of acetonitrile with diethyl ether.

4.7.6 – FTO Glass Preparation

The FTO plate has been manually cut using a glass cutter from an original 5 cm by 5 cm plate, cut into 1 cm by 5 cm sections for experimental use. The 1 cm plate width could be estimated to be generally ± 1 mm from the desired 1 cm measurements using a ruler. This sample FTO plate was cleaned with DI water and dry Kimwipe before insertion into the electrochemical cell. The plate electrical connection was made with an alligator working electrode clip passed through a standard rubber septa size 19/22. With synthesis for coating of the FTO plate, approximately 2 cm x 1 cm of the FTO plate is immersed in solution, with the conductive surface facing into the center of the cell. A counter electrode with a platinum wire and platinum mesh held at the opposite side, with an Ag/AgCl reference electrode held in place in the approx. center of the two other electrodes. The approximate distance between electrodes is 3 cm. The solution was 15 mL of DI water, 0.1 M KCl (0.112 g), and 0.5 mM of complex when the coating process occurs – concentration of complex varying by experiment. DI water is purged of air with

bubbling N_2 for 15 min before use and 15 min after cell is set-up in order to establish a nitrogen atmosphere in solution and in the cell.

Typical settings of the electrochemical coating process include a CV scan from 0 to -1.5 V for 3 passes, a CPE experiment holding potential at the working electrode at -1.3 V for 1 h, and a post-CPE CV scan from 0 to -1.5V (*vs.* Ag/AgCl) with 3 passes. After the coating process is complete, the FTO plate is removed and left to air dry without further cleaning. Before testing, the FTO plate is immersed in DI water for 2 min to remove residual salt layers and to assist in ensuring that there are no free-standing remnants on any particular sample. The test for hydrogen production follows the above steps with noted held potential (-1.0 V, -1.1 V, -1.2 V, -1.3 V), with the main tested potential being -1.2 V (*vs.* Ag/AgCl). The electrochemical cell was subsequently taken to gas chromatography to detect gases present in the cell headspace.

Chapter 5: Conclusion and Outlook

This thesis covers the electrochemical exploration of several complexes based on Mn, Mo, Fe, Ni and Cu 3d transition metals. The primary objective was to catalyze the hydrogen evolution reaction (HER), focusing on using electrolysis of water as the ideal proton source. As an alternative, acetic acid as a substrate was also investigated. Chapter 2 introduces the electrochemical exploration of five metal complexes, primarily those on pyridine-based tridentate and bidentate complexes with Mn(I), Mo(0) and Mo(VI). In the course of this exploration, it was found that non-desirable reactions or by-products occurred through the reduction of these complexes, often attributable to the presence of water or acetic acid. This is presented visually and by electrochemical characterization. Visually as deposition onto the working and counter electrode or by dispersing into solution. Electrochemically, this is shown in cyclic voltammetry as shifts of redox peaks, changes in current including growth as enhancement, or elimination. Even though these were not favourable outcomes, it led to greater knowledge and handling of these metal complexes.

Chapter 3 shifts the focus to a new series of complexes using macrocyclic closed-ring ligands also displaying a pyridine-ligating group. Six complexes with Mn(II), Fe(III), Ag(I) and Ni(II) were synthesized with quinquedentate N_5 and N_3O_2 macrocyclic ligands. Three new structures were elucidated by single crystal XRD that are not present in the Cambridge database. The electrochemical characterizations were primarily exploratory, with cyclic voltammetry performed in acetonitrile with additions of water to observe if

HER catalytic enhancement was present. Ni5N-3,2,3 was additionally explored in the presence of MOPS free acid and $NaNO_2$, to observe reduction event characteristics and if the NO_2^- anion could be reduced with these events, which was determined not to occur. Future work with these macrocyclic complexes may continue, exploring different ligand choices and modifying the substrate used for electrocatalytic activity.

In Chapter 4, electrodeposition of the Cu3N2O complex on the working electrode was found to occur in aqueous solution under applied reduction potentials. This was observed as a copper-colour film along with a dark-blue film at differing sections of the electrode. This film was found to produce quantifiable amounts of hydrogen gas by electrolysis of water, at potentials below background influence (-1.3 V *vs.* Ag/AgCl). This was compared with copper wire as an analogue to the electrodeposited film, where the hydrogen output yielded a significant difference, Cu3N2O as 24.2 µmol and the copper wire as 1.2 µmol.

Development of these findings continued with Ni4N, an open-ended tetradentate complex. The Ni4N complex was crystallized and characterized by single crystal XRD to yield a structure not present in the Cambridge database. The initial cyclic voltammetry of the complex in 0.1 M KCl aqueous solution revealed a significantly stronger current flow to electrodeposited films from Cu3N2O. At -2.0 V (*vs.* Ag/AgCl), a current of ~4.0 mA was observed compared to ~1.2 mA with the film from Cu3N2O. Analysis of the evolved hydrogen gas testing indicated a moderately higher H_2 amount produced of 29.0 µmol. From here an FTO glass electrode was chosen for the electrodeposition and a dark-grey film was observed. This was compared with films generated with $NiCl_2$ as a starting

material, which interestingly showed similar electrochemical features to that of Ni4N-coated FTO and likewise creating a relatively darker grey film, but with a current density about 1/10 of that from Ni4N.

Experiments into the various properties of the Ni4N-coated FTO were carried out. The minimum starting potential for initiation of electrodeposition appeared to be at -1.05 V (*vs.* Ag/AgCl), but after this initiation has begun, it appears a lower potential e.g. -0.70 V was effective for continued deposition. This is theorized as likely due to the initial formation of film on the FTO surface supporting further film formation at lower potentials. Brief testing indicated that applied potential of -1.0 V led to detectable hydrogen production at 5.9 µmol and increased potential of -1.1 V producing 15.9 µmol H_2. For better comparability to literature, -1.2 V (*vs.* Ag/AgCl) was chosen for CPE during hydrogen production. The optimal Ni4N concentration for initial coating was evaluated to be 0.5 mM based on hydrogen output, which averaged 46.7 µmol with a Faradaic efficiency of 95.8% ± 6.2%. Over an extended period of 5 h, films produced in this manner were found to produce 131.4 µmol H_2, with a Faradaic efficiency of 57%. To identify onset and overpotentials, an alternative setup with 0.5 M H_2SO_4 was used. The onset for hydrogen evolution was determined to be 68 mV (*vs.* RHE), and overpotentials with current densities of 0.1 and 1.0 mA cm^{-2} were 220 mV and 345 mV respectively. The Tafel slope was determined to be 94 mV dec^{-1}, comparing well with literature. Surface characterization was performed on the Ni4N-coated FTO glass by SEM-EDS, AFM, EDX, XPS, and powder XRD, and indicated that the film as $NiO/Ni(OH)_2$.

Potential future work stemming from this thesis could be further exploration of the Ni4N-derived film and optimizing the quality of these films. Further investigation of the long-term stability during HER, exploring the effects of higher potentials on the film formation and total hydrogen production, and the nature of the film being susceptible to oxidative potentials. Annealing the film may provide another avenue for research, as it has been noted in literature that thermal treatment can dehydrate $Ni(OH)_2$ to NiO, potentially increasing conductivity of the film and thus HER effectiveness.[73] Additionally, synthesizing alternative metal complexes, such as using cobalt with 1,2-bis(3-aminopropylamino)ethane to form a similar starting material for film formation may be fruitful for investigation.

References

(1) Fischer, M.; Werber, M.; Schwartz, P. V. Batteries: Higher Energy Density than Gasoline? *Energy Policy* **2009**, *37* (7), 2639–2641. https://doi.org/10.1016/j.enpol.2009.02.030.

(2) Xu, Y.; Deng, Y.; Liu, W.; Zhao, X.; Xu, J.; Yuan, Z. Research Progress of Hydrogen Energy and Metal Hydrogen Storage Materials. *Sustain Energy Technol.* **2023**, *55*. https://doi.org/10.1016/j.seta.2022.102974.

(3) Kojima, Y. Hydrogen Storage Materials for Hydrogen and Energy Carriers. *Int J Hydrogen Energy* **2019**, *44* (33), 18179–18192. https://doi.org/10.1016/j.ijhydene.2019.05.119.

(4) Franchi, G.; Capocelli, M.; De Falco, M.; Piemonte, V.; Barba, D. Hydrogen Production via Steam Reforming: A Critical Analysis of MR and RMM Technologies. *Membranes (Basel)* **2020**, *10* (1). https://doi.org/10.3390/membranes10010010.

(5) Howarth, R. W.; Jacobson, M. Z. How Green Is Blue Hydrogen? *Energy Sci Eng* **2021**, *9* (10), 1676–1687. https://doi.org/10.1002/ese3.956.

(6) Dixon, R. K.; Li, J.; Wang, M. Q. Progress in Hydrogen Energy Infrastructure Development—Addressing Technical and Institutional Barriers. In *Compendium of Hydrogen Energy: Hydrogen Storage, Distribution and Infrastructure: Volume 2*; Elsevier, 2015; pp 323–343. https://doi.org/10.1016/B978-1-78242-362-1.00013-4.

(7) Christoforidis, K. C.; Fornasiero, P. Photocatalytic Hydrogen Production: A Rift into the Future Energy Supply. *ChemCatChem* **2017**, *9* (9), 1523–1544. https://doi.org/10.1002/cctc.201601659.

(8) Chen, L.; Qi, Z.; Zhang, S.; Su, J.; Somorjai, G. A. Catalytic Hydrogen Production from Methane: A Review on Recent Progress and Prospect. *Catalysts* **2020**, *10* (8). https://doi.org/10.3390/catal10080858.

(9) Chen, W. H.; Chen, C. Y. Water Gas Shift Reaction for Hydrogen Production and Carbon Dioxide Capture: A Review. *Appl Energy* **2020**, *258*. https://doi.org/10.1016/j.apenergy.2019.114078.

(10) Liu, Z.; Deng, Z.; Davis, S. J.; Ciais, P. Global Carbon Emissions in 2023. *Nat Rev Earth Environ* **2024**, *5* (4), 253–254. https://doi.org/10.1038/s43017-024-00532-2.

(11) Ramachandran, R.; Menont, R. K. AN OVERVIEW OF INDUSTRIAL USES OF HYDROGEN. *Int J Hydrogen Energy* **1998**, *23* (7), 593–598.

(12) Tarhan, C.; Çil, M. A. A Study on Hydrogen, the Clean Energy of the Future: Hydrogen Storage Methods. *J Energy Storage* **2021**, *40*. https://doi.org/10.1016/j.est.2021.102676.

(13) Do, T. N.; Kwon, H.; Park, M.; Kim, C.; Kim, Y. T.; Kim, J. Carbon-Neutral Hydrogen Production from Natural Gas via Electrified Steam Reforming: Techno-Economic-Environmental Perspective. *Energy Convers Manag* **2023**, *279*. https://doi.org/10.1016/j.enconman.2023.116758.

(14) Chen, W. H.; Biswas, P. P.; Ong, H. C.; Hoang, A. T.; Nguyen, T. B.; Dong, C. Di. A Critical and Systematic Review of Sustainable Hydrogen Production from Ethanol/Bioethanol: Steam Reforming, Partial Oxidation, and Autothermal Reforming. *Fuel* **2023**, *333*. https://doi.org/10.1016/j.fuel.2022.126526.

(15) Niu, S.; Li, S.; Du, Y.; Han, X.; Xu, P. How to Reliably Report the Overpotential of an Electrocatalyst. *ACS Energy Lett* **2020**, *5* (4), 1083–1087. https://doi.org/10.1021/acsenergylett.0c00321.

(16) Yokoyama, Y.; Fukutsuka, T.; Miyazaki, K.; Abe, T. Origin of the Electrochemical Stability of Aqueous Concentrated Electrolyte Solutions. *J Electrochem Soc* **2018**, *165* (14), A3299–A3303. https://doi.org/10.1149/2.0491814jes.

(17) Qiu, J.; Moeller, A.; Zhen, J.; Yang, H.; Din, L.; Adelstein, N. Teaching Heterogeneous Electrocatalytic Water Oxidation with Nickel- and Cobalt-Based Catalysts Using Cyclic Voltammetry and Python Simulation. *J Chem Educ* **2023**, *100* (8), 3036–3043. https://doi.org/10.1021/acs.jchemed.3c00176.

(18) Groenemans, H.; Saur, G.; Mittelsteadt, C.; Lattimer, J.; Xu, H. Techno-Economic Analysis of Offshore Wind PEM Water Electrolysis for H_2 Production. *Curr Opin Chem Eng* **2022**, *37*. https://doi.org/10.1016/j.coche.2022.100828.

(19) Anwar, S.; Khan, F.; Zhang, Y.; Djire, A. Recent Development in Electrocatalysts for Hydrogen Production through Water Electrolysis. *Int J Hydrogen Energy* **2021**, *46* (63), 32284–32317. https://doi.org/10.1016/j.ijhydene.2021.06.191.

(20) Dong, S.; Li, Y.; Zhao, Z.; Li, R.; He, J.; Yin, J.; Yan, B.; Zhang, X. A Review of the Application of Heterostructure Catalysts in Hydrogen Evolution Reaction. *ChemistrySelect* **2022**, *7* (14). https://doi.org/10.1002/slct.202104041.

(21) Gandeepan, P.; Finger, L. H.; Meyer, T. H.; Ackermann, L. 3d Metallaelectrocatalysis for Resource Economical Syntheses. *Chem Soc Rev* **2020**, *49* (13), 4254–4272. https://doi.org/10.1039/d0cs00149j.

(22) Wang, S.; Lu, A.; Zhong, C. J. Hydrogen Production from Water Electrolysis: Role of Catalysts. *Nano Converg* **2021**, *8* (1). https://doi.org/10.1186/s40580-021-00254-x.

(23) Bullock, R. M.; Che, J. G.; Gagliardi, L.; Chiri, P. J.; Farh, O. K.; Hendo, C. H.; Jone, C. W.; Keit, J. A.; Klosin, J.; Mintee, S. D.; Morri, R. H.; Radosevic, A. T.; Rauchfus, T. B.; Strotma, N. A.; Vojvodic, A.; War, T. R.; Yan, J. Y.; Surendranath, Y. Using Nature's Blueprint to Expand Catalysis with Earth-Abundant Metals. *Science (1979)* **2020**, *369* (6505). https://doi.org/10.1126/science.abc3183.

(24) Elgrishi, N.; Rountree, K. J.; McCarthy, B. D.; Rountree, E. S.; Eisenhart, T. T.; Dempsey, J. L. A Practical Beginner's Guide to Cyclic Voltammetry. *J Chem Educ* **2018**, *95* (2), 197–206. https://doi.org/10.1021/acs.jchemed.7b00361.

(25) Rountree, E. S.; McCarthy, B. D.; Eisenhart, T. T.; Dempsey, J. L. Evaluation of Homogeneous Electrocatalysts by Cyclic Voltammetry. *Inorg Chem* **2014**, *53* (19), 9983–10002. https://doi.org/10.1021/ic500658x.

(26) Appel, A. M.; Helm, M. L. Determining the Overpotential for a Molecular Electrocatalyst. *ACS Catal* **2014**, *4* (2), 630–633. https://doi.org/10.1021/cs401013v.

(27) Bard, A. J.; Faulkner, L. R. *Electrochemical Methods : Fundamentals and Applications*.

(28) Majumder, S.; Abdel Haleem, A.; Nagaraju, P.; Naruta, Y. A New Preparation of a Bifunctional Crystalline Heterogeneous Copper Electrocatalyst by Electrodeposition Using a Robson-Type Macrocyclic Dinuclear Copper Complex for Efficient Hydrogen and Oxygen Evolution from Water. *Dalton Transactions* **2017**, *46* (28), 9131–9139. https://doi.org/10.1039/c7dt01594a.

(29) Lv, W.; Zhang, R.; Gao, P.; Lei, L. Studies on the Faradaic Efficiency for Electrochemical Reduction of Carbon Dioxide to Formate on Tin Electrode. *J Power Sources* **2014**, *253*, 276–281. https://doi.org/10.1016/j.jpowsour.2013.12.063.

(30) Heard, D. M.; Lennox, A. J. J. Electrode Materials in Modern Organic Electrochemistry. *Angew. Chem. Int. Ed.* **2020**, *59* (43), 18866–18884. https://doi.org/10.1002/anie.202005745.

(31) Hughes, J. P.; Clipsham, J.; Chavushoglu, H.; Rowley-Neale, S. J.; Banks, C. E. Polymer Electrolyte Electrolysis: A Review of the Activity and Stability of Non-Precious Metal Hydrogen Evolution Reaction and Oxygen Evolution Reaction Catalysts. *Renewable and Sustainable Energy Reviews* **2021**, *139*. https://doi.org/10.1016/j.rser.2021.110709.

(32) Wang, X.; Xing, X.; Huo, Y.; Zhao, Y.; Li, Y.; Chen, H. Study of Tetraethylammonium Bis(Trifluoromethylsulfonyl)Imide as a Supporting Electrolyte for an All-Organic Redox Flow Battery Using Benzophenone and 1,4-Di-Tert-Butyl-2,5-Dimethoxybenzene as Active Species. *Int J Electrochem Sci* **2018**, *13* (7), 6676–6683. https://doi.org/10.20964/2018.07.56.

(33) Gong, K.; Fang, Q.; Gu, S.; Li, S. F. Y.; Yan, Y. Nonaqueous Redox-Flow Batteries: Organic Solvents, Supporting Electrolytes, and Redox Pairs. *Energy Environ Sci* **2015**, *8* (12), 3515–3530. https://doi.org/10.1039/c5ee02341f.

(34) Tomiyasu, H.; Shikata, H.; Takao, K.; Asanuma, N.; Taruta, S.; Park, Y. Y. An Aqueous Electrolyte of the Widest Potential Window and Its Superior Capability for Capacitors. *Sci Rep* **2017**, *7*. https://doi.org/10.1038/srep45048.

(35) Zamora Zeledón, J. A.; Jackson, A.; Stevens, M. B.; Kamat, G. A.; Jaramillo, T. F. Methods—A Practical Approach to the Reversible Hydrogen Electrode Scale. *J Electrochem Soc* **2022**, *169* (6), 066505. https://doi.org/10.1149/1945-7111/ac71d1.

(36) Jerkiewicz, G. Standard and Reversible Hydrogen Electrodes: Theory, Design, Operation, and Applications. *ACS Catal* **2020**, *10* (15), 8409–8417. https://doi.org/10.1021/acscatal.0c02046.

(37) Wang, H.; Wang, M.; Wang, J. How to Choose Suitable Reference Electrode and Aqueous Electrolyte to Avoid Error in Electrochemical Measurements? *Current Chinese Science* **2022**, *3* (3), 204–212. https://doi.org/10.2174/2210298103666221102092735.

(38) Zeng, M.; Li, Y. *Recent Advances in Heterogeneous Electrocatalysts for the Hydrogen Evolution Reaction*; Royal Society of Chemistry, 2015; Vol. 3. https://doi.org/10.1039/c5ta02974k.

(39) Zhao, J.; Tran, P. D.; Chen, Y.; Loo, J. S. C.; Barber, J.; Xu, Z. J. Achieving High Electrocatalytic Efficiency on Copper: A Low-Cost Alternative to Platinum for Hydrogen Generation in Water. *ACS Catal* **2015**, *5* (7), 4115–4120. https://doi.org/10.1021/acscatal.5b00556.

(40) Laursen, A. B.; Varela, A. S.; Dionigi, F.; Fanchiu, H.; Miller, C.; Trinhammer, O. L.; Rossmeisl, J.; Dahl, S. Electrochemical Hydrogen Evolution: Sabatiers Principle and the Volcano Plot. *J Chem Educ* **2012**, *89* (12), 1595–1599. https://doi.org/10.1021/ed200818t.

(41) Banoth, P.; Kandula, C.; Kollu, P. Introduction to Electrocatalysts. In *ACS Symposium Series*; American Chemical Society, 2022; Vol. 1432, pp 1–37. https://doi.org/10.1021/bk-2022-1432.ch001.

(42) Liu, X.; Li, S.; Liu, Y.; Cao, Y. Formic Acid: A Versatile Renewable Reagent for Green and Sustainable Chemical Synthesis. *Cuihua Xuebao/Chinese Journal of Catalysis* **2015**, *36* (9), 1461–1475. https://doi.org/10.1016/S1872-2067(15)60861-0.

(43) Xu, H.; Rebollar, D.; He, H.; Chong, L.; Liu, Y.; Liu, C.; Sun, C. J.; Li, T.; Muntean, J. V.; Winans, R. E.; Liu, D. J.; Xu, T. Highly Selective Electrocatalytic CO_2 Reduction to Ethanol by Metallic Clusters Dynamically Formed from Atomically Dispersed Copper. *Nat Energy* **2020**, *5* (8), 623–632. https://doi.org/10.1038/s41560-020-0666-x.

(44) Li, S.; Nagarajan, A. V.; Li, Y.; Kauffman, D. R.; Mpourmpakis, G.; Jin, R.; Kauffman, D. R.; Mpourmpakis, G.; Jin, R. The Role of Ligands in Atomically Precise Nanocluster-Catalyzed CO_2 Electrochemical Reduction. *Nanoscale* **2021**, *13* (4), 2333–2337. https://doi.org/10.1039/d0nr07832h.

(45) Wang, J.; Zang, W.; Liu, X.; Sun, J.; Xi, S.; Liu, W.; Kou, Z.; Shen, L.; Wang, J. Switch Volmer-Heyrovsky to Volmer-Tafel Pathway for Efficient Acidic Electrocatalytic Hydrogen Evolution by Correlating Pt Single Atoms with Clusters. *Small* **2024**. https://doi.org/10.1002/smll.202309427.

(46) Lasia, A. Mechanism and Kinetics of the Hydrogen Evolution Reaction. *Int J Hydrogen Energy* **2019**, *44* (36), 19484–19518. https://doi.org/10.1016/j.ijhydene.2019.05.183.

(47) Rao, G. K.; Jamshidi, M. P.; Dawkins, J. I. G.; Pell, W.; Korobkov, I.; Richeson, D. Electrocatalytic Generation of H_2 from Neutral Water in Acetonitrile Using Manganese Polypyridyl Complexes with Ligand Assistance. *Dalton Trans.* **2017**, *46* (20), 6518–6522. https://doi.org/10.1039/c7dt01039g.

(48) Wietzke, R.; Mazzanti, M.; Latour, J. M.; Pécaut, J.; Cordier, P. Y.; Madic, C. Lanthanide(III) Complexes of Tripodal N-Donor Ligands: Structural Models for the Species Involved in Solvent Extraction of Actinides(III). *Inorg Chem* **1998**, *37* (26), 6690–6697. https://doi.org/10.1021/ic980192n.

(49) Natrajan, L.; Pécaut, J.; Mazzanti, M.; LeBrun, C. Controlled Hydrolysis of Lanthanide Complexes of the N-Donor Tripod Tris(2-Pyridylmethyl)Amine versus Bisligand Complex Formation. *Inorg Chem* **2005**, *44* (13), 4756–4765. https://doi.org/10.1021/ic0502224.

(50) Li Xu; Yoichi Sasaki; Masaaki Abe. Syntheses, Structures, and Fluxional Behavior of Tricarbonylmolybdenum(0) and Trioxomolybdenum(VI) Complexes of Tris(2-Pyridylmethyl)Amine with One Free Arm. *Chem Lett* **1999**, 163–164.

(51) Van Staveren, D. R.; Bothe, E.; Weyhermüller, T.; Metzler-Nolte, N. Spectroscopic Properties, Electrochemistry, and Reactivity of Mo^0, Mo^I, and Mo^{II} Complexes with the [Mo(Bpa)$(CO)_3$] Unit [Bpa = Bis(2-Picolyl)Amine] and Their Application for the Labelling of Peptides. *Eur J Inorg Chem* **2002**, 1518–1529.

(52) Land, M. A. Designing Volatile Molybdenum Compounds for Vapor-Phase Deposition. Ph.D. Thesis, Carleton University, Ottawa, ON, 2023.

(53) Salignac, B.; Grundler, P. V.; Cayemittes, S.; Frey, U.; Scopelliti, R.; Merbach, A. E.; Hedinger, R.; Hegetschweiler, K.; Alberto, R.; Prinz, U.; Raabe, G.; Kölle, U.; Hall, S. Reactivity of the Organometallic Fac-$[(CO)_3Re^I(H_2O)_3]^+$ Aquaion. Kinetic and Thermodynamic Properties of H_2O Substitution. *Inorg Chem* **2003**, *42* (11), 3516–3526. https://doi.org/10.1021/ic0341744.

(54) Gonzalez, M. A.; Yim, M. A.; Cheng, S.; Moyes, A.; Hobbs, A. J.; Mascharak, P. K. Manganese Carbonyls Bearing Tripodal Polypyridine Ligands as Photoactive Carbon Monoxide-Releasing Molecules. *Inorg Chem* **2012**, *51* (1), 601–608. https://doi.org/10.1021/ic2021287.

(55) Thakur, M. S.; Singh, N.; Sharma, A.; Rana, R.; Abdul Syukor, A. R.; Naushad, M.; Kumar, S.; Kumar, M.; Singh, L. Metal Coordinated Macrocyclic Complexes in Different Chemical Transformations. *Coord Chem Rev* **2022**, *471*. https://doi.org/10.1016/j.ccr.2022.214739.

(56) Nelson, S. M.; Mcfall, S. G.; Drew, M. G. B.; Bin Othman, A. H. The Coordination Chemistry of Some Pentadentate Macrocyclic Ligands. *J.C.S. Chem. Comm.* **1977**, *77*, 523–532.

(57) Wang, J.; Yamauchi, K.; Huang, H.; Sun, J.; Luo, Z.; Zhong, D.; Lu, T.; Sakai, K. A Molecular Cobalt Hydrogen Evolution Catalyst Showing High Activity and Outstanding Tolerance to CO and O_2. *Angewandte Chemie* **2019**, *131* (32), 11039–11043. https://doi.org/10.1002/ange.201904578.

(58) Nelson, S. M.; Mcllroy, P. D. A.; Stevenson, C. S.; Konig, E.; Ritter, G.; Waigel, J. Quadridentate versus Quinquedentate Co-Ordination of Some N, and N,O, Macrocyclic Ligands and an Unusual Thermally Controlled Quintete Singlet Spin Transition in an Iron(II) Complex. **1986**.

(59) Nelson, S. M. DEVELOPMENTS IN THE SYNTHESIS AND COORDINATION CHEMISTRY OF MACROCYCLIC SCHIFF BASE LIGANDS. *Pure & Appl. Chem* **1980**, *52*, 2461–2476.

(60) Zhang, D.; Wang, H.; Chen, Y.; Zhang, L.; Tian, L.; Ni, Z. H.; Jiang, J. Synthesis, Structure, and Magnetic Properties of Cyanide-Bridged Low-Dimensional Heterometallic Fe^{III}-Mn^{II} Complexes. *Dalton Transactions* **2009**, No. 43, 9418–9425. https://doi.org/10.1039/b909717a.

(61) Cairns, C.; Mcfall, S. G.; Nelson, S. M.; Drew, M. G. B. Nickel(II) Complexes of Quinquedentate Macrocyclic Ligands and the Crystal and Molecular Structure of the Ring-Opened Hydrolysis Product [11-(6-Acetyl-2-Pyridyl)-3,7,10-Triazadodec-10-Enylamine-NN'N''N'''N'''']-Aquanickel(II) Diperchlorate. *J.C.S. Dalton* **1979**, 446–453.

(62) Persson, I. Ferric Chloride Complexes in Aqueous Solution: An EXAFS Study. *J Solution Chem* **2018**, *47*, 797–805. https://doi.org/10.1007/s10953-018.

(63) Bouteiller, H.; Pasturel, M.; Lemoine, P. On the Crystal Structures of the Polymorphs of Manganese(II) Chloride Tetrahydrate: α-$MnCl_2{\cdot}4H_2O$ and β-$MnCl_2{\cdot}4H_2O$. *J Chem Crystallogr* **2021**, *51*, 311–316. https://doi.org/10.1007/s10870-020-00856-z.

(64) *Spectral Database for Organic Compounds (SDBS); infrared spectrum; SDBS No.: 12944; RN 1129-30-2; https://sdbs.db.aist.go.jp/sdbs/ (accessed April 23, 2024)*.

(65) Kryatova, M. S.; Makhlynets, O. V.; Nazarenko, A. Y.; Rybak-Akimova, E. V. Nickel(II) Complexes with Tetradentate N_4 Ligands: Synthesis, Structure, Electrochemistry and Thermochromism in Solution. *Inorganica Chim Acta* **2012**, *387*, 74–80. https://doi.org/10.1016/j.ica.2011.12.054.

(66) Ambrosi, A.; Sofer, Z.; Pumera, M. Lithium Intercalation Compound Dramatically Influences the Electrochemical Properties of Exfoliated MoS_2. *Small* **2015**, *11* (5), 605–612. https://doi.org/10.1002/smll.201400401.

(67) Shinagawa, T.; Garcia-Esparza, A. T.; Takanabe, K. Insight on Tafel Slopes from a Microkinetic Analysis of Aqueous Electrocatalysis for Energy Conversion. *Sci Rep* **2015**, *5*. https://doi.org/10.1038/srep13801.

(68) Gong, M.; Zhou, W.; Tsai, M. C.; Zhou, J.; Guan, M.; Lin, M. C.; Zhang, B.; Hu, Y.; Wang, D. Y.; Yang, J.; Pennycook, S. J.; Hwang, B. J.; Dai, H. Nanoscale Nickel Oxide/Nickel Heterostructures for Active Hydrogen Evolution Electrocatalysis. *Nat Commun* **2014**, *5*. https://doi.org/10.1038/ncomms5695.

(69) Noor-Ul-Ain Babar; Khurram Saleem Joya. Spray-Coated Thin-Film Ni-Oxide Nanoflakes as Single Electrocatalysts for Oxygen Evolution and Hydrogen Generation from Water Splitting. *ACS Omega* **2020**, *5*, 10641–10650.

(70) Lovell, E. C.; Lu, X.; Zhang, Q.; Scott, J.; Amal, R. From Passivation to Activation-Tunable Nickel/Nickel Oxide for Hydrogen Evolution Electrocatalysis. *ChemComm* **2020**, *56* (11), 1709–1712. https://doi.org/10.1039/c9cc07486d.

(71) El-Maghrabi, H. H.; Nada, A. A.; Bekheet, M. F.; Roualdes, S.; Riedel, W.; Iatsunskyi, I.; Coy, E.; Gurlo, A.; Bechelany, M. Coaxial Nanofibers of Nickel/Gadolinium Oxide/Nickel Oxide as Highly Effective Electrocatalysts for Hydrogen Evolution Reaction. *J Colloid Interface Sci* **2021**, *587*, 457–466. https://doi.org/10.1016/j.jcis.2020.11.103.

(72) Zeng, M.; Li, Y. Recent Advances in Heterogeneous Electrocatalysts for the Hydrogen Evolution Reaction. *J Mater Chem A Mater* **2015**, *3* (29), 14942–14962. https://doi.org/10.1039/c5ta02974k.

(73) Lee, D. U.; Fu, J.; Park, M. G.; Liu, H.; Ghorbani Kashkooli, A.; Chen, Z. Self-Assembled $NiO/Ni(OH)_2$ Nanoflakes as Active Material for High-Power and High-Energy Hybrid Rechargeable Battery. *Nano Lett* **2016**, *16* (3), 1794–1802. https://doi.org/10.1021/acs.nanolett.5b04788.

(74) Shinagawa, T.; Takanabe, K. Electrocatalytic Hydrogen Evolution under Densely Buffered Neutral PH Conditions. *J Phys Chem C* **2015**, *119* (35), 20453–20458. https://doi.org/10.1021/acs.jpcc.5b05295.

(75) Oeckler, O.; Simon, A. Redetermination of the Crystal Structure of Copper Dibromide, $CuBr_2$. *Z. Kristallogr. NCS* **2000**, *215*.

Appendix

Table 13: List of various H_2 production tests conducted for Chapter 4.

Name of test	Potential (V)	Area H_2	H_2 (µmol)	O_2 Area
Cu3N2O, Graphite WE	-1.3 V	654	24.2	236.7
Cu wire WE (Background)	-1.3 V	32.9	1.2	393.7
Graphite Coat (Ni4N)	-1.3 V	785	29.0	568.7
Graphite Test (Ni4N)	-1.3 V	1434	53.0	386.2
FTO1 Coat	-1.3 V	847	31.3	480.6
FTO1 Test	-1.3 V	2217	82.0	476.7
Blank FTO (Background)	-1.3 V	32.3	1.2	354.1
FTO4 (Sequential Test)	-1.0 V	161.9	5.9	498
FTO4 (Sequential Test)	-1.1 V	430.5	15.9	390.7
FTO4 (Sequential Test)	-1.2 V	337.7	12.5	649.8
rFTO4 recoat	-1.3 V	1212.4	44.8	378.5
rFTO4 test	-1.2 V	783.7	29.0	349.7
r2FTO4 coat	-1.3 V	771.5	28.5	455
FTO7 5 hr test	-1.2 V	3082	114.0	699.1
FTO12 test 1.9 mM	-1.2 V	909	33.6	371.8
$NiCl_2$ coat (Background)	-1.3 V	71.1	2.6	465.3
FTO13 1.0 mM coat	-1.3 V	761	28.1	742.7
FTO15 0.5 mM coat	-1.3 V	888	32.8	582.3
FTO15 0.5 mM test	-1.2 V	950	35.1	315.7
FTO16 0.3 mM coat	-1.3 V	803	29.7	725.7
FTO22 1.0 mM test	-1.2 V	1157.9	42.8	313.6
FTO16 0.3 mM test	-1.2 V	946.5	35.0	148.2
FTO18 0.5 mM test	-1.2 V	1325.6	49.0	183.1
FTO19 1.0 mM test	-1.2 V	959.4	35.5	180.4
FTO20 1.0 mM test	-1.2 V	1153.8	42.7	279.9
FTO13 1.0 mM test	-1.2 V	1003	37.1	423.7
FTO23 0.5 mM test	-1.2 V	1206.1	44.6	156.8
FTO24 0.3 mM test	-1.2 V	1168.5	43.2	102.4
FTO21 0.1 mM test	-1.2 V	686.4	25.4	158.7
FTO26 0.5 mM 5 hr	-1.2 V	3546.9	131.2	479.6
Cu4N FTO28 0.5 mM	-1.2 V	533.05	19.7	149.6
FTO32 0.5 mM	-1.2 V	1271.9	47.0	167.4

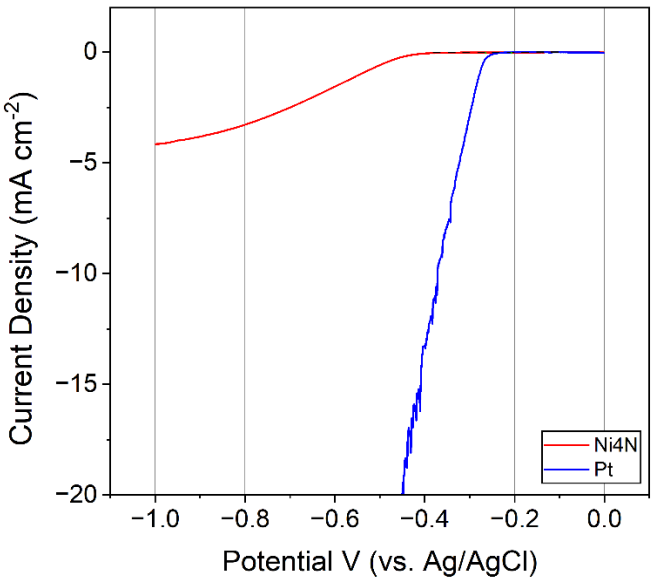

Figure 77: Expanded LSV comparison (*vs.* Ag/AgCl) of Ni4N-coated FTO glass (red) and a bare platinum wire (blue) as the working electrode in 0.5 M H_2SO_4 at a scan rate of 2 mV s^{-1}.